# Elucidating the Mechanical Properties of Crystalline Interfaces from Thermal Fluctuations

A Dissertation

Presented to

the Faculty of the Department of Mechanical Engineering

University of Houston

In Partial Fulfillment

of the Requirements for the Degree

Doctor of Philosophy

in Mechanical Engineering

by

Dengke Chen

December 2015

# Elucidating the Mechanical Properties of Crystalline Interfaces from Thermal Fluctuations

Dengke Chen

Approved:

Chair of the Committee
Yashashree Kulkarni, Associate Professor,
Mechanical Engineering

Committee Members:

Pradeep Sharma, Professor,
Mechanical Engineering

Gemunu Gunaratne, Professor,
Physics

Yichao Chen, Professor,
Mechanical Engineering

Hadi Ghasemi, Assistant Professor,
Mechanical Engineering

Suresh K. Khator, Associate Dean,
Cullen College of Engineering

Pradeep Sharma, Department Chair,
Mechanical Engineering

# Acknowledgements

Until now, I still remember clearly the first day when I stopped by my advisor Dr. Kulkarni's office. It was an awkward situation. I could not speak a complete English sentence, only communicated with the most primitive gestures. It was that day I knew the dislocation, grain boundary and two names "Hull and Bacon" which always tortured me in my whole PhD life.....Then, in a twinkle, five years passed. During this period, I have known more names of the big guys from papers, conferences, seminars and so forth. I appreciate their smartness, humor, erudition. However, to my mind, I respect more the people who lead and support the freshman kindly. Luckily, my advisor is one of them. From the first class to my first paper being published, Dr. Kulkarni has always encouraged me and given me a lot of advice. What she most often says is, "Dengke, I see your potential, trust in yourself and stick to what you like." These simple words have motivated me to overcome obstacles in my research. I appreciate this so much. There has been a few teachers that have trusted me and given me an opportunity like this since I graduated from high school.

Since I came to UH, I have also met other nice and helpful professors. Our department chair, Dr. Sharma, is the professor I see the most everyday. He always got me back on track when I got trapped in a helpless situation. I am especially grateful to him for analyzing the gains and loses for my Postdoc offer, which helped me decide to go to Atlanta for postdoc. Professor Wheeler, I got three A's from his courses, also helped me a lot in my first year. Even though he has retired, every time he came to department he would ask my advisor my situation. I was greatly touched that he came forward to shake my hands and congratulated me after he knew I got an offer. Dr. Agrawal, the professor I asked for recommendation letters almost every time when I tried to apply scholarship or

other positions. I appreciate that he could take time out from his busy schedule to write these boring letters. In addition, I sincerely thank the other members on my PhD committee, Dr. Gemunu Gunaratne, Dr. Yichao Chen, Dr. Hadi Ghasemi, for giving their precious and kind suggestions on my dissertation.

I would also like to thank all my labmates for making my PhD life full of enthusiasm and fun. Yuranan, the previous postdoc in our lab, now is the assistant professor in Thailand, taught me a lot of things whether in research or in personal life. Especially that long talk in Berkeley enlightened me. Qian, who will be associate professor in China, is not only the senior that can lead me in research but also the funny player who goes to gym with me for many years. Thanks to him for urging me to make it a rule to go to gym every week. I give special thanks to Nikhil, Fatemeh, for their invaluable help in research. Every time I faced the problem, I would disturb them. I feel truly thankful to have met Fan, Shuyin, Shengjie, Xiaobao, Xin, who have given me the priceless friendship. Also thank the other labmates, Nebiyu, Tanushree, Farah, Vikash, Sana, Himani, Mehdi, Ehsan, Matthew, Zeinab, Tarek, Dajla who have constituted this friendly lab.

Finally, I want to thank my parents for their endless love which has given me the courage and strength to pursue my PhD. Though they are getting older and older, they still do not give me any pressure on earning money, marriage... I am very guilty of not having too much time to take care of them during the whole Phd period. I also thank my little brother for accompanying our parents instead of me these years. Family is the greatest motivation. I love them all!

# Elucidating the Mechanical Properties of Crystalline Interfaces from Thermal Fluctuations

An Abstract

of a

Dissertation

Presented to

the Faculty of the Department of Mechanical Engineering

University of Houston

In Partial Fulfillment

of the Requirements for the Degree

Doctor of Philosophy

in Mechanical Engineering

by

Dengke Chen

December 2015

# Abstract

Nanostructured materials have gained prominence owing to the exciting array of physical properties that are primarily governed by the high density of interfaces and interfacial phenomena. This dissertation presents the statistical mechanics modeling and atomistic simulations of two types of crystalline interfaces, namely twin boundaries and grain boundaries, to understand their thermodynamic and kinetic properties based on thermal fluctuations.

To this end, we first study the thermal fluctuations of twin boundaries in face-centered-cubic metals to elucidate the deformation mechanism governing their kinetic properties. Our simulations show that the normal motion of twin boundaries is strongly coupled to shear deformation up to near the melting temperature. Since twin boundaries commonly occur as parallel interfaces, we further investigate the entropic interaction between fluctuating twin boundaries using atomistic simulations and statistical mechanics based analysis. The simulations reveal that fluctuations of twin boundaries are enhanced in the presence of adjoining twin boundaries as their spacing $d$ decreases. In addition, the theoretical analysis shows that fluctuating twin boundaries indeed exhibit an attractive entropic interaction which enhances their thermal fluctuations and that this force decreases as $1/d^2$. This attractive interaction between twin boundaries is attributed to their shear coupled normal motion and is fundamentally distinct from the well-known repulsive entropic interaction followed by fluid membranes and many crystalline membranes and interfaces.

In addition to the entropic force, we present a study of the thermal expansion of twin boundaries at finite temperature by way of atomistic simulations. The simulations reveal that for all twin boundary spacing $d$, the thermal expansion induced stress varies as $1/d$. This long-range effect is attributed to the inho-

mogeneity in the thermal expansion coefficient due to the interfacial regions.

Finally, we study the effect of defects, specifically second phase particles, in grain boundaries by extending the interface random walk model, and deriving the general analytical expression relating the grain boundary mobility to key parameters governing the interaction between the particles and the grain boundary. We verify our theoretical model through atomistic simulations for symmetrical tilt boundaries with multiple fixed inclusions and propose a method to extract the mobility from grain boundary fluctuations.

# Table of Contents

# List of Figures

# List of Tables

# Chapter 1 Introduction

## 1.1 Motivation

Nanostructured materials have gained prominence owing to the exciting array of physical properties that are primarily governed by the high density of interfaces and interfacial phenomena. In the context of this work, interfaces imply crystalline planar defects, such as grain boundaries and twin boundaries, that are known to be key players in governing the behavior of crystalline materials. Indeed, the energetics, atomistic structure, and distribution of these grain boundaries (GBs) or twin boundaries (TBs), have been implicated in a wide range of material characteristics including mechanical properties [1, 2, 3, 4, 5], thermal transport [6, 7, 8, 9, 10, 11, 12, 13, 14, 15], and electronic properties [16, 17, 18, 19, 20, 21, 22]. The study of GBs and their key role in mechanical properties such as strength [1, 2, 3, 4, 23, 24, 25, 26, 27], ductility [28, 29, 30, 31, 32], fracture toughness [33, 34, 35, 36, 37, 38] and creep [39, 40, 41, 42, 43], has spanned decades, with several seminal contributions shaping our understanding of these interfaces over the years. However, with the advent of nanotechnology, the need for quantitative atomistic insights into the response of GBs and how the knowledge can be used to design novel nanomaterials has become vital. This provides the motivation for our work which aims to elucidate the thermodynamic and kinetic properties of crystalline interfaces, specifically, GBs and TBs, by way of statistical mechanics modeling and atomistic simulations.

### 1.1.1 GB and TB Structure

A grain boundary is the interface between two adjacent grains with different crystallographic orientations in a polycrystalline material, as shown in Figure 1.1.

General grain boundaries are rather complicated defects and need at least five

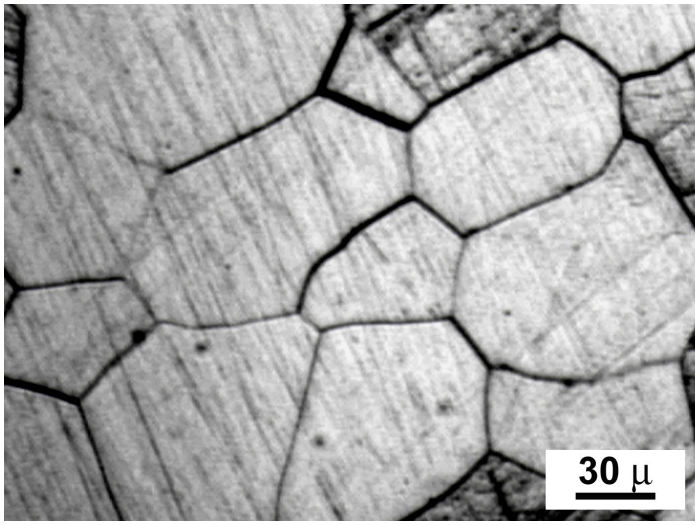


Figure 1.1: Micrograph of grain boundaries in polycrystal [44].

macroscopic parameters for geometric description, in which three are associated with another grain orientation and the other two specify the direction normal to the boundary [45]. In practice, researchers use the coincident site lattice (CSL) [46] model to denominate and distinguish different grain boundaries. In CSL theory, the degree of fit $\Sigma$ is the reciprocal density of coincidence sites between the structures of the two grains. To put it simply, small $\Sigma$ corresponds to more atoms coincident with each other between two adjacent grains. In the extreme case, $\Sigma 1$ represents perfect crystallinity without grain boundaries. Thus lower $\Sigma$ grain boundaries typically have lower grain boundary energies. Other than $\Sigma$, grain boundaries are also classified based on their angle of mismatch into two groups – low angle grain boundaries with a mismatch angle less than 15 degrees and high angle grain boundaries with a mismatch angle greater than 15 degrees. Low angle grain boundaries have a well-defined structure and are amenable to theoretical analysis. High angle grain boundaries have an increasingly more amorphous interfacial region with increasing mismatch angle and are prone to processes such as GB sliding, and migration. A typical polycrystal with randomly oriented grains

naturally contains all kinds of low-angle, high-angle and random GBs.

A special type of crystalline interface is known as the twin boundary denoted by Σ3. Although, the TB is a high angle grain boundary, but it is highly symmetric and hence has one of the lowest GB energy of about 22 eV. Figure 1.2 shows a TB in a face-centered-cubic crystal formed by the mirror reflection of the atomic layers about a (111) plane. Since the stacking sequence along the (111) direction is ABCABC..., the reflection leads to the formation of an interface between the matrix and the twin.

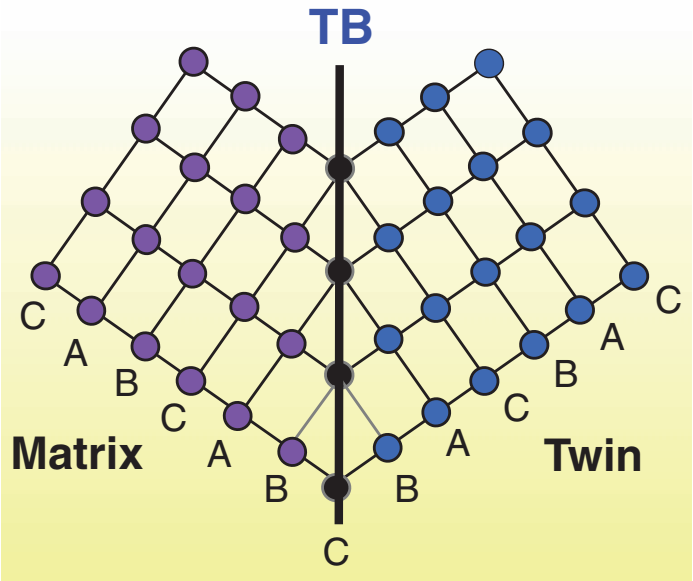


Figure 1.2: Schematic illustration of a Σ3 CTB structure in a FCC metal [32].

### 1.1.2 Effect of GBs on Mechanical Properties

As the grain size is decreased, especially to the nanoscale, more fraction of atoms are located in the core region of grain boundaries, as shown in Figure 1.3. Thus, the whole polycrystal is divided into perfect regions and disordered grain boundaries regions. Assuming the grains to be shaped as spheres or cubes, the volume fraction of disordered grain boundaries can be as much as 50% for average 5 nm grain size [5]! This large fraction of grain boundaries density is des-

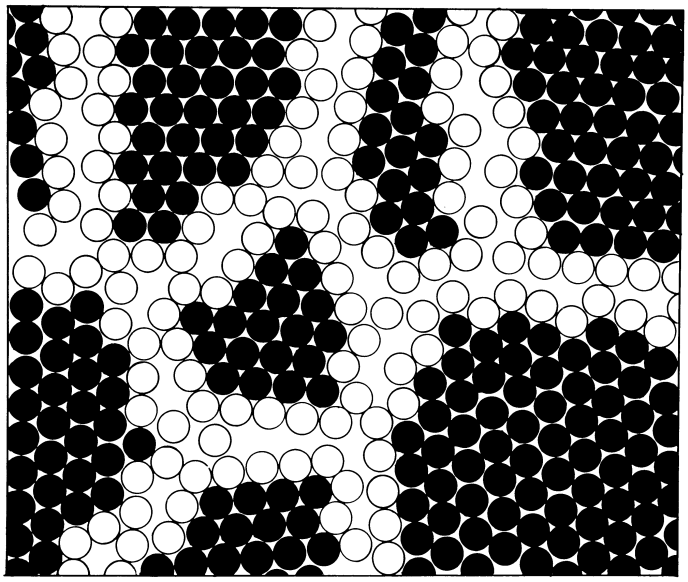

Figure 1.3: Atomic structure of a two-dimensional nanocrystalline material [1].

tined to significantly alter the multiple properties of crystalline materials. Given our background and interests, we present a brief review of the effect of GBs on mechanical properties in the following sections.

**Material Strength**

It is well established that the refinement of grains impedes dislocation movement and hence the onset of plasticity thereby increasing the materials strength. The dependence of yield stress on the grain size can be explained by the Hall-Petch relation

$$\sigma_y = \sigma_0 + kd^{-\alpha}, \tag{1.1}$$

where $\sigma_y$ is the yield stress, $d$ is the average grain size, $k$ and $\alpha$ are d-independent positive constants. Due to this attractive property, nanocrystalline (NC) face-centered-cubic (FCC) metals, with an average grain size less than 100 nm, witnessed an intensity of research in the nineties owing to their ultrahigh strength compared with their ultrafine grain (UFG) crystalline and conventional coarse-grain (CG) polycrystalline counterparts, with grain size in the range 100 nm - 1

$\mu$m and greater than 1 $\mu$m respectively [24, 30].

The increase in strength is primarily associated with the fact that grain boundaries act has effective barriers to dislocation motion, thereby inhibiting the onset of plasticity. However, After the grain size is reduced below a critical point, usually at 10 nm, the materials get softer surprisingly. This phenomenon is referred to as the inverse Hall-Petch relation and is attributed to a radical transition in mechanism as GB-mediated processes such as sliding and migration become dominant [24, 27]. Figure 1.4 shows the panorama of yield stress variation in the whole grain size range.

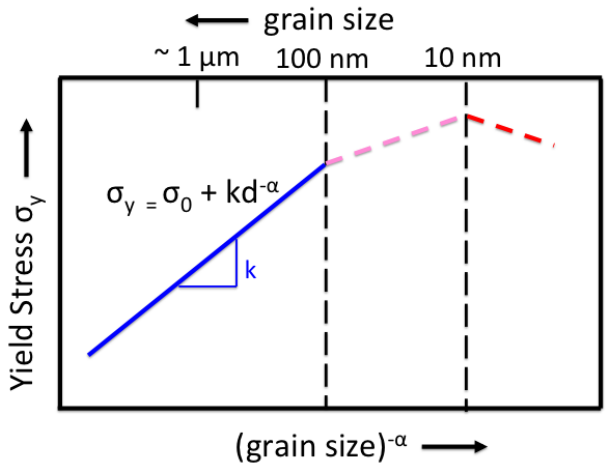


Figure 1.4: Schematic representation of the variation of yield stress as a function of grain size in coarse-grain (CG) polycrystalline, ultrafine grain (UFG) crystalline and nanocrystalline (NC) metals and alloys[24].

**Ductility**

Although a high density of grain boundaries leads to very high strengths, they have a detrimental effect on the material ductility. Most NC metals with grain sizes less than 25 nm typically show less than 2% elongation to failure in contrast to 40% - 60% for their conventional polycrystalline counterparts [23, 26]. Figure 1.5 shows that most nanostructured metals fall into the "high strength—

low ductility" shaped blue region. In the context of nanocrystalline materials, it is observed that the grain boundaries can eventually serve as stress concentrators leading to a loss of ductility. Simultaneously, elevated temperature tends to weaken the nanocrytalline stability due to the grain growth [2].

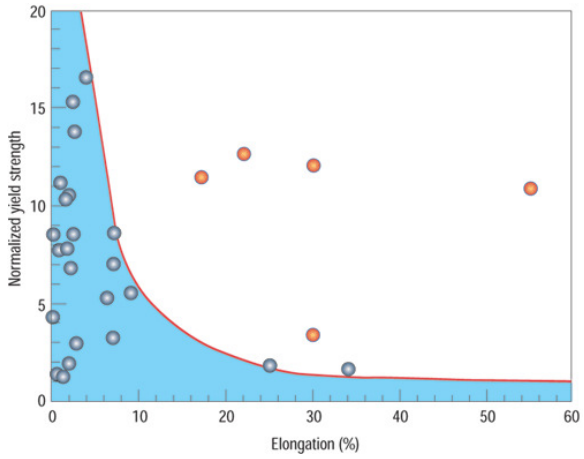


Figure 1.5: Normalized yield strength versus percentage elongation (ductility) for nanostructured metals[26].

Nanotwinned (NT) FCC metals, as show in Figure 1.6, are designed by the introduction of coherent TBs (CTBs) within ultra-fine crystalline metals having a grain size of a few hundred nanometers and exhibit attractive properties of retaining ductility along with ultra-high strength [28, 29, 31]. Indeed, Lu et al.

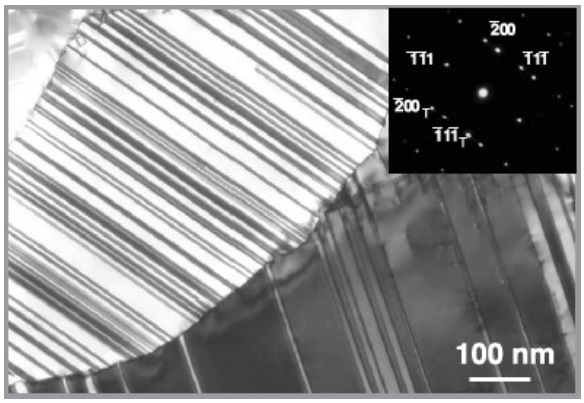


Figure 1.6: TEM observations of the microstructure in NT Cu sample [28].

[28] showed that nanotwinned (NT) Cu containing twin lamella of about 35 nm

thickness exhibits a yield strength over 1 GPa with elongation to failure as high as 14%, which is in sharp contrast to NC-Cu having a yield strength of about 400 MPa and elongation to failure of about 2-3% for comparable grain sizes, as show in Figure 1.7. Owing to these superior properties, nanotwinned metals have been

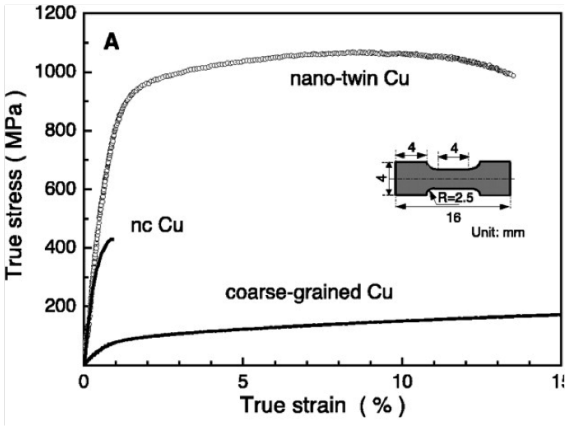


Figure 1.7: A typical tensile stress-strain curve for the NT Cu in comparision with that for a CG-Cu sample and a NC-Cu sample [28].

the subject of active research in recent years [47, 32, 48, 49, 50, 51, 52, 53, 54, 55, 56, 57].

**Fracture Toughness**

Decreasing the grain size increases the fracture toughness which is similar to increasing the yield strength with grain refinement. The reasonable explanation is that GBs arrest a crack initiated in the neighboring grain and thus delay the propagation of fracture [33, 34]. As the grain size decreases, more grains impede the propagation effectively, as show in Figure 1.8. As we know that the Hall-Petch relationship fails when the grain size is reduced below a critical point. The dependence of fracture toughness on the grain size follows the same rule. At these grain sizes, intergranular fracture is expected to happen [34]. The crack tip inside the grain initially induces a limited emission of dislocation and soon creates several nano-voids in the surrounding boundaries, finally propagating along the grain

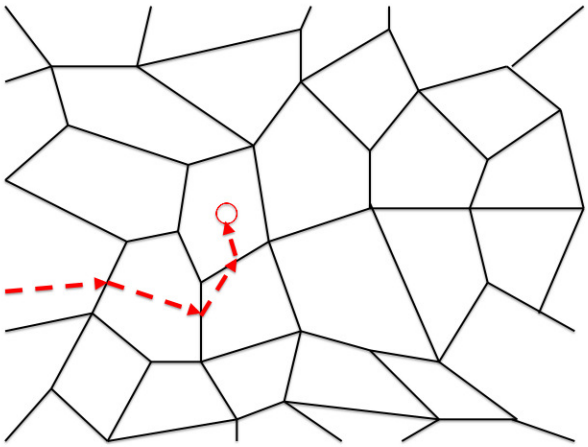

Figure 1.8: Crack propagation in a nanocrystal. Red line represents the propagation path.

boundaries, as shown in Figure 1.9. When a crack tip is artificially made inside a

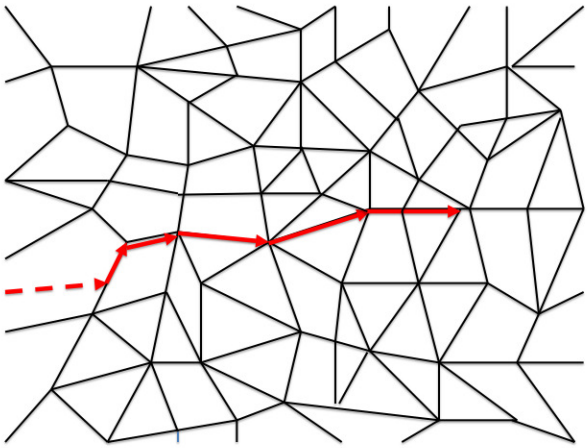

Figure 1.9: Intergranular fracture propagation. Red line represents the propagation path.

grain, the crack initially blunts by a limited emission of partial dislocations, but soon this behavior is taken over by the creation of nanovoids in the surrounding grain boundaries, initiating an intergranular fracture mechanism, the nanovoids joining the main crack.

**Radiation Tolerance**

In addition to sustaining high stresses, many materials are subject to extreme environments, such as nuclear radiation. The radiation creates numerous point defects, such as interstitials and vacancies, which can in turn affect the strength, ductility, fracture toughness and other mechanical properties of materials. Thus it is necessary to design structural materials for nuclear power systems with high radiation tolerance.

Compared to conventional polycrystalline materials, NC materials containing a large fraction of GBs have been shown to improve radiation resistance [58, 59, 60, 61]. GBs can serve as sinks that attract, absorb point and line defects and thus enhance the tolerance by leaving the bulk region around the GBs relatively defect-free, as shown in Figure 1.10. In fact, although GBs improve radiation tolerance, the defects absorbed by the GBs can also affect their properties, such as migration and mobility, and finally affect the microstructural evolution of materials. In Chapter 5, we will provide insights into the interaction between defects and GBs.

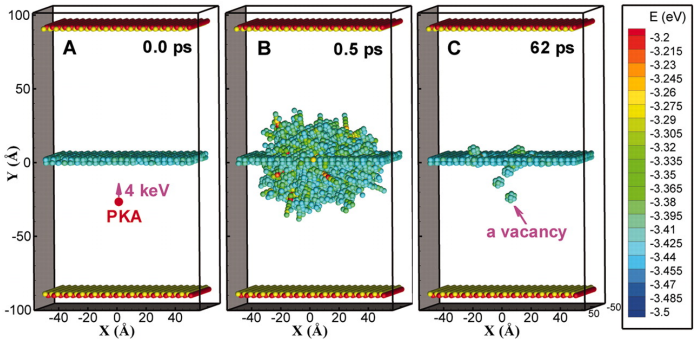


Figure 1.10: Representative snapshots of a MD simulation of a collision cascade near a Σ11 symmetric tilt GB at 300 K at three different time intervals. The atoms are colored by their potential energy [59].

## 1.2 Equilibrium Thermal Fluctuation of Interfaces

While these superior properties certainly open up exciting avenues for the applications of nanostructured materials, they also call for a critical examination of the stability of these structural motifs especially at high temperatures. By structural instability, we imply processes such as grain growth, which are intimately connected to properties like interfacial stiffness, mobility, as well as the interaction of the constituting interfaces, such as GBs and TBs. An analysis of the thermal fluctuations based on statistical mechanics provides a convenient and powerful approach to gain insight into these interfacial properties.

There exists a number of numerical methods in the literature for the calculation of interfacial properties, such as interfacial free energy $\gamma_s$, stiffness $\Gamma$ and mobility $M$. In general, these methods can be broadly classified as "driving force" or "finite strain" method and "thermal fluctuations" method. The former [62, 63, 64, 65, 66, 67] is straightforward in which the driving force or finite strain is applied to induce the interfacial deformation or movement and the properties can be obtained from the general constitutive relation. The latter approach [68, 69, 70, 71, 72, 73, 74, 75, 76] utilizes the fluctuations of thermodynamic parameters such as strain and displacement to extract the desired properties. Since the dimensions of the nanostructure are limited and noise is unavoidable during the atomistic simulations, thermal fluctuations approach has gained prominence and is widely used to provide insights into the thermodynamic and kinetic properties of these interfaces.

In their pioneering work [77], Parrinello and Rahman proposed a method to extract the elastic constants from the thermal strain fluctuations of bulk crystal. To be specific, they showed that

$$C_{ijkl} = \frac{k_B T}{< V >} (\epsilon_{ij} \epsilon_{kl})^{-1}, \tag{1.2}$$

where $C_{ijkl}$ is the forth-order stiffness tensor, $\epsilon_{ij}$ is the strain tensor, $< V >$ is the ensemble average volume of the system, $k_B$ is the Boltzmann constant, $T$ is the temperature. Ever since then, plenty of works have sprung up like mushrooms after rain [78, 79, 80, 81, 82, 83, 84]. It is worth noting that in Equation 1.2, the strain tensor $\epsilon_{ij}$ is not straightforward to calculate. Meyers [83] proposed a method to involve the atomic displacement instead of strain, given by

$$< \tilde{u}_i(\mathbf{k})\tilde{u}_k(\mathbf{k}) > \frac{k_b T}{V}(C_{ijkl}k_j k_l)^{-1}, \tag{1.3}$$

where $\tilde{u}_i(\mathbf{k})$ and $\tilde{u}_k(\mathbf{k})$ are the displacement components in Fourier space for wave vector $\mathbf{k}$. We refer the reader to Landau and Lifshitz [85] for details of the derivation.

After a simple modification, Equation 1.3 can be easily applied into two dimensional membranes [86, 87]. For a fluctuating fluid membrane, as shown in Figure 1.11, the energetic cost for the out-of-plane fluctuations arises from the bending stiffness of the membrane. Then the Hamiltonian of the membrane can

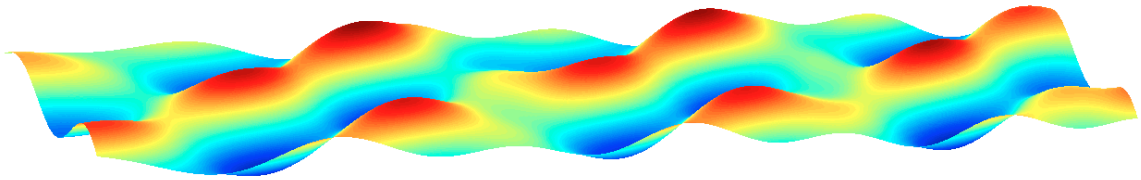

Figure 1.11: Schematic diagram of a freely fluctuating membrane. Different colors indicate different out of plane displacements [88].

be written as

$$H = \frac{1}{2}\kappa \int (\Delta h)^2 d\mathbf{r}, \tag{1.4}$$

where $\kappa$ is the bending stiffness of the membrane, $h$ is the out-of-plane displacement. Expanding $h$ in Fourier space, we have

$$h = \sum A(\mathbf{k})e^{i\mathbf{kr}}, \tag{1.5}$$

where A(k) is the fluctuation spectrum. Then, the Hamiltonian can be expressed in the form

$$H = \frac{1}{2} S\kappa \sum k^4 S^2(\mathbf{k}), \tag{1.6}$$

where $S$ is the area of the membrane. We note that the energy is quadratic in $A(\mathbf{k})$. Using the equipartition of energy, the relation between the mean square fluctuation spectrum and the bending stiffness can be obtained,

$$< A^2(\mathbf{k}) >= \frac{k_b T}{S\kappa k^4}. \tag{1.7}$$

Although initially developed for fluid membranes, the membrane theory has also been effectively applied to study crystalline membranes such as graphene and other two-dimensional materials [89, 90], as well as crystalline interfaces, such as GBs, and solid-liquid interfaces based on thermal fluctuations. For instance, several high angle GBs in FCC metals exhibit capillarity induced fluctuations. Here, the energetic cost of the GB fluctuations stems from the increase in the GB area to accommodate the out-of-plane deformation. Thus, the Hamiltonian becomes

$$H = \frac{1}{2}(\gamma_s + \gamma_s'') \int \nabla^2 h d\mathbf{r}, \tag{1.8}$$

where $\gamma_s + \gamma_s''$ is defined as the GB stiffness $\Gamma$, which it can be determined from the mean square fluctuation spectrum as before

$$< A^2(\mathbf{k}) >= \frac{k_b T}{S\Gamma k^2}. \tag{1.9}$$

In the case of solid interfaces, the central idea is that the energetic cost for the out-of-plane fluctuation of the interface, which naturally involves deformation of the adjoining bulk regions, is used to construct an energy associated only with the interface. Then the surrounding bulk can be neglected and the interface is regarded as a membrane with an appropriate elastic energy. This means that they can be modeled as membranes whose out-of-plane fluctuations are governed by

interfacial stiffness. Motivated by the striking resemblance between membranes and crystalline interfaces, many mature methods on statistical thermodynamics of membranes can be borrowed and developed for gaining insight into the properties of these solid interfaces and their important role in the mechanical response of nanostructured materials.

## 1.3 Computational Approach

Theoretical analysis, numerical calculation and experimental measurement are considered as the three main approaches in modern science. Among them, computational modeling has been widely used in a variety of science and engineering fields due to its ability to serve as a virtual experimental tool as well as predict unknown phenomena. Especially the latter property has gained more and more attention in recent decades. From macroscopic to microscopic scale, there are plenty of simulation methods, such as finite element method (FEM), Monte Carlo method (MC), molecular dynamics method (MD), density functional theory (DFT) and so forth. Generally, increase in accuracy and resolution comes with limitation in simulation size and invariably longer simulation time. MD method stands out of the competition and has become one of the most popular computational simulation techniques for studying the behaviors of materials due to its balance in accuracy and efficiency.

MD is a computational simulation of the time evolution of a system with N particles based on the classical Newtonian mechanics [91]. All the particles, usually atoms or molecules are considered as rigid bodies interacting with each other. Their interactions are described by the means of empirical interaction potential. By numerically integrating Newton's equations of motion with proper initial conditions, the trajectory including the positions and velocities of each par-

ticles is obtained and the configuration of the whole systems is determined. To be specific, there are several key components:

**(1) Interaction Potential**

Fundamentally, materials derive their properties from the interaction between their constituent atoms [92]. The most intuitive thought is that two atoms do not like to get close to each other but attract when they are located at a longer distance. This can be described as the classic "Lennard-Jones" (LJ) pair potential [93],

$$\phi(r) = 4\epsilon_0[(\frac{r}{\sigma_0})^{-12} - (\frac{r}{\sigma_0})^{-6}]. \tag{1.10}$$

Here, $r$ is the distance between the two atoms, $\epsilon_0$ is the depth of the energy well and $2^{1/6}\sigma_0$ is the distance in which the potential reaches its minimum value. Given the simple nature of the LJ potential, several richer interatomic potentials have been developed that go beyond the pair potential. Among them, the embedded atom method (EAM) [94] potential is simple and efficient and hence has been widely used for metals. For the EAM potential, the potential energy of the system with $N$ particles is given by

$$V(\{\mathbf{r}_i\}) \equiv V(\mathbf{r}_1, \mathbf{r}_2, ..., \mathbf{r}_N) = \sum_{i<j} \phi(r_{ij}) + \sum_i F(\sum_{j\neq i} \rho(r_{ij})), \tag{1.11}$$

where $r_{ij}$ is the distance between atoms $i$ and $j$, $\phi$ is a pair-wise potential function, $\rho$ is the contribution to the electron charge density from atom $j$ at the location of atom $i$, and $F$ is an embedding function that represents the energy required to place atom $i$ in the electron cloud. Then the force acting on the atom $i$ is the negative derivative of the potential function, i.e.,

$$\mathbf{f}_j = -\frac{V(\{\mathbf{r}_i\})}{\partial \mathbf{r}_j}. \tag{1.12}$$

The EAM potential is a multi-body potential and gives very good estimates for defect energies in metals such as vacancy formation energy, GB energy, and stacking

fault energy. Hence, EAM potentials are suitable and very efficient for studying the mechanical properties of metals.

**(2) The Verlet Algorithm**

According to the Newton's second law, the equation of motion can be given by

$$m\frac{d^2\mathbf{r}_i}{dt^2} = -\frac{V(\{\mathbf{r}_i\})}{\partial \mathbf{r}_j}. \tag{1.13}$$

Once the initial position and velocity are determined, the new positions and velocities are obtained from numerical integration. The Verlet algorithm [95] is one of the simplest and most stable in MD simulation. To be specific, the updated positions and velocities are calculated as

$$\mathbf{r}_i(t+\Delta t) = \mathbf{r}_i(t) + \mathbf{v}_i\Delta t + \mathbf{a}_i(t)\frac{\Delta t^2}{2}, \tag{1.14a}$$

$$\mathbf{a}_i(t+\Delta t) = -\frac{1}{m}\frac{\partial V(\{\mathbf{r}_i(t+\Delta t)\})}{\partial \mathbf{r}_i(t+\Delta t)}, \textit{ and} \tag{1.14b}$$

$$\mathbf{v}_i(t+\Delta t) = \mathbf{v}_i(t) + [\mathbf{a}_i(t) + \mathbf{a}_i(t+\Delta t)]\frac{\Delta t}{2}. \tag{1.14c}$$

**(3) Energy Minimization**

Energy minimization is utilized to obtain a stable equilibrium configuration with the minimum possible potential energy. Many algorithms have been developed to accelerate the minimization process. Among them, conjugate gradient method is most commonly implemented in atomistic simulations due to its efficiency and simplicity [96].

## 1.4 Dissertation Outline

In this dissertation, we present the statistical mechanics modeling and atomistic simulations crystalline interfaces based on thermal fluctuations. Specifically,

our aim is to understand the fluctuations of and entropic interaction between twin boundaries as well as the effect of defects, such as second phase particles, on the kinetics of grain boundaries. The rest of the dissertation is organized as follows.

In Chapter 2, we investigate the thermal fluctuations of twin boundaries in FCC metals to elucidate the deformation mechanism governing their kinetic properties by way of molecular dynamics simulations. In Chapter 3, we present the entropic interaction between fluctuating twin boundaries constituting a NT structure at finite temperature by means of atomistic simulations and statistical mechanics modeling. In Chapter 4, we report the long-range thermal force inside these NT metals induced by the inhomogeneity in the thermal expansion coefficient due to the interfacial regions. In Chapter 5, we extend the interface random walk model to account for the drag effect of second phase particles. We re-derive the GB diffusion equation in time domain and frequency domain, and propose a simple and efficient calculation approach to obtain the modified GB mobility.

# Chapter 2 Kinetics of Twin Boundaries from Thermal Fluctuations

## 2.1 Introduction

Nanotwinned (NT) metals are known to demonstrate a remarkable combination of mechanical properties, namely, ultra-high strength, enhanced ductility, and high strain rate sensitivity [28, 31, 32, 53, 97, 98, 99, 100]. This is in contrast to nanocrystalline (NC) materials which exhibit a loss of ductility, and grain stability with decreasing grain size, thereby offsetting the initial excitement generated by their very high yield strength (see [30] for review). It is well documented, through many experimental and theoretical studies, that this loss of stability of nanograined metals, which has severely limited their practical application, is associated with thermally-activated or stress-assisted grain growth caused by grain boundary mediated processes such as migration and sliding [101, 102, 103, 104, 105, 106]. It is natural then, that the grain growth and twin lamella stability in NT metals would also be intimately connected to the thermodynamic and kinetic properties of twin boundaries (TB) and grain boundaries (GB). Although the prospect of the stability of NT structures is of vital concern, one which defines their ultimate utility and raises fundamental questions regarding the underlying physics, the issue has remained relatively unaddressed until recently [107, 108, 109].

In this Chapter, we report our investigation of the motion of twin boundaries by way of computational modeling of their thermal fluctuations over a range of temperatures. In the theory of statistical mechanics of interfaces, thermal fluctuations have been effectively used to elucidate the thermodynamic and kinetic

properties of fluid and solid membranes and interfaces [86]. In the case of high-angle grain boundaries, the capillary wave theory has been successfully used to capture their long wavelength thermal fluctuations to derive important quantities such as the grain boundary stiffness and mobility [72]. The energetic cost for these out-of-plane fluctuations comes from the surface tension, or in other words, the increase in the area of the interface to accommodate the bending due to fluctuations. The Fourier spectrum of these capillarity-induced fluctuations is given by

$$< A^2(k) >= \frac{k_B T}{S\Gamma k^2}, \tag{2.1}$$

where $k$ is the wave vector, $A(k)$ is the amplitude of the mode $k$ fluctuation, S is the area of the interface or gain boundary, and $\Gamma$ is the interfacial stiffness. The initial aim of our work was to furnish a constitutive description for the motion of twin boundaries based on this relation. However, as described in what follows, our molecular dynamics simulations revealed that a fluctuating twin boundary, unlike other high angle grain boundaries, does not exhibit capillary fluctuations.

## 2.2 Simulation Method

In our simulations, the TB fluctuations were modeled by way of molecular dynamics simulations using LAMMPS (Large-scale Atomic/Molecular Massively Parallel Simulator) [110]. All simulations were performed on Cu using the embedded-atom method developed by Mishin et al. [111]. At each temperature, the simulation cell was first equilibrated for 100 ps at zero pressure using the NPT ensemble. The molecular dynamics run was then carried out for 1 ns under the NVT ensemble using the Nose-Hoover thermostat. The system configuration was observed every 1000 time steps. To investigate the effect of temperature on the fluctuations, the simulations were carried out over temperatures ranging from

100 K to 1800K. The simulation box dimensions were $L_x \approx 300\mathring{A}$, $L_y \approx 100\mathring{A}$, and $L_z \approx 20\mathring{A}$ with periodic boundary conditions in the $x$ and $z$ (lateral) directions as shown in Figure 2.1. The specimen was oriented along the $[\bar{1}12]$, $[\bar{1}1\bar{1}]$ , and $[\bar{1}\bar{1}0]$ crystallographic directions. Since the cell dimension was much smaller in the $z$ direction, the fluctuations along this direction were neglected. The $y$ direction was aligned normal to the TB, and the fluctuations were observed along the $x$ direction. To assess the effect of cell size on the fluctuation measurements, we also performed the simulation at 1000K on a larger specimen with dimensions $600\mathring{A} \times 200\mathring{A} \times 40\mathring{A}$. The results changed only negligibly confirming that our initial choice of dimensions was appropriate for extracting the thermal fluctuations of a single interface.

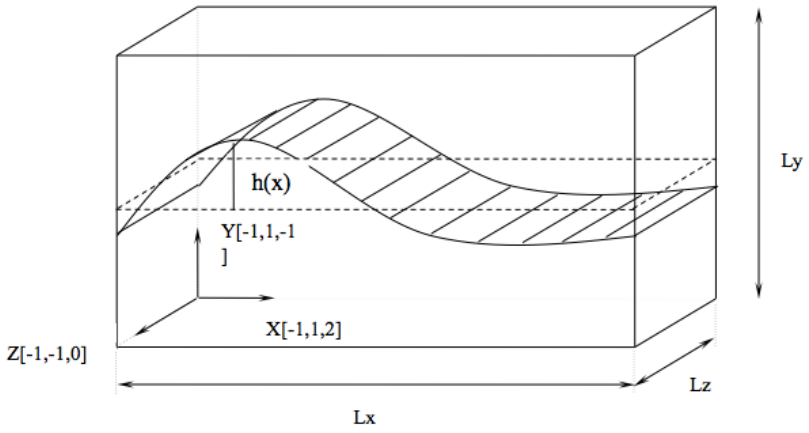


Figure 2.1: Schematic of the bicrystal specimen showing the flat twin boundary at 0K (dotted lines) and the fluctuating twin boundary at finite temperature (solid lines) [112].

At 0K, the TB is a flat interface located at the center of the simulation box as shown by the dotted lines in Figure 2.1. At finite temperature, the interface fluctuates and we denote the instantaneous out-of-plane displacement by $h(x)$. Many approaches have been proposed to locate the instantaneous position of a fluctuating interface in molecular dynamics simulations [69, 113, 68, 74]. In

this work, we use the centrosymmetry parameter to distinguish between atoms belonging to the interface and the bulk and thus, identify the instantaneous TB position. The centrosymmetry parameter of an atom is given by

$$CS = \sum_{i=1}^{N/2} |\mathbf{R}_i + \mathbf{R}_{i+N/2}|^2, \tag{2.2}$$

where $N$ is the number of nearest neighbors and equals 12 for FCC crystals. $\mathbf{R}_i$ and $\mathbf{R}_{i+N/2}$ are vectors from the central atom to a particular pair of nearest neighbors. For a perfect crystal region, $CS$ is zero; for defects such as a dislocation, grain boundary, or surface, it is a finite real number. Since the fluctuation could be ignored in the $z$ direction, $CS$ did not change significantly in this direction and hence, was summed along this direction. Thus, to obtain a smooth curve for the variation of $CS$ along the $y$ direction to identify the interface position, the simulation cell was divided into many slices along the $x$ direction as shown in Figure 2.2. Within each slice, this local parameter $CS$ was extracted as the average

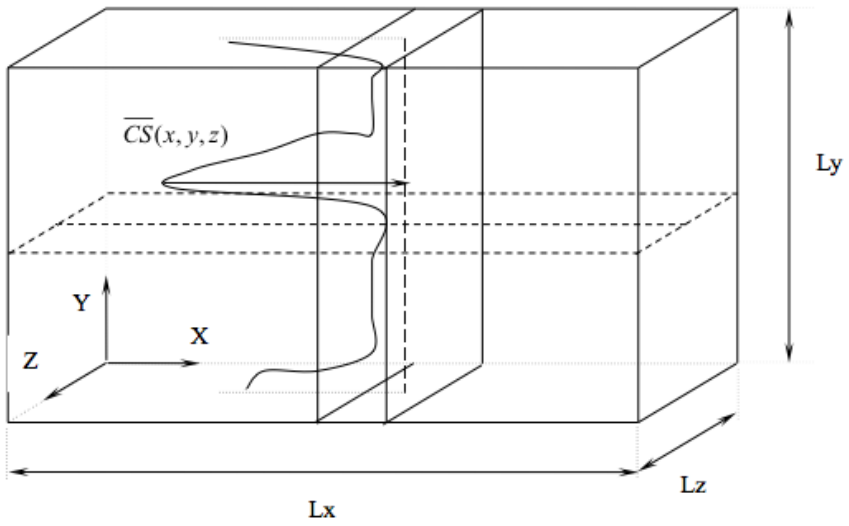


Figure 2.2: Schematic of the bicrystal showing the variation of the average centrosymmetry parameter, $\overline{CS}$ in a slice along the x-axis. This is used to identify the instantaneous position of the twin boundary [112].

$$\overline{CS}(x,y) = \sum_i \frac{CS_i}{(y_i - y)^2 + 1}. \tag{2.3}$$

Based on the method proposed by Trautt et al.[74]. $CS_i$ denotes the centrosymmetry parameter of atom $i$ and $y_i$ is the $y$-coordinate of atom $i$. Then, the average centrosymmetry function, $\overline{CS}$, for each slice, depends on $y$, and can be plotted for any particular slice along the x-direction. The peak corresponds to the instantaneous location of the TB in this slice. Following a similar procedure for each slice, the profile of the function $h(x)$ can be obtained. The Fourier transform of $h(x)$ is given by

$$h(x) = \sum_k A(k)\, e^{ikx}. \tag{2.4}$$

Assuming the simulation cell to be divided into N slices labeled as $x_i, i = 0, 1, 2, \ldots, N-1$, the fluctuation spectrum $A(k)$ is obtained as the Discrete Fourier Transform

$$A(k) = \frac{1}{N} \sum_{i=0}^{N-1} h(x_i) \exp(-2\pi k \frac{i}{N}). \tag{2.5}$$

Once the fluctuation amplitude $A(k)$ is computed for a given snapshot of the interface, the fluctuation average, $< A^2(k) >$ can be determined by computing the average over the snapshots taken at every 1000 time steps during the simulation.

## 2.3 Results and Discussion

Figure 2.3 shows the results for the variation of the power spectrum, $< A^2(k) >$, with $k$ for different temperatures on a log-log plot. The blue, green and red solid lines with slope -1 indicate trend lines obtained for each curve by least squares method for temperature 300K, 800K and 1300K respectively. The black solid line with slope -2 represents the thermal fluctuation curve for high angle grain boundaries. We observe that $< A^2(k) >$ has a linear dependence on $1/k$ all the way up to 0.9 homologous temperature. Within the context of existing

literature on thermal fluctuations of low angle GBs and high angle GBs, this is a rather unexpected behavior of coherent TBs.

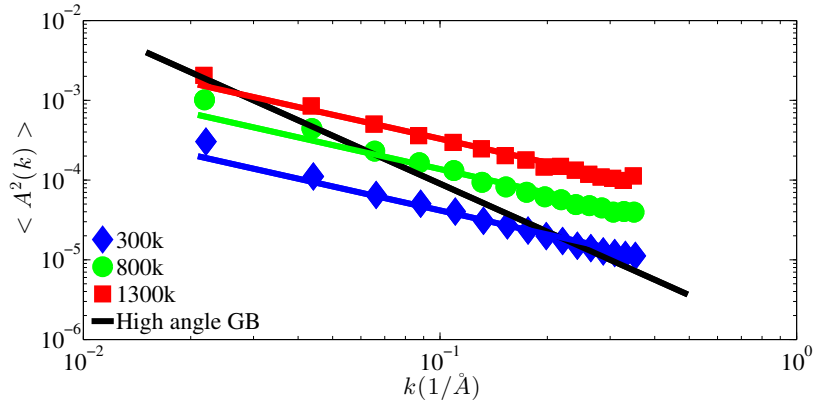


Figure 2.3: Power spectrum of TB fluctuations as a function of k for different temperatures obtained by molecular dynamics simulations [112].

As mentioned earlier, several molecular dynamics studies have revealed that many high angle GBs follow the relation described by Equation 2.1, exhibiting a $1/k^2$ dependence of the fluctuation spectrum. However, based on a dislocation model, Rottman [114] predicted that the energy of the thermal fluctuations of low-angle grain boundaries is linear in wave number, thereby implying a $1/k$ dependence of $< A^2(k) >$. A very recent work by Karma et al. [73] provides fresh insight into the deformation mechanisms that lead to these differences in the fluctuation spectra for low-angle and high-angle GBs. They show that the $1/k$ scaling behavior is associated with shear-coupled motion of GBs, and is exhibited by low-angle grain boundaries even at high temperatures. They derive the relation between equilibrium fluctuations and the coupling factor as

$$< A^2(k) >= \frac{k_B T}{SC\beta^2 k}, \tag{2.6}$$

where C is a parameter comprising of the elastic constants of the material, while $\beta = v_{||}/v_n$ was defined by Cahn et al. [115] as the coupling factor between the applied shear velocity ($v_{||}$) and the resulting normal GB velocity ($v_n$). In

contrast to low angle GBs, high angle GBs exhibit a $1/k^2$ scaling law at high temperatures attributed to capillarity-induced fluctuations, and a $1/k$ dependence at low temperatures. This transition is associated with a transition in the kinetics of the GBs from shear coupling to pure sliding. The same conclusions were drawn by Cahn et al. [115] based on their molecular dynamics simulations of shear deformation of bicrystals with various low-angle and high-angle GBs. At low and intermediate temperatures, the normal motion of all GBs was coupled to shear deformation. However, at high temperatures, the high-angle GBs showed a transition to pure sliding and spontaneous normal motion and the shear coupling vanished, while the low-angle GBs still retained their coupled response up to near the melting point.

Taken together, our simulations show that coherent TBs, which are also high angle tilt boundaries, do not exhibit any capillarity-induced fluctuations even at high temperatures, in sharp contrast to other high angle GBs. In fact, the thermal fluctuations indicate that the TB motion remains strongly coupled to shear deformation up to 0.95 homologous temperature. These conclusions are also in agreement with our prior simulations of the high temperature shearing of twinned bicrystals in which we observed that, unlike many high-angle GBs studied by Cahn et al. [115], the TBs do not exhibit sliding or spontaneous normal motion at high temperatures [116].

## 2.4 Conclusion

Our study provides important insights into the high temperature stability of nanotwinned structures. While nanocrystalline materials are known to be prone to grain growth and creep due to grain boundary normal motion and grain boundary sliding, respectively, our simulations indicate that the twin boundaries

do not exhibit sliding or spontaneous normal motion even at high temperatures and hence predict stable twin lamella at high temperatures. This is in qualitative agreement with the recent experimental studies by Bezares et al. [107] which reveal enhanced stability of nanotwinned FCC metals under nanoindentation and creep tests compared to their nanocrystalline counterparts. However, more detailed simulations of nanotwinned structures are needed to shed light on the interplay of grain boundaries and twin boundaries in determining the overall grain stability as well as the effect of pre-existing defects in these interfaces, which will be pursued in our future work. It should also be insightful to investigate the interactions of fluctuating twin boundaries and explore their role in governing the critical twin lamella thickness for optimal properties. Thus, our study furnishes a mechanistic understanding of the enhanced stability of twin lamella at high temperatures, as opposed to high angle grain boundaries, and opens up further avenues for materials design.

# Chapter 3 Entropic Interaction between Fluctuating Twin Boundaries

## 3.1 Introduction

Nanotwinned (NT) face-centered-crystal (FCC) metals are designed by the introduction of coherent twin boundaries (CTBs) within ultra-fine crystalline metals having a grain size of a few hundred nanometers. The typical twin lamella thickness within each grain ranges between 20-100 nm. The numerous studies performed till date reveal that the CTBs have a very high shear strength compared to most grain boundaries (GBs) and are also effective barriers to dislocation motion leading to a Hall-Petch type strengthening mechanism [48, 49, 50]. However, a unique feature of the CTBs is that the twin planes are also slip planes for FCC metals which enables them to accommodate large plastic strains by absorption of dislocations thus enhancing ductility [47]. In addition, experimental studies have revealed even more promising characteristics such as enhanced creep response, good thermal stability, and radiation response owing to the presence of both twin and grain boundaries [107, 117, 118]. Very recently, Jang et al. [53], and Wang et al. [54] have even fabricated nanotwinned nanowires with twin spacing on the order of a few angstroms. The smallest twin lamella has only two atomic layers separating adjacent twin boundaries. Through combined experimental and computational studies, Wang et al. [54] have shown that these nanowires with ultra-high density twins exhibit yield strength close to the theoretical strength of the metal. While these superior properties certainly open up exciting avenues for the applications of NT materials, they also call for a critical examination of the stability of these structural motifs especially at high temperatures. By structural

instability we imply processes such as grain growth, which are intimately connected to properties like interfacial stiffness, mobility, as well as the interaction of the constituting interfaces, such as GBs and TBs. An analysis of the thermal fluctuations based on statistical mechanics provides a convenient and powerful approach to gain insight into these interfacial properties.

There is a rich literature on the statistical thermodynamics of membranes which was primarily developed for soft materials– fluid and polymerized membranes– that exhibit large fluctuations [86, 87]. Based on the equilibrium thermal fluctuations, membrane theory enables estimates for quantities such as bending stiffness, and surface tension. In recent years, the membrane theory has also been applied to study crystalline membranes such as graphene and other two-dimensional materials [89, 90], as well as crystalline interfaces, such as GBs, and solid-liquid interfaces [69, 70, 72] based on thermal fluctuations. In the case of solid interfaces, the central idea is that the energetic cost for the out-of-plane fluctuation of the interface, which naturally involves deformation of the adjoining bulk regions, is used to construct an energy associated only with the interface. Then the surrounding bulk can be neglected and the interface is regarded as a membrane with an appropriate elastic energy. For instance, several high angle GBs in FCC metals exhibit capillarity induced fluctuations. This means that they can be modeled as membranes whose out-of-plane fluctuations are governed by surface tension, or more precisely, interfacial stiffness.

Studies based on thermal fluctuations have also shown that membranes exert a repulsive entropic pressure on each other, due to steric effects, that depends on the inter-membrane distance [119, 120, 121, 122, 123, 124]. Unlike the extensive work on the steric interaction of membranes, the effect of the presence of multiple GBs on their thermal fluctuations has not been addressed before. This becomes more relevant in the light of the recent fabrication of NT metals with twin bound-

ary spacing on the order of angstroms. Motivated by the striking resemblance between a stack of fluctuating biomembranes and an array of parallel fluctuating twin boundaries (Figure 3.1), we seek to elucidate the entropic interaction between fluctuating twin boundaries constituting a nanotwinned structure at finite temperature.

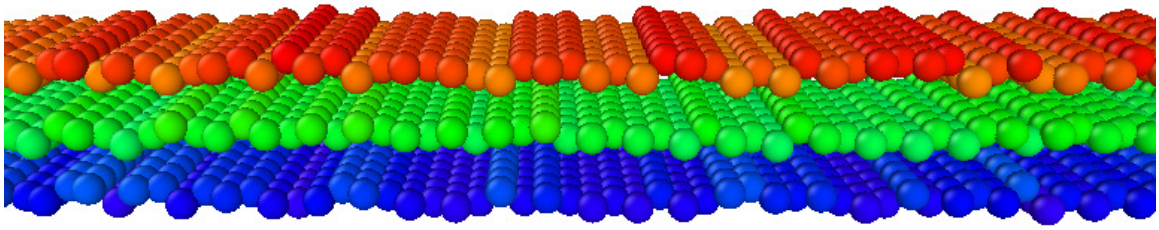

Figure 3.1: Atomistic structure of a section of the NT specimen depicting parallel coherent TBs fluctuating at 800K. Only the atoms with non-zero centrosymmetry parameter (comprising the TBs) are shown [28].

The Chapter is organized as follows. Section 3.2 provides a review of the theory of equilibrium thermal fluctuations applied to fluid membranes and different types of crystalline membranes and interfaces. The modeling of entropic interaction between multiple membranes and the effect of this entropic force on their fluctuation spectrum is also briefly discussed. Section 3.3 presents the molecular dynamics simulations of the thermal fluctuations of multiple CTBs as a function of twin boundary spacing. Section 3.4 presents the statistical mechanics based analysis of the entropic interactions between fluctuating CTBs. The summary and potential ramifications of these findings are discussed in Section 3.5.

## 3.2 Brief Review of Equilibrium Thermal Fluctuations

We begin by providing a brief review of the statistical mechanics of membranes. To be specific, we demonstrate that how the thermal fluctuation spectra for different membranes and interfaces are related to their interfacial properties.

### 3.2.1 Fluctuation Spectrum of a Free Membrane

For a fluctuating fluid membrane (Figure 3.2), the energetic cost for the out-of-plane fluctuations arises from the bending stiffness of the membrane. To understand this, we first treat the membrane as a quasi-one dimensional interface that is thin in one direction, such that the fluctuation along this axis can be ignored (Figure 3.3). Let $b$ be the width of the thin dimension and $W$ be the length of the longer dimension, and $h(x)$ be the out-of-plane displacement. Then the

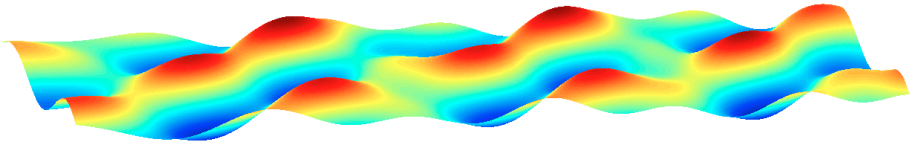

Figure 3.2: Schematic diagram of a freely fluctuating membrane. Different colors indicate different out of plane displacements [88].

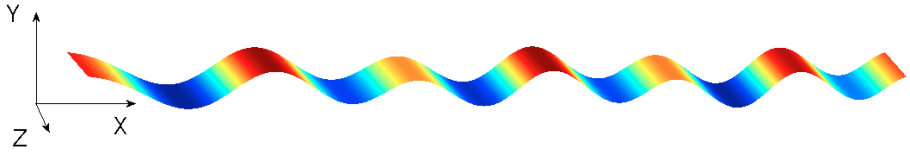


Figure 3.3: A fluctuating membrane approximated as quasi one-dimensional with $b \ll W$, where $W$ is the length in the direction of wave propagation (X axis), and $b$ is the width in the Z-direction [88].

Hamiltonian can be written as

$$\mathcal{H} = b \int_0^W \frac{1}{2}\kappa[h''(x)]^2 dx, \tag{3.1}$$

where $\kappa$ is the bending modulus, and $h''(x)$ is the mean curvature. Expanding $h(x)$ in Fourier space,

$$h(x) = \sum A(k) e^{ikx}, \tag{3.2}$$

the Hamiltonian can be expressed in the form

$$\mathcal{H} = \frac{1}{2} bW\kappa \sum_k k^4 A^2(k). \tag{3.3}$$

This energy is quadratic in $A(k)$. Using equipartition of energy, we obtain the relationship between the mean square fluctuation spectrum and the wave vector as

$$< A^2(k) >= \frac{k_B T}{bW\kappa k^4}, \tag{3.4}$$

where $<>$ means thermal average. Lipid bilayers, graphene and other two-dimensional materials are known to follow this relation. The fluctuations of many GBs and crystal-melt interfaces can also be modeled in a similar fashion. Previous studies [69, 72] showed that the fluctuations of high angle GBs and solid-liquid interfaces in FCC metals can be well described using the capillarity or the surface tension model as

$$< A^2(k) >= \frac{k_B T}{bW\Gamma k^2}, \tag{3.5}$$

where $\Gamma$ is the grain boundary stiffness analogous to the surface tension. However, not all GBs exhibit capillarity induced fluctuations. A recent work [73] revealed that GBs that undergo shear-coupled normal motion, such as many low-angle GBs, display a significantly different response and derived a modified expression for thermal fluctuations as

$$< A^2(k) >= \frac{k_B T}{bWC\beta^2 k}. \tag{3.6}$$

Here, $C$ is a parameter comprising of the elastic constants of the materials, and $\beta$ is a coupling factor defined as

$$\beta = v_{||}/v_n. \tag{3.7}$$

Introduced by [115], $\beta$ characterizes the coupling relationship between the velocity parallel to the GB ($v_{||}$) and the concomitant normal GB velocity ($v_n$) during shear coupled normal motion. Our previous work [112] further reveals that CTBs also follow this behavior (Equation 3.6) since they exhibit shear coupled normal motion. We note that although lipid membranes, high angle GBs, and CTBs display a different relationship between their fluctuation spectrum $A(k)$ and the wave vector $k$ (Equation 3.4, 3.5, and 3.6, respectively), they all essentially follow a power law with different exponents for $k$.

### 3.2.2 Fluctuation Spectrum of a Confined Membrane

The fact that a membrane fluctuating close to adjacent surfaces, such as in a multilayer system, experiences an effective repulsive pressure arising from confinement was first introduced by [119]. The commonly used model can be represented by a simpler problem of modeling the fluctuations of a single membrane constrained by two rigid plates, as shown in Figure 3.4. Contrary to an unconfined membrane, there is a constraint on the out-of-plane deflection $h(x, y)$ that

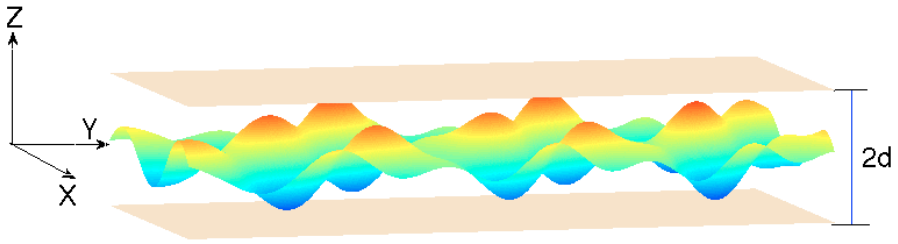


Figure 3.4: Schematic of a confined membrane fluctuating between two rigid plates [88].

$$-d \leq h(x,y) \leq d, \tag{3.8}$$

where the rigid plates are separated by a distance $2d$. Recognizing the difficulty of imposing this constraint inequality, many researchers [122, 123, 125, 126, 127, 128] proposed a 'soft constraint' to replace Equation 3.8. Specifically, it is assumed that the net result of the confinement is that the membrane experiences an effective harmonic potential that can be introduced as an additional term in the Hamiltonian. This modifies Equation 3.1 to

$$\mathcal{H} = b \int_0^W \frac{1}{2}[\kappa(h''(x))^2 + \omega h^2(x)]dx, \tag{3.9}$$

where $\omega$ is a constant that accounts for the confinement. Thus the mean square fluctuation spectrum becomes

$$< A^2(k) >= \frac{k_B T}{bW(\kappa k^4 + \omega)}. \tag{3.10}$$

It is evident that the effect of $\omega$ can be ignored for small wavelength. However, at long wavelength or small $k$, $\omega$ is the dominant term and the fluctuation spectrum becomes independent of $k$. This is represented in Figure 3.5 which plots Equation 3.10. We should note that this figure is just for showing the interaction force effect does not represent any real membrane fluctuation spectrum case This implies that the repulsive force between fluctuating membranes arising from the steric interactions inhibits their fluctuations especially in the long wavelength modes. This correlation between repulsive force and suppression of fluctuations also appears in the entropic interaction between solid-liquid interfaces [69] and crystalline membranes such as bilayer graphene [129]. Thus, we conclude that membranes and interfaces whose free (unconstrained) fluctuations follow Equation 3.4 or Equation 3.5 exhibit a suppression of long wavelength fluctuations under confinement owing to the repulsive nature of entropic interactions. In the

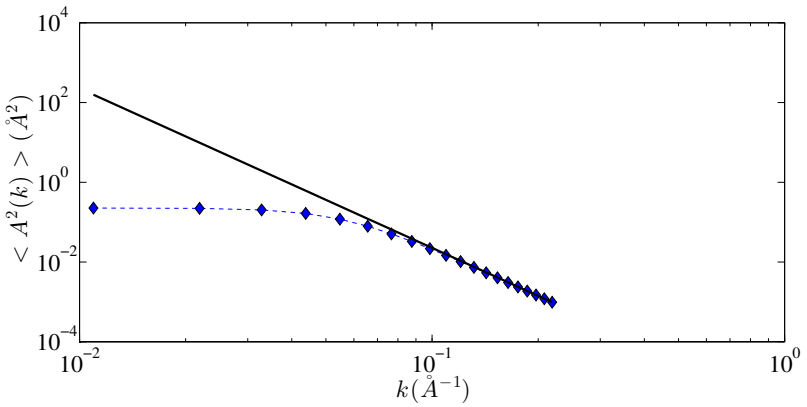


Figure 3.5: Mean square of out-of-plane displacement component $< A^2(k) >$ respect to wave vector $k$ for free membrane (solid black line), membranes with confinement (dotted blue line) [88].

following sections, we examine the entropic interactions and effect on fluctuations of multiple CTBs, or in general, interfaces whose free fluctuations follow Equation 3.6.

## 3.3 Thermal Fluctuations of Multiple Twin Boundaries

### 3.3.1 Simulation Method

We first present our molecular dynamics simulations that examine the thermal fluctuations of multiple, parallel CTBs as a function of the twin boundary spacing. The nanotwinned structures were modeled by way of molecular dynamics simulations using LAMMPS [110]. All simulations were performed on Cu using the embedded-atom-method (EAM) interatomic potential developed by Mishin et al. [111]. As shown in Figure 3.6, the specimen were oriented along the $[\bar{1}12]$, $[\bar{1}1\bar{1}]$ , and $[\bar{1}\bar{1}0]$ crystallographic directions. Equally spaced CTBs separated by distance d are shown by red colored atoms. The rest of the face-centered-cubic atoms are shown in blue color. Thus, the Y-direction was aligned normal to the

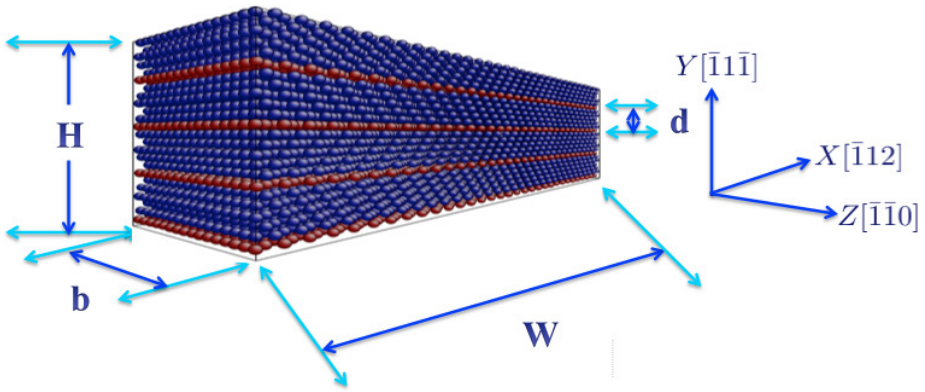


Figure 3.6: Atomistic structure of a nanotwinned specimen showing the crystallographic orientation [88].

plane of the twin boundaries. The simulation cell dimensions in the lateral (X and Z) directions were $W \approx 56$ nm, and $b \approx 1.9$ nm, with periodic boundary conditions applied in both directions. Since the length in the Z-direction is much smaller than that in the X-direction ($b \ll W$), fluctuations along the Z-direction can be ignored. Thus, the problem can be regarded as quasi-one dimensional. The CTB spacing was varied from 0.6 nm to 12 nm. As shown in Figure 3.7, each specimen with a different CTB spacing had a different height in the Y-direction since the number of CTBs was held fixed at $N = 4$ (including one CTB located at the top/bottom end of the specimen due to periodicity).

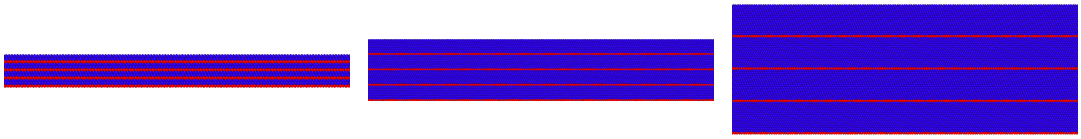

Figure 3.7: Atomistic structure of a typical specimen with a single CTB ($N = 4$) and different $d$ (a) d = 0.6nm; (b) d = 1.8nm; (c) d = 3.0nm. The cyan atoms show the CTB [88].

### 3.3.2 Simulation Results

Figure 3.8 shows the variation of the fluctuation spectrum of a CTB as a function of the wave vector $k$ in the presence of multiple parallel CTBs. We

note that the different curves have been shifted for a better comparison, thus the $< |A(k)|^2 >$ in vertical axis do not represent the real values. For clarity, only

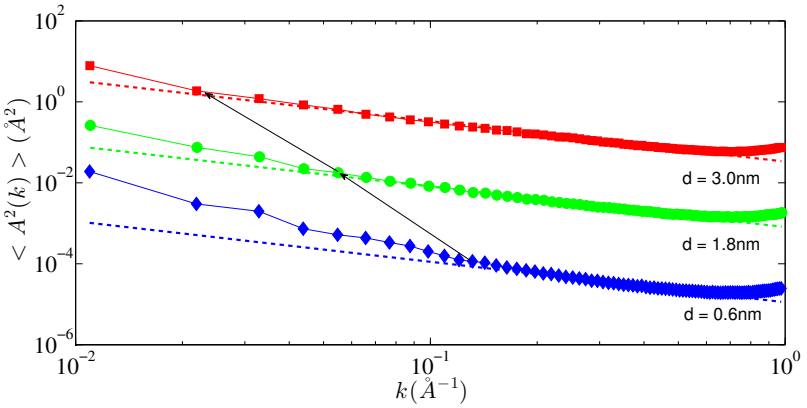


Figure 3.8: Fluctuation spectrum as a function of wave vector for different twin spacing $d$ [88].

the simulation results for 0.6 nm, 1.8 nm, and 3.0 nm twin boundary spacings are shown. We first observe that in the presence of adjoining CTBs, the long wavelength fluctuation modes of CTBs are enhanced. This is in sharp contrast to other interfaces discussed earlier which exhibit a suppression of fluctuations. We further note that as the twin boundary spacing $d$ decreases, more fluctuation modes are affected (and enhanced). For example, for a twin boundary spacing of 0.6 nm, the fluctuation with wavelength greater than 4 nm are amplified, whereas if the spacing is 3.0 nm, only the wavelengths greater than 30 nm are amplified. Examining the mean square of the out-of-plane displacement in real space $< h^2 >$ also yields the same trend. Figure 3.9 shows that as the twin boundary spacing decreases, the out-of-plane displacements of the CTBs are enhanced. The effect of neighboring CTBs is diminished beyond a CTB spacing of 3 nm

In order to verify whether this behavior is unique to CTBs and not a common characteristic of all solid-solid interfaces separated by a crystalline matrix, we also performed a series of molecular dynamics simulations on specimens containing multiple GBs, instead of CTBs, to extract the change in their fluctuations due to

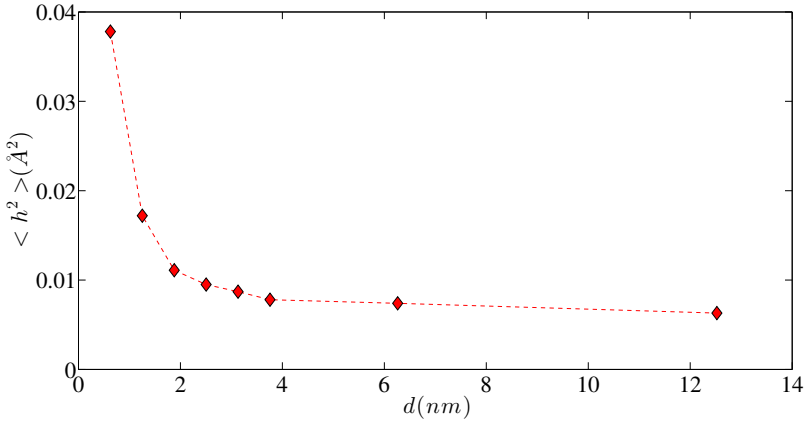


Figure 3.9: Mean square out-of-plane displacement $< h^2 >$ in real space as a function of twin spacing $d$. The horizontal axis represent the relative twin spacing length compared with NT structure length $W$ [88].

confinement. The simulation procedure was similar to that described above and the specimen consisted of parallel $\Sigma 5(310)$ GBs with periodic boundary conditions in all directions. We specifically selected a high-angle GB since they exhibit capillarity induced fluctuations under unconfined conditions as represented by Equation 3.5, unlike unconfined CTBs which follow Equation 3.7. As expected, Figure 3.10 shows that such high angle GBs experience a noticeable suppression of the long wavelength modes similar to fluid membranes.

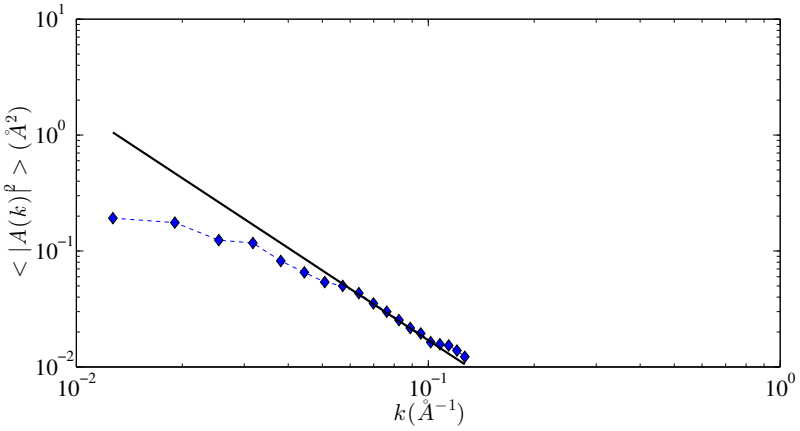


Figure 3.10: Fluctuation spectrum as a function of wave vector $k$ for a single $\Sigma 5(310)$ high-angle GB (solid line), and multiple GBs (dashed line). The solid line has a slope of -2 as expected from Equation 3.5 [88].

## 3.4 Entropic Interaction between Fluctuating Twin Boundaries

As mentioned above, since fluid membranes are flexible and undergo large fluctuations, they exert a repulsive force on each other as they come close. Starting with the pioneering work of [119], this repulsive steric interaction has been studied using the classical model of a membrane fluctuating between two rigid plates [120, 121, 122, 123, 124]. In contrast to fluid membranes, the twin boundaries are separated by a crystalline matrix which also undergoes deformation to accommodate the fluctuations of the neighboring interfaces. Specifically, the out-of-plane fluctuations of the CTBs are accommodated by localized shear-coupled normal motion which induces strain fields in the elastically deformable matrix [112]. Hence, the rigid plate model is not suitable for this case. Instead, we begin by formulating a linear elastic boundary value problem for two fluctuating CTBs and calculating the strain energy based on the continuum model proposed by Karma et al. [73]. We then calculate the associated Hemholtz free energy for this system as a function of the twin boundary spacing $2d$, to finally obtain the entropic force. We note that the problem addressed here as well our approach is similar in some aspects to the statistical mechanics based study of interaction between fluctuating dislocations by Rickman et al. [130]. Interestingly, they also find that the entropic contribution to the force between dislocations at finite temperature is attractive.

### 3.4.1 Boundary Value Problem

Figure 3.11a shows the schematic of two fluctuating twin boundaries (denoted by CTB-1 and CTB-2) under thermal equilibrium with their flat configurations located at distance $d$ above and below the $x$ axis respectively. Similar to our

atomistic simulations, the length in the $x$ direction is denoted by $W$, and the thickness in the $z$ direction is denoted by $b$ and points out of the plane of the paper. With $b \ll W$, the problem is treated as quasi one-dimensional. We describe the out-of-plane displacements of the two CTBs by functions $h^1(x)$ and $h^2(x)$ which can be expanded in Fourier series as

$$h^1(x) = \sum_{i=0}^{N} \hat{h}_i^1 = \sum_{i=0}^{N} [a_i \cos(k_i x) + c_i \sin(k_i x)] \; and \tag{3.11a}$$

$$h^2(x) = \sum_{j=0}^{N} \hat{h}_j^2 = \sum_{j=0}^{N} [b_j \cos(k_j x) + d_j \sin(k_j x)], \tag{3.11b}$$

where $N = \frac{W}{l_0}$, $l_0$ being the minimum lattice distance along the $x$ direction, $a_i \equiv a(k_i)$, $c_i \equiv c(k_i)$, $b_j \equiv b(k_j)$, $d_j \equiv d(k_j)$, and $k_i = \frac{2\pi}{W} i$ is the wave vector. The first task is to obtain the strain energy, which we denote by $E(h^1, h^2)$, induced by these two perturbations $h^1(x)$ and $h^2(x)$. For simplicity, we first consider a pair

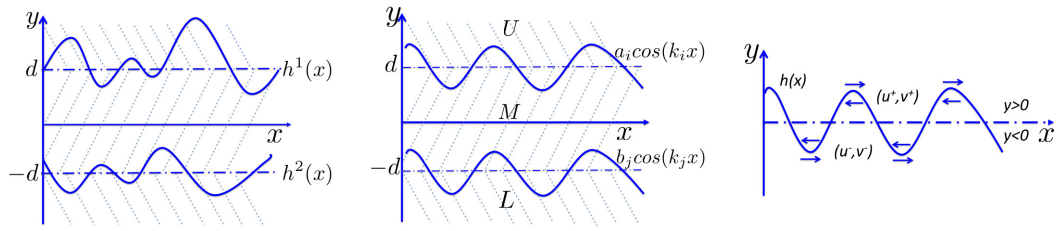


Figure 3.11: Schematic of the continuum model for interactions of CTBs [88].

of single cosine modes, as shown in Figure 3.11b. Due to the coupling relation, Equation 3.7, the perturbations of both CTBs must induce shear strains in the adjoining grains, as shown in Figure 3.11c. Thus, the problem of computing the strain energy of a pair of CTBs fluctuating as cosine modes is reduced to calculating the associated strain field in the crystalline matrix. To this end, we first define three regions, namely, $U$ (upper) for $y \geq d$, $L$ (lower) for $y \leq -d$ and $M$ (middle) for $-d \leq y \leq d$ (Figure 3.11b). Let $u$ and $v$ be the $x$ and $y$ components of the displacement vector respectively. The components of the displacement field in the three regions are denoted by $(u^U(x,y), v^U(x,y))$, $(u^M(x,y), v^M(x,y))$ and

$(u^L(x,y), v^L(x,y))$. Assuming isotropic linear elasticity, these fields satisfy the following equilibrium equations:

$$(\partial_x^2 + \partial_y^2)u^R + \frac{1}{1-2\nu}\partial_x(\partial_x u^R + \partial_y v^R) = 0 \quad and \tag{3.12a}$$

$$(\partial_x^2 + \partial_y^2)v^R + \frac{1}{1-2\nu}\partial_y(\partial_x u^R + \partial_y v^R) = 0, \tag{3.12b}$$

with $\nu$ being the Poisson's ratio, and $R$ taking values $U$,$M$, and $L$, subject to the following boundary conditions:

$$u^U(x,d) - u^M(x,d) = \beta h^1(x) = \beta a_i \cos(k_i x), \tag{3.13a}$$

$$u^M(x,-d) - u^L(x,-d) = -\beta h^2(x) = -\beta b_j \cos(k_j x), \tag{3.13b}$$

$$v^U(x,d) = v^M(x,d), \tag{3.13c}$$

$$v^M(x,-d) = v^L(x,-d), \tag{3.13d}$$

$$\sigma_{yy}^U(x,d) = \sigma_{yy}^M(x,d), \tag{3.13e}$$

$$\sigma_{yy}^M(x,-d) = \sigma_{yy}^L(x,-d), \tag{3.13f}$$

$$\sigma_{xy}^U(x,d) = \sigma_{xy}^M(x,d), \tag{3.13g}$$

$$\sigma_{xy}^M(x,-d) = \sigma_{xy}^L(x,-d), \; and \tag{3.13h}$$

$$u^U(x,\infty) = u^L(x,-\infty) = v^U(x,\infty) = v^L(x,-\infty) = 0. \tag{3.13i}$$

Equation 3.13a and Equation 3.13b indicate that the normal displacements of the CTBs corresponding to $h^1(x)$ and $h^2(x)$ must be coupled to relative tangential translations of the adjoining regions of the matrix and twin by $\beta h^1(x)$ and $-\beta h^2(x)$ respectively. We should note here that the minus sign in Equation 3.13b signifies that these two CTBs have reversed crystallographic orientations of the grains above and below. Thus, the direction of the shear coupled normal motion experienced by CTB-1 and CTB-2 is reversed. Equation 3.13c and Equation 3.13d enforce the continuity of the normal displacement. Equation 3.13e, 3.13f, 3.13g, 3.13h are continuity equations for the normal and shear components of the

traction vector at the interfaces where the normal stress is given by

$$\sigma^R_{yy}(x,y) = \lambda \partial_x u^R(x,y) + (\lambda + 2\mu)\partial_y v^R(x,y), \tag{3.14}$$

and the shear stress is given by

$$\sigma^R_{xy}(x,y) = \mu[\partial_x v^R(x,y) + \partial_y u^R(x,y)]. \tag{3.15}$$

Finally, Equation 3.13a implement the far field boundary conditions. To circumvent the problem of directly solving the boundary value problem with these complicated boundary conditions, we decompose it into two simpler independent boundary value problems using the linearity of Equation 3.12. Specifically, the complete displacement field is constructed by superimposing the displacement field induced by CTB-1 with perturbation $h^1(x) = a_i \cos(k_i x)$ and coupling coefficient $\beta$ located at $y = d$, and that induced by CTB-2 with perturbation $h^2(x) = b_j \cos(k_j x)$ and coupling coefficient $-\beta$ located at $y = -d$ (Figure3.12). Karma [73] obtained the following displacement field induced by a perturbation $h(x) = a(k)\cos(kx)$ of an interface with coupling coefficient $\beta$ located by $y = 0$, as shown in Figure 3.11c:

$$u = \left[\frac{\beta a(k)}{2}\operatorname{sgn}(y) - \frac{\beta a(k)}{4(1-\nu)}ky\right] e^{-k|y|}\cos kx \; and \tag{3.16a}$$

$$v = \left[\frac{\beta a(k)}{4(1-\nu)}(1-2\nu) + \frac{\beta a(k)}{4(1-\nu)}\operatorname{sgn}(y)ky\right] e^{-k|y|}\sin kx. \tag{3.16b}$$

Translating this solution in order to obtain the displacement field induced by perturbations located at $y = d$ and $y = -d$ respectively, and then superimposing them, we have the complete displacement field as follows:

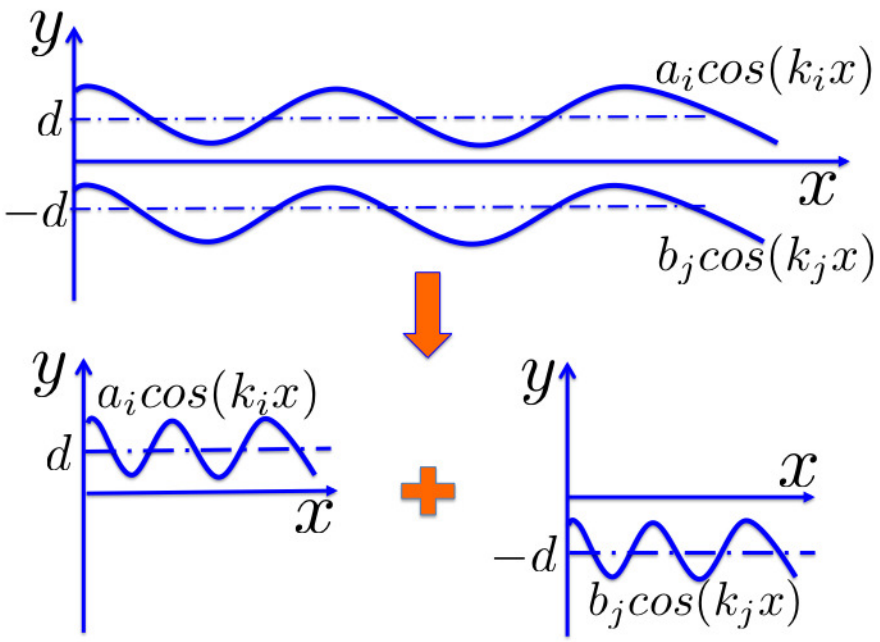


Figure 3.12: Decomposition of the complete displacement field due to two fluctuating CTBs into two simpler cases involving a single fluctuating CTB at different locations [88].

in region $U$,

$$\begin{aligned} u^U(x,y) &= \frac{\beta a_i}{2}\left[1-\frac{k_i(y-d)}{2(1-\nu)}\right]e^{-k_i(y-d)}\cos k_i x + \\ &\quad \frac{-\beta b_j}{2}\left[1-\frac{k_j(y+d)}{2(1-\nu)}\right]e^{-k_j(y+d)}\cos k_j x, \\ v^U(x,y) &= \frac{\beta a_i}{4(1-\nu)}[1-2\nu+k_i(y-d)]e^{-k_i(y-d)}\sin k_i x + \\ &\quad \frac{-\beta b_j}{4(1-\nu)}[1-2\nu+k_j(y+d)]e^{-k_j(y+d)}\sin k_j x; \end{aligned} \tag{3.17}$$

in region $M$,

$$\begin{aligned} u^M(x,y) &= \frac{-\beta a_i}{2}\left[1+\frac{k_i(y-d)}{2(1-\nu)}\right]e^{-k_i(y-d)}\cos k_i x + \\ &\quad \frac{-\beta b_j}{2}\left[1-\frac{k_j(y+d)}{2(1-\nu)}\right]e^{-k_j(y+d)}\cos k_j x, \\ v^M(x,y) &= \frac{\beta a_i}{4(1-\nu)}[1-2\nu-k_i(y-d)]e^{-k_1(y-d)}\sin k_i x + \\ &\quad \frac{-\beta b_j}{4(1-\nu)}[1-2\nu+k_j(y+d)]e^{-k_j(y+d)}\sin k_j x; \end{aligned} \tag{3.18}$$

and in region $L$,

$$\begin{aligned} u^L(x,y) = \frac{-\beta a_i}{2}\left[1+\frac{k_i(y-d)}{2(1-\nu)}\right]e^{-k_i(y-d)}\cos k_i x + \\ \frac{\beta b_j}{2}\left[1+\frac{k_j(y+d)}{2(1-\nu)}\right]e^{-k_j(y+d)}\cos k_j x, \\ v^L(x,y) = \frac{\beta a_i}{4(1-\nu)}[1-2\nu-k_i(y-d)]e^{-k_i(y-d)}\sin k_i x + \\ \frac{-\beta b_j}{4(1-\nu)}[1-2\nu-k_j(y+d)]e^{-k_j(y+d)}\sin k_j x. \end{aligned} \tag{3.19}$$

### 3.4.2 Strain Energy

Having determined the displacement field, we can now calculate the total strain energy associated with the cosine mode perturbations of the two CTBs. Using the periodicity of the perturbations, $h^1(x)$, and $h^2(x)$, the strain energy is expressed as [73]

$$\begin{aligned} E(a_i,b_j) = \frac{bW}{\Lambda}[\int_0^\Lambda dx\int_d^\infty e(u^U,v^U)dy + \int_0^\Lambda dx\int_{-d}^{d} e(u^M,v^M)dy + \\ \int_0^\Lambda dx\int_{-\infty}^{-d} e(u^L,v^L)dy], \end{aligned} \tag{3.20}$$

where $\Lambda$ is introduced as the least common multiple of the wavelengths $2\pi/k_i$ and $2\pi/k_j$ of the fluctuations of CTB-1 and CTB-2, respectively. $W$ is assumed to be a large integer multiple of $\Lambda$. $e(u^U,v^U)$, $e(u^M,v^M)$, and $e(u^L,v^L)$ are the elastic energy densities in the regions $U$, $M$, and $L$, respectively, and are given by

$$e(u^R,v^R) = \mu\frac{1-\nu}{1-2\nu}\left(\frac{\partial u^R}{\partial x}+\frac{\partial v^R}{\partial y}\right)^2 + \frac{\mu}{2}\left(\frac{\partial u^R}{\partial y}+\frac{\partial v^R}{\partial x}\right)^2 - 2\mu\frac{\partial u^R}{\partial x}\frac{\partial v^R}{\partial y}, \tag{3.21}$$

where, $R$ represents $U$,$M$, and $L$ respectively.

The integrals over $x$ are evaluated using the relations

$$\frac{1}{\Lambda}\int_0^\Lambda \sin(k_i x)\sin(k_j x)dx = \frac{1}{\Lambda}\int_0^\Lambda \cos(k_i x)\cos(k_j x)dx = \frac{1}{2}\delta_{ij}, \tag{3.22}$$

where $\delta_{ij}$ is the Kronecker delta, and

$$\frac{1}{\Lambda}\int_0^\Lambda \sin(k_i x)\cos(k_j x)dx = \frac{1}{\Lambda}\int_0^\Lambda \cos(k_i x)\sin(k_j x)dx = 0. \tag{3.23}$$

All the integrals over $y$ can also be computed analytically. Summing up the contributions after integration over both $x$ and $y$, we obtain

$$E(a_i, b_j) = \frac{bW\beta^2\mu a_i^2 k_i}{8(1-\nu)} + \frac{bW\beta^2\mu b_j^2 k_j}{8(1-\nu)} - \delta_{ij}\frac{bW\beta^2\mu a_i b_j k_i^2}{4(1-\nu)} e^{-2k_i d}(\frac{1}{k_i} - 2d). \quad (3.24)$$

We note that the first two terms consisting of $a_i^2$ and $b_j^2$, represent the contribution from the self-energy induced by independent fluctuations of the CTBs. The last term consisting of the product, $a_i b_j$, represents the interaction energy between CTB-1 and CTB-2. Naturally, the separation distance $2d$ enters the energy expression through the interaction term. Following the above calculations, the strain energy associated with CTB-1 and CTB-2 undergoing sine mode fluctuations, $c_i \sin(k_i x)$ and $d_j \sin(k_j x)$, respectively, can also be evaluated as

$$E(c_i, d_j) = \frac{bW\beta^2\mu c_i^2 k_i}{8(1-\nu)} + \frac{bW\beta^2\mu d_j^2 k_j}{8(1-\nu)} - \delta_{ij}\frac{bW\beta^2\mu c_i d_j k_i^2}{4(1-\nu)} e^{-2k_i d}(\frac{1}{k_i} - 2d). \quad (3.25)$$

Finally, we consider the remaining two scenarios. When CTB-1 undergoes fluctuation $a_i \cos(k_i x)$, and CTB-2 undergoes fluctuation $d_j \sin(k_j x)$, or when CTB-1 undergoes fluctuation $c_i \sin(k_i x)$, and CTB-2 undergoes fluctuation $b_j \cos(k_j x)$, it can be seen that the interaction energy is zero owing to Equation 3.23.

We are now ready to evaluate the total strain energy, $E(h^1, h^2)$, as a sum over the contribution from the self-energy and interaction energy for all the modes. Thus, evaluating the kronecker delta in Equations 3.24 and 3.25, we have

$$\begin{aligned} E(h^1, h^2) &= \sum_{i,j} E(\hat{h}_i^1, \hat{h}_j^2) \\ &= \sum_{i,j} [E(a_i, b_j) + E(c_i, d_j)] \\ &= \sum_i [\frac{bW\beta\mu a_i^2 k_i}{8(1-\nu)} + \frac{bW\beta\mu b_i^2 k_i}{8(1-\nu)} - \frac{bW\beta\mu a_i b_i k_i^2}{4(1-\nu)} e^{-2k_i d}(\frac{1}{k_i} - 2d) \\ &+ \frac{bW\beta\mu c_i^2 k_i}{8(1-\nu)} + \frac{bW\beta\mu d_i^2 k_i}{8(1-\nu)} - \frac{bW\beta\mu c_i d_i k_i^2}{4(1-\nu)} e^{-2k_i d}(\frac{1}{k_i} - 2d)]. \end{aligned} \quad (3.26)$$

### 3.4.3 Helmholtz Free Energy and Entropic Force

In order to obtain the Helmholtz free energy of the system, we first construct the partition function $Z_i$ for wave vector $k_i$, using the strain energy corresponding to the wave vector $k_i$

$$\begin{aligned} E_i = &\frac{bW\beta\mu a_i^2 k_i}{8(1-\nu)} + \frac{bW\beta\mu b_i^2 k_i}{8(1-\nu)} - \frac{bW\beta\mu a_i b_i k_i^2}{4(1-\nu)} e^{-2k_i d}(\frac{1}{k_i} - 2d) \\ &+ \frac{bW\beta\mu c_i^2 k_i}{8(1-\nu)} + \frac{bW\beta\mu d_i^2 k_i}{8(1-\nu)} - \frac{bW\beta\mu c_i d_i k_i^2}{4(1-\nu)} e^{-2k_i d}(\frac{1}{k_i} - 2d). \end{aligned} \tag{3.27}$$

Assuming the coupling parameter $\beta \simeq 1$, and introducing the following nondimensionalization

$$E_0 = \frac{bW^2\mu}{8(1-\nu)}\,,\ A_i = \frac{a_i}{W}\,,\ B_i = \frac{b_i}{W}\,,\ C_i = \frac{c_i}{W}\,,\ D_i = \frac{d_i}{W}\,,\ K_i = k_i W\,,\ \varphi = \frac{2d}{W}\,, \tag{3.28}$$

we get

$$\begin{aligned} E_i = &E_0 K_i A_i^2 + E_0 K_i B_i^2 - 2E_0 K_i A_i B_i e^{-K_i\varphi}(1 - K_i\varphi) \\ &+ E_0 K_i C_i^2 + E_0 K_i D_i^2 - 2E_0 K_i C_i D_i e^{-K_i\varphi}(1 - K_i\varphi). \end{aligned} \tag{3.29}$$

Then, the partition function corresponding to the wave vector $k_i$ is obtained as

$$\begin{aligned} Z_i &= \int_{-\infty}^{\infty} dA_i \int_{-\infty}^{\infty} dB_i \int_{-\infty}^{\infty} dC_i \int_{-\infty}^{\infty} dD_i e^{-\frac{E_i}{k_B T}} \\ &= [\int_{-\infty}^{\infty} dA_i \int_{-\infty}^{\infty} dB_i e^{-\frac{E_{iAB}}{k_B T}}]^2, \end{aligned} \tag{3.30}$$

where $E_{iAB} = E_0 K_i A_i^2 + E_0 K_i B_i^2 - 2E_0 K_i A_i B_i e^{-K_i\varphi}(1 - K_i\varphi)$. Let $P_i = \frac{E_0 K_i}{k_B T}$ and $Q_i = \frac{E_0 K_i}{k_B T} e^{-K_i\varphi}(1 - K_i\varphi)$. It is obvious that $P_i > Q_i > 0$, and then

$$\frac{E_{iAB}}{k_B T} = P_i A_i^2 + P_i B_i^2 - 2Q_i A_i B_i. \tag{3.31}$$

Introduce new variables $s_i = \sqrt{P}B_i + \sqrt{P}A_i, t_i = \sqrt{P}B_i - \sqrt{P}A_i$, and then

$$\frac{E_{iAB}}{k_B T} = \frac{P_i - Q_i}{2P_i} s_i^2 + \frac{P_i + Q_i}{2P_i} t_i^2. \tag{3.32}$$

Substituting into Equation 3.27, we obtain

$$\begin{aligned} Z_i &= \left[ \int_{-\infty}^{\infty} ds_i e^{-\frac{P_i - Q_i}{2P_i} s_i^2} \int_{-\infty}^{\infty} dt_i e^{-\frac{P_i + Q_i}{2P_i} t_i^2} \frac{1}{2P_i} \right]^2 \\ &= \frac{\pi^2}{P_i^2 - Q_i^2}. \end{aligned} \tag{3.33}$$

The complete partition function becomes

$$\begin{aligned} Z &= \prod_i^N Z_i = \prod_i^N \frac{\pi^2}{P_i^2 - Q_i^2} \\ &= \pi^{2N} \prod_i^N \frac{1}{P_i^2 - Q_i^2}. \end{aligned} \tag{3.34}$$

Then, the Helmholtz free energy is computed as

$$F = -k_B T \ln Z = k_B T \sum_i^N \ln(P_i^2 - Q_i^2) - 2N k_B T \ln \pi. \tag{3.35}$$

Finally, the entropic force is defined as [124]

$$f = -\frac{\partial F}{\partial (2d)} = -\frac{1}{W} \frac{\partial F}{\partial \varphi}. \tag{3.36}$$

Given the complexity of the summation, we evaluate Equation 3.36 numerically.

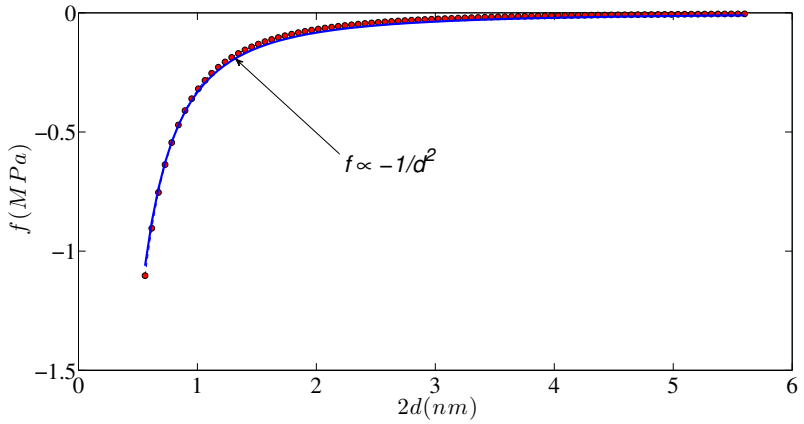


Figure 3.13: Entropic force as a function of twin spacing $2d$. The blue line is the fitting curve which shows $1/d^2$ dependence [88].

To this end, we use material properties for copper and other parameters that are consistent with our atomistic simulations: $W = 56$nm, $b = 1.9$m, $\mu = 56.64$GPa,

$T = 800$K, $\nu = 0.25$, $l_0 = 4.4275\mathring{A}$, $N = 126$. $l_0 = \sqrt{6}a/2$ (where $a = 3.615\mathring{A}$) is taken as the lattice parameter along the x axis which corresponds to the $[\bar{1}12]$ crystallographic direction. Figure 3.13 shows the entropic force between fluctuating CTBs versus twin spacing $2d$. It can be seen that the entropic interaction is indeed attractive and decays as $1/d^2$, that is to say

$$f \propto -\frac{1}{d^2}. \tag{3.37}$$

Comparing Figure 3.9 and Figure 3.13, it is somewhat surprising that an attractive force with a magnitude of just over 1 MPa for the smallest CTB spacing of 0.6 nm can lead to almost a doubling of the fluctuation amplitude. Nevertheless, our theoretical analysis confirms our previous conjecture that the entropic force between CTBs must be attractive given the enhancement of the CTB fluctuations observed in atomistic simulations.

## 3.5 Conclusion

In summary, we present a study of the interaction between twin boundaries at finite temperature using molecular dynamics simulations and statistical mechanics based on a continuum representation of a fluctuating twin boundary in an elastic medium. Our atomistic simulations reveal that as the spacing between twin boundaries decreases, their fluctuations are enhanced, and are almost doubled in the case of the smallest twin boundary spacing of $6\mathring{A}$. This is in contrast to many other crystalline interfaces such as high angle grain boundaries and crystal-melt interfaces, which exhibit a remarkable suppression of fluctuations in multilayer systems due to the repulsive nature of their entropic interactions. Our theoretical analysis of the entropic interaction of twin boundaries shows that there is indeed an attractive force between fluctuating twin boundaries which accounts for the increase in fluctuations observed in our simulations. The rather

surprising attractive force is attributed to the characteristic of twin boundaries to exhibit shear-coupled normal motion. Since our continuum model for a fluctuating twin boundary follows the work of Karma et al. [73] on the fluctuations of shear coupled grain boundaries, our findings should also be valid for low angle grain boundaries that exhibit shear-coupled normal motion. More generally, we conclude that for shear coupled grain boundaries, the entropic interaction is dominated by the deformation of the elastic medium between adjoining interfaces, and hence is fundamentally distinct from the entropic pressure resulting from steric hindrance. In fact, the entropic contribution to twin boundary interactions reported here is in qualitative agreement with the attractive nature of interactions between fluctuating dislocations at finite temperature observed by Rickman et al. [130].

# Chapter 4 Thermal Stress due to Twin Boundaries

## 4.1 Introduction

Research over the past decade has provided compelling evidence that a novel class of materials known as nanotwinned (NT) metals may be the optimal motifs for the design of high-strength high-ductility materials [28, 29, 31]. Nanotwinned FCC metals are designed by the introduction of coherent twin boundaries (CTBs) within ultra-fine crystalline metals having a grain size of a few hundred nanometers. The typical twin lamella thickness within each grain ranges between 20-100 nm. The numerous studies performed till date reveal that the CTBs have a very high shear strength compared to most grain boundaries (GBs) and are also effective barriers to dislocation motion. This leads to a Hall-Petch type strengthening mechanism associated with GBs [32, 49, 50]. However, a unique feature of the CTBs is that the twin planes are also slip planes for FCC metals which enables them to accommodate large plastic strains by absorption of dislocations thus enhancing ductility [47]. In addition, experimental studies have revealed more promising characteristics such as good creep response, thermal stability, and radiation response [107, 117, 118]. Very recent studies have made it possible to fabricate NT nanowires with twin spacing on the order of a mere few angstroms which demonstrate extraordinary strength [53, 54, 131]. The smallest twin lamella in these specimen has only two atomic layers separating adjacent TBs. While these superior nanostructures certainly open up exciting avenues for the applications of NT materials, they also call for a closer examination of the stability of these structural motifs especially at finite temperature. In this paper,

we perform atomistic simulations at high temperatures to compute the thermal stress due to the presence of twin boundaries as a function of the twin boundary spacing and explain our results by means of a simple thermal expansion based analysis.

## 4.2 Simulation Method

Molecular dynamics simulations were performed on Cu based on the embedded-atom-method (EAM) interatomic potential developed by Mishin et al. [111] using LAMMPS (Large-scale Atomic/Molecular Massively Parallel Simulator) [110]. As shown in Figure 4.1, the nanotwinned specimens were oriented along the $[\bar{1}12]$, $[\bar{1}1\bar{1}]$ , and $[\bar{1}\bar{1}0]$ crystallographic directions. Thus, the Y-direction was aligned normal to the plane of the twin boundaries. The simulation cell dimensions in the lateral (X and Z) directions were $L_x \approx 70\mathring{A}$, and $L_z \approx 70\mathring{A}$, with periodic boundary conditions applied in both directions. Simulations were performed for three different specimen heights, specifically, $124\mathring{A}$, $248\mathring{A}$, and $372\mathring{A}$, to take into account any dependence of the stress calculations on the length in the normal direction. The CTB spacing was varied from 0.6 nm to 6 nm. Since the CTB spacing was kept uniform within a specimen, each specimen with constant height but different CTB spacing contained different numbers of CTBs.

The simulation cell was first relaxed at zero temperature using energy minimization. Keeping the atoms on the upper and lower boundaries fixed, the structure was equilibrated at 800K by running molecular dynamics for 100 ps using the Nose-Hoover thermostat such that the stresses in the lateral directions were completely relaxed to zero. The virial stress formulation was used for estimating the average stress. We note that there is thermal stress in the Y-direction since it is not allowed to relax due to the fixed displacement boundary conditions at

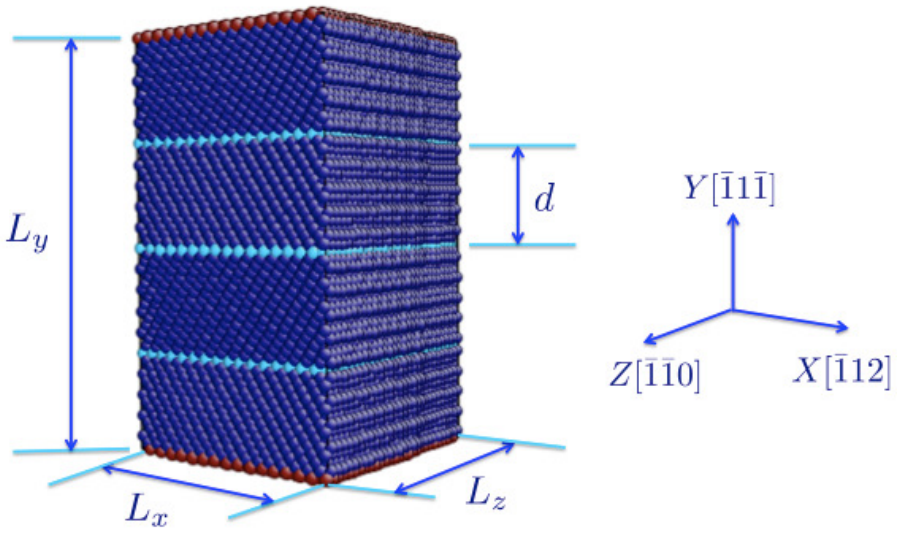


Figure 4.1: Atomistic structure of a nanotwinned specimen showing the crystallographic orientation. Equally spaced CTBs separated by distance $d$ are shown by cyan colored atoms [132].

the top and bottom surfaces. In order to isolate the contribution of the CTBs to the calculated stress, we need to subtract the contribution of the thermal stress resulting in a single crystal. To this end, a corresponding single crystal specimen with identical dimensions, orientation, and boundary conditions was created and equilibrated as above. We thereby obtain the contribution of the twin boundaries to the thermal stress as

$$\sigma = \sigma_{NT} - \sigma_{SC}, \tag{4.1}$$

where $\sigma_{NT}$ denotes the normal stress in the Y-direction calculated for the NT specimen and $\sigma_{SC}$ denotes the normal stress in the Y-direction calculated for the corresponding single crystal specimen without CTBs. To assess the effect of the simulation cell size on the stress calculations, we also performed the simulation on a larger specimen with dimensions $210\mathring{A} \times 250\mathring{A} \times 240\mathring{A}$. The results changed only negligibly.

## 4.3 Simulation Results

Figure 4.2 shows the variation of the stress $\sigma$ as a function of $1/d$, for specimen with different height $H$ at 800K. The relationship is linear and indicates that an increase in the CTB separation leads to a decrease in the thermal stress. For the different heights considered in our simulations, we also observe that for a fixed CTB spacing, the thermal stress $\sigma$ is independent of the height of the specimen, and hence the number of CTBs.

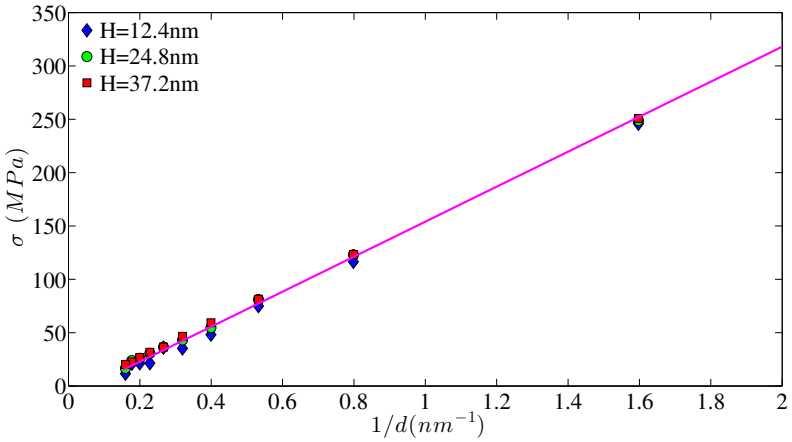


Figure 4.2: Variation of the stress ($\sigma$) with CTB density ($1/d$), for specimens with different height ($H$) at 800K. All cases show a linear relation [132].

We now consider simulations in which the number of CTBs, $N$, is held constant while the CTB spacing, $d$, is varied. For the sake of illustration, Figure 4.3 shows the atomistic structure of a typical specimen with three CTBs ($N = 3$) and different $d$. In these cases, $d$ is the CTB spacing and is also equal to the distance between the last CTBs and the adjoining top or bottom surfaces. Following the simulation procedure described above, we obtain the relationship between the thermal stress $\sigma$ and the TB density $1/d$. The results for specimens with different number of CTBs are compiled in Figure 4.4. All the cases exhibit a $1/d$ dependence of the thermal stress due to twin boundaries at finite temperature. We also note that as $N$ decreases, there is a decrease in the slope of the curves. This is

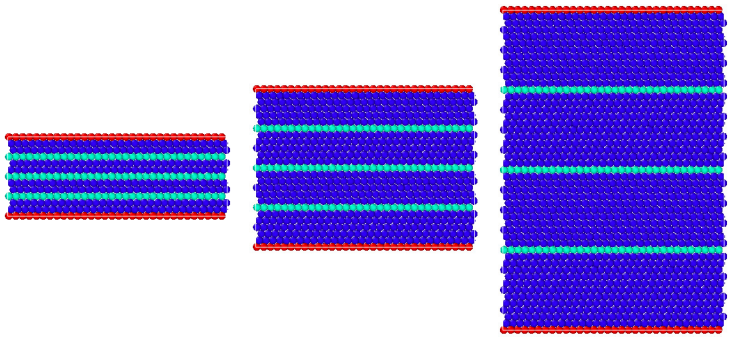

Figure 4.3: Atomistic structure of a typical specimen with a three CTBs ($N = 3$) and different $d$, and hence different heights. The red atoms indicate the fixed surfaces. The cyan atoms indicate the CTBs [88].

possibly a result of size effects in specimens with very few atomic layers, and will be discussed again in section 4.5. Nevertheless, taking together the simulation results shown in Figures 4.2 and 4.4, we observe that the linear dependence of the thermal stress on $1/d$ is rather insensitive to the number of CTBs or sample dimensions.

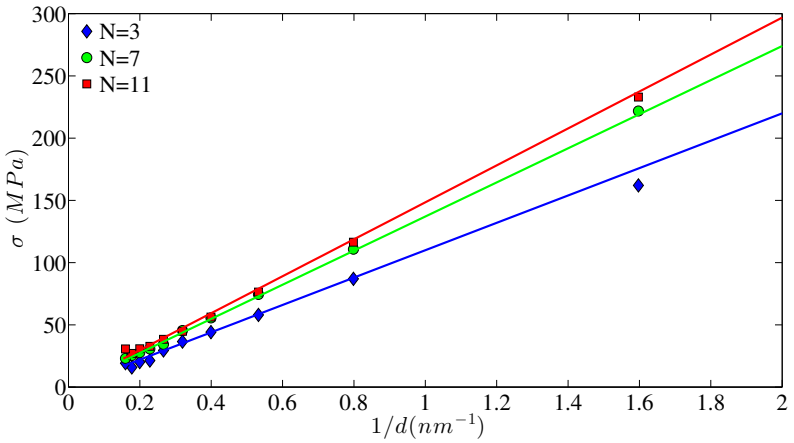


Figure 4.4: Variation of the stress $\sigma$ with CTB density, $1/d$, for specimen with different number of CTBs, $N$, at 800K. All cases show a linear dependence [132].

## 4.4 Analysis

Here we investigate the role of the thermal expansion to explain the $1/d$ dependence of the thermal stress observed in simulations. Past research has shown that the thermal expansion coefficient of nanostructured metals is indeed different from their single crystal counterparts and is strongly grain-size dependent [133, 134, 135, 136, 137]. This is due to the change in the coefficient of thermal expansion in the proximity of the grain boundaries owing to the mismatch in orientation. Following the work of Phillpot [133], we consider a periodic or infinitely long NT structure as comprising of two parts: the interfacial region around the CTB and the bulk region that is single crystalline. As shown in Figure 4.5), there is an interface region (hatched area) of width $\Lambda$ around each TB (shown by the dotted line in the middle). The hatched area on either ends is of width $\Lambda/2$ due to periodicity. The rest of the region is considered a perfect crystal. We assume that each of these regions has a distinct thermal expansion coefficient denoted by $\alpha_{TB}$, and $\alpha_{SC}$ respectively. It is reasonable to assume that $\alpha_{TB}$, and $\alpha_{SC}$ are material properties which means that they are independent of the CTB spacing $d$. Since the stress in the $Y$-direction (normal to the CTBs) is uniform, the effective thermal expansion coefficient $\alpha_{NT}$ for the nanotwinned structure can be calculated by adding the thermal expansion from the CTB region and the bulk region. Thus, we have

$$2d\,\alpha_{NT} = 2\,\Lambda\alpha_{TB} + (2d - 2\Lambda)\alpha_{SC}, \tag{4.2}$$

where $\Lambda$ is the thickness of the interfacial region. This can be reduced to

$$\alpha_{NT} - \alpha_{SC} = \Lambda(\alpha_{TB} - \alpha_{SC})\frac{1}{d}. \tag{4.3}$$

This is the difference between the thermal expansion coefficient of the NT structure and the single crystal structure. Assuming linear thermal expansion, linear elasticity yields the thermal stress as $\sigma = \alpha E \Delta T$, where $E$ is the Young's modulus.

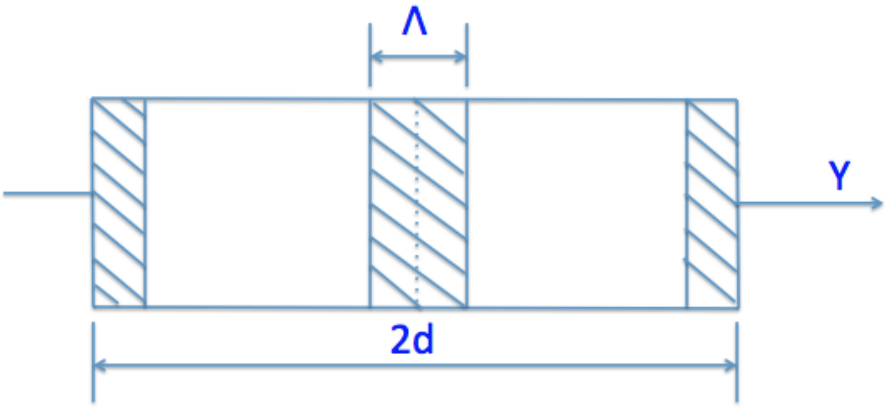


Figure 4.5: Schematic of a CTB superlattice of $2d$ length [132].

Thus, Equation 4.3 can be simplified as

$$\begin{aligned} \sigma &= \sigma_{NT} - \sigma_{SC} \\ &= \alpha_{NT}\Delta T E_{NT} - \alpha_{SC}\Delta T E_{SC} \\ &\approx \Lambda E_{SC}\Delta T(\alpha_{TB} - \alpha_{SC})\frac{1}{d} \propto \frac{1}{d}, \end{aligned} \tag{4.4}$$

which shows a linear dependence of the thermal stress on $1/d$, consistent with the atomistic simulations presented earlier. In the above derivation, it was assumed that $E_{NT} \approx E_{SC}$ which we have verified through molecular dynamics simulations. A series of simulations were performed on nanotwinned specimens shown in Figure 4.3 by replacing the fixed boundary conditions in the Y-direction with periodic boundary conditions in all directions. The specimens were first equilibrated at 800K under the NPT ensemble to relax the stresses and then subjected to uniaxial tension. The Young's modulus was obtained in each case as the slope of the stress-strain curve. For each CTB spacing, an identical simulation was performed on a corresponding single crystalline specimen. Figure 4.6 shows that the values of $E_{NT}$ and $E_{SC}$ converge for CTB spacing larger than 1 nm. Although some size effect is observed for spacings less than 1 nm, the difference is only about 4%, so our assumption that $E_{NT} \approx E_{SC}$ remains valid. We note that this analysis can be used to estimate the thermal stress due to any type of grain boundary. In-

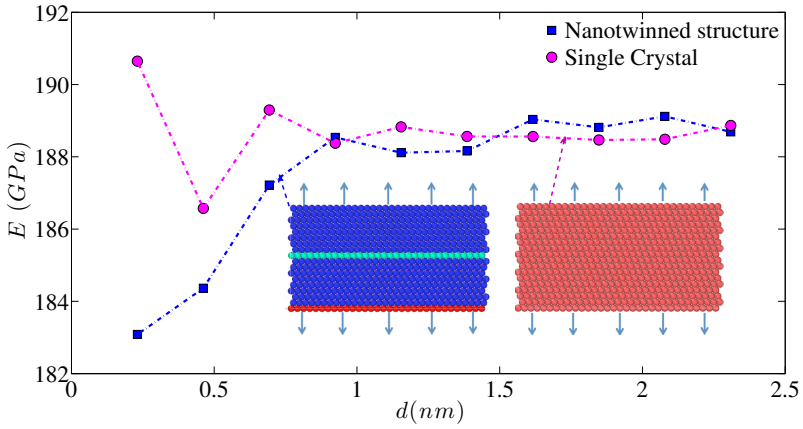


Figure 4.6: Variation of the Young's Modulus for single crystal ($E_{SL}$) and nanotwinned ($E_{NT}$) specimen with CTB spacing $d$ at 800K [132].

deed, previous studies have demonstrated that the thermal expansion coefficient of a general grain boundary follows a $1/d$ dependence on the grain size or grain boundary spacing [133, 137]. Thus, our study concludes that the thermal stress should exhibit a $1/d$ dependence for any interface and that it arises from the inhomogeneity in the coefficient of thermal expansion caused by the interfacial region around the CTB or GB.

## 4.5 Numerical Estimates

Based on the simulation results and the theoretical model discussed above, we now estimate the coefficient of thermal expansion for a CTB and compare it with available estimates for grain boundaries. To this end, let $m$ be the slope of the linear fit for $\sigma$ versus $1/d$. Then, using the expression for the slope based on Equation 4.4, we have

$$\Lambda(\alpha_{TB} - \alpha_{SC}) = \frac{m}{E_{SC}\Delta T}. \tag{4.5}$$

Since $\Lambda$ is not known, we estimate the value of the product of the $\Lambda$ parameter and the difference in the thermal expansion coefficients of the CTB and the single crystal. Normalizing the above expression with $\alpha_{SC}$ and the lattice constant, $a$, we

define $\eta$ as

$$\eta = \frac{\Lambda}{a}\left(\frac{\alpha_{TB}}{\alpha_{SC}} - 1\right) = \frac{m}{a\Delta T E_{SC}\alpha_{SC}}. \tag{4.6}$$

We use the following numerical values for Cu: $a = 3.615\mathring{A}$ (at 0 K), $E_{SC} = 189$ GPa (Figure 4.6), and $\alpha_{SC} = 16.934 \times 10^{-6}/K$ (obtained from simulations). Thus, calculating the slope, $m$, from Figure 4.2 and substituting in Equation 4.6, we get

$$\eta = \frac{\Lambda}{a}\left(\frac{\alpha_{TB}}{\alpha_{SC}} - 1\right) = 0.1772. \tag{4.7}$$

Similarly, calculating the slopes for the curves for different $N$ from Figure 4.4 and substituting in Equation 4.6, we get $\eta = 0.1112$ for $N = 3$, $\eta = 0.1386$ for $N = 7$, and $\eta = 0.1502$ for $N = 11$. Note that the values for $\eta$ approach that specified in Equation 4.7 as $N$ increases. To investigate this size effect in specimen with fewer atomic layers, let us consider a finite NT structure with $N$ CTBs in the interior similar to our simulation specimens which are non-periodic in the Y-direction. Since the structure is finite (non-periodic), it does not contain the interfacial regions of thickness $\Lambda/2$ on the ends of the specimen, unlike the structure in Figure 4.5 which is periodic. Then, Equation 4.2 is modified to

$$d(N+1)\alpha_{NT} = N\Lambda\alpha_{TB} + (N+1)(d-\Lambda)\alpha_{SC}, \tag{4.8}$$

which can be written as

$$\alpha_{NT} - \alpha_{SC} = \frac{\Lambda}{d}(\alpha_{TB} - \alpha_{SC}) - \frac{\Lambda\alpha_{TB}}{d(N+1)}. \tag{4.9}$$

Thus, for very large $N$, Equation 4.9 reduces to Equation 4.2. Revisiting the results of Figure 4.2, we see that for fixed $d$, as $N$ increases, the second term on the right hand side reduces and the curves eventually converge to that of Figure 4.2. Thus, the difference in the slopes in Figure 4.4 arises due to finite size effects in specimen with very few CTBs.

We finally calculate the thermal expansion coefficient for the CTB based on estimates for $\Lambda$ for different interfaces available in literature. A previous study

estimated the thickness of the interfacial region for a general grain boundary in nanocrystallline Cu and Au specimens to be about $2a - 3a$ [133]. Their atomistic simulations revealed that the thermal expansion coefficient of a twist grain boundary in Au is about 80% greater than that of a single crystal for the smallest grain boundary spacing considered. Experimental studies by Lu et al. [137] reported the interfacial thickness of grain boundaries in Ni-P alloys to be about 2 nm. Since CTB is a coherent, highly ordered interface, it is reasonable to assume that the interfacial thickness for a CTB would be much less than that of a grain boundary. Indeed, in our recent work [88] using molecular dynamics simulations and statistical mechanics based analysis of thermal fluctuations of CTBs, we show that the average thickness of a CTB is about $0.1 - 0.2\mathring{A}$. Using $\Lambda = 0.1\mathring{A}$ in Equation 4.7, we obtain

$$\alpha_{TB} = 7.4\alpha_{SC}. \tag{4.10}$$

This is consistent with the range for the thermal expansion coefficient of grain boundaries reported by Lu et al. [137] between 1.2 to 12 times that of a single crystal.

## 4.6 Concluding Remarks

In summary, we present molecular dynamics simulations to estimate the thermal stress due to the presence of parallel coherent twin boundaries at finite temperature. Our simulations reveal that for all twin boundary spacings, $d$, the stress decays as $1/d$. We present a simple analytical model to show that the $1/d$ dependence stems from the thermal stress in nanostructured materials due to the inhomogeneity in the thermal expansion coefficient of the matrix and the interfacial regions. It is also interesting to note that twin boundaries separated by a mere distance of about 6 $\mathring{A}$ lead to a thermal expansion induced stress of about

250 MPa which is surprisingly large. This possibly results from the large coefficient of thermal expansion of a CTB which is more than seven times greater than that of a single crystal. However, we note that these results are obtained for NT specimens when the thermal stress is not relaxed. If the thermal stress is relaxed completely, there will be no stress measured from simulations. The environment experienced by twin boundaries in real NT materials should be somewhere in between the two cases. This is because of residual thermal stress within the grains in a typical NC structure resulting from the different thermal expansion of neighboring grains and the grain boundary regions separating them [133]. Thus, the present work provides an upper bound to the thermal expansion induced stress in the presence of twin boundaries and other crystalline interfaces. We finally note that although our simulations and analysis should hold for grain boundaries in general, our study focuses on twin boundaries owing to the fabrication of NT structures consisting of parallel twin boundaries with separation distances ranging from a few nanometers to a few angstroms.

# Chapter 5 Mobility of Defective Grain Boundaries

## 5.1 Introduction

Manipulating the material microstructure for desired properties has well been explored over the past decades [23, 138, 139, 140, 141, 142]. In particular, the average grain size of polycrystalline materials plays a vital role in determining the mechanical properties due to the classic Hall-Petch relationship [25]. In view of this, investigating the microstructure evolution, espicially in the presence of defects, becomes a critical issue. In polycrystalline materials, it is the grain boundary (GB) motion including sliding, rotation and migration that controls the microstructural evolution and sets the final configuration.

The key property responsible for GB motion is mobility $M$, which is the proportionality coefficient between exerted pressure $F$ and the migration velocity $v$

$$v = MF. \tag{5.1}$$

Mobility M is generally considered as the intrinsic property of GB and follows the Arrhenius equation

$$M = M_0 exp(-\frac{Q_m}{k_B T}), \tag{5.2}$$

where $M_0$ is the preexponential constant, $Q_m$ is the activation energy for GB migration, $k_B$ is the Boltzmann constant, $T$ is temperature. Due to its core role in GB growth, a great majority of experimental measurements of GB mobility were carried out based on bicrystals and polycrystals over the past decades to study its dependence on five macroscopic degrees of freedom associated with the GB

structure, including misorientation and inclination, on the temperature and the effect of external force [143, 144, 145, 146, 147, 148].

With the rapid developments in high performance computing, atomistic simulations, such as molecular dynamics (MD) simulations, are being increasingly used to investigate the GB mobility. Compared with experiments, there are many more parameters that can be controlled and the simulation cell can be free of impurities as well. In general, there are two main classes of MD simulation approaches aimed at understanding GB migration and mobility. One is the "driving force" method, in which the driving force is applied to move the GB migration. This "driving force" can be a real force such as applied elastic strain [64] and interface curvature restoring force [65, 66]; or can be somewhat artificial energy difference between different grains [67]. The other class of method to capture the mobility is related to GB "thermal fluctuations", either the boundary profile [68] or average position [74]. The former method has some limitation so that it can not be applied to GBs having a cusp in the plot of the energy versus misorientation or at low temperature. The latter, which was motivated by the classic random walk model, has more general application in temperature range $0.2T_m$ to $0.88T_m$ ($T_m$ is melting temperature), especially after adapted by Deng and Schuh [75, 76] for low temperature. Mendelev et al. [149] compared these two classes of MD simulation methods and reached the conclusion that both methods lead to the same values of GB mobility provided that the drive force is low enough.

However, the mobility obtained from either simulation methods is one or two orders of magnitude larger than that measured from experiments; meanwhile the activation energy for GB migration during simulation is smaller by a factor of 2-3 than that obtained from experiments. This obvious discrepancy between simulation and experiment can be attributed to the presence of impurities in experimental samples [150, 151]. Thus, it is necessary to investigate the drag

effect of impurities on GB mobility. In fact, there are only a few studies that have been done in this area, either in theory [152, 153, 154, 155, 156, 157, 158] or in simulation [159, 160]. Qualitatively, the presence of impurities impedes the GB migration and decreases the GB mobility. Also, the more the concentration of impurities, the smaller is the GB mobility.. Nevertheless, there are few quantitative studies on the impact of impurity properties, such as concentration, size and other factors like temperature. The reason is that the effect of impurities on grain boundary migration can be very complex, not only depending on the type of impurities, such as vacancy, interstitials, second phase particles and so on, but also relying on the form of the microscopic interaction between impurities and GB. In order to circumvent these obstacles, we try to start with the simplest case. To be specific, we implement the interface random walk model to study the GB mobility with fixed second phase particles. On one hand, as mentioned before, the interface random walk model is verified as a simply and efficient simulation method. It also does not need any external driving force which avoid disturbing the original structure as much as possible. On the other hand, the second phase particles are fixed in our simulations to avoid their diffusion effect on GB migration.

The rest of the Chapter is organized as follows. Section 5.2 provides a review of the random walk model applied to calculate the GB mobility. In Section 5.3 we extend it to account for the presence of impurities, such as second phase particles. We re-derive the GB diffusion equation in time domain and frequency domain , and proposed a simple and efficient calculation approach to obtain the modified GB mobility. Section 5.4 presents our molecular dynamics simulation result which support our theoretical model and discusses about the particles drag effect dependence on concentration, size and temperatures. The summary and potential ramifications of these findings are discussed in Section 5.5.

## 5.2 Brief Review of Random Walk Model

### 5.2.1 Interface Random Walk Model

Trautt et al. [74] presented an approach in which interface Mobility $M$ can be extracted from its random walk by means of MD simulations. Average migration of grain boundary can be considered as 1-D Brownian motion due to the thermal noise (Figure 5.1). Based on this assumption, the GB mobility $M$ can be determined by the 'diffusion coefficient' $D$ which can be easily captured from the classical Einstein diffusion equation.

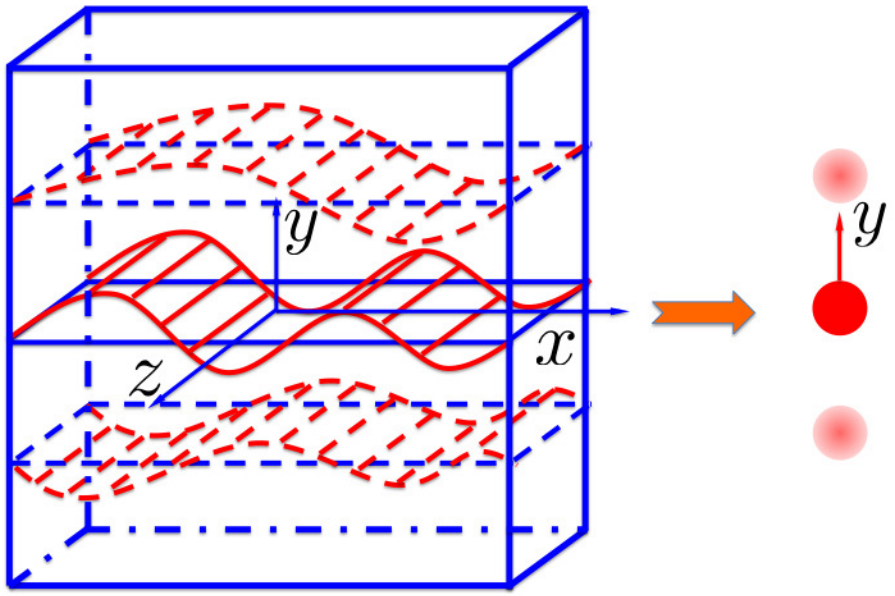


Figure 5.1: Migration of quasi-one dimensional grain boundary can be considered as Brownian particle moving in Y direction.

To understand how GB mobility $M$ is connected to the 'diffusion coefficient' $D$, imagine a 2-D GB fully periodic in $X$ and $Z$ directions. At finite temperature, its height profile $h(\mathbf{r}, t)$ is shown in Figure 5.2.

Starting from the classic GB migration equation

$$v(\mathbf{r}, t) = MF(\mathbf{r}, t), \tag{5.3}$$

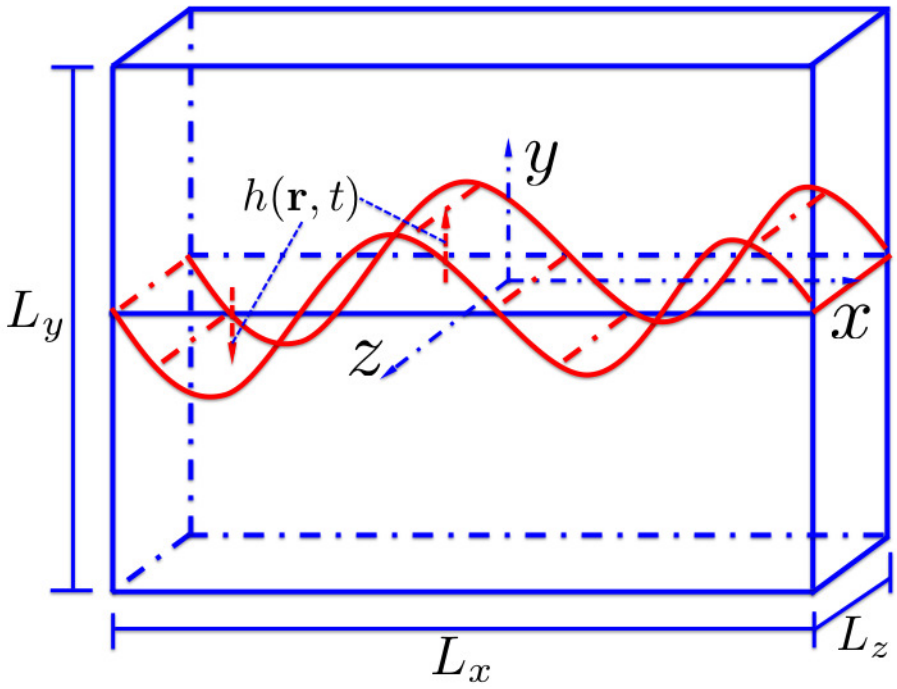


Figure 5.2: Quasi-one dimensional grain boundary.

where $v(\mathbf{r},t)$ is the velocity, $F(\mathbf{r},t)$ is the force acting on GB which includes noise force $\xi(\mathbf{r},t)$ and curvature restoring force $f_c(\mathbf{r},t)$. According to the similarity between GB and Brownian particle, the thermal noise force $\xi(\mathbf{r},t)$ can be assumed to satisfy this condition

$$< \xi(\mathbf{r},t)\xi(\mathbf{r}^{'},t^{'}) >= \frac{2k_BT}{M}\delta(\mathbf{r}-\mathbf{r}^{'})(t-t^{'}). \tag{5.4}$$

Under the small slope approximation $h_x \ll 1, h_y \ll 1$, the curvature restoring force $f_c$ is

$$f_c(\mathbf{r},t) = \Gamma(h_{xx}+h_{yy}), \tag{5.5}$$

where the $\Gamma$ is the GB stiffness. Then the Equation 5.3 can be converted into

$$\frac{\partial h(\mathbf{r},t)}{\partial t} = M[\Gamma(h_{xx}+h_{zz})+\xi(\mathbf{r},t)]. \tag{5.6}$$

Introducing the spatial average of GB migration

$$\bar{h}(\mathbf{r},t) = \frac{1}{S}\int_0^{L_x}\int_0^{L_Z} h(\mathbf{r},t)dxdz, \tag{5.7}$$

where $S = L_x L_z$ is the GB area. Similarly, the spatial average of GB migration velocity is

$$\overline{\frac{\partial h(\mathbf{r},t)}{\partial t}} = \frac{1}{S}\int_0^{L_x}\int_0^{L_Z} M[\Gamma(h_{xx}+h_{zz})+\xi(\mathbf{r},t)]dxdz. \tag{5.8}$$

Due to the periodic boundary conditions in $X$ and $Z$ directions, the spatial integral of curvature restoring force vanishes, that is

$$\begin{aligned}
&\frac{1}{S}\int_0^{L_x}\int_0^{L_z} M[\Gamma(h_{xx}+h_{zz})]dxdz \\
&= \frac{M\Gamma}{S}[\int_0^{L_z}\int_0^{L_x} h_{xx}dxdz + \int_0^{L_x}\int_0^{L_z} h_{zz}dxdz] \\
&= \frac{M\Gamma}{S}[\int_0^{L_z} h_x|_0^{L_x}dz + \int_0^{L_x} h_z|_0^{L_z}dx]. \\
&= 0.
\end{aligned} \tag{5.9}$$

Thus,

$$\begin{aligned}
&\overline{\frac{\partial h(\mathbf{r},t)}{\partial t}} = \frac{1}{S}\int_0^{L_x}\int_0^{L_Z}\xi(\mathbf{r},t)dxdz \\
&\Rightarrow \frac{\partial \overline{h}(\mathbf{r},t)}{\partial t} = M\overline{\xi}(\mathbf{r},t),
\end{aligned} \tag{5.10}$$

where $\overline{\xi}(\mathbf{r},t) = \frac{1}{S}\int_0^{L_x}\int_0^{L_Z}\xi(\mathbf{r},t)dxdz$ denotes its corresponding spatial average value.

Solving the Equation 5.10 in time domain,

$$\overline{h}(\mathbf{r},t) = M\int_0^t \overline{\xi}(\mathbf{r},\tau)d\tau. \tag{5.11}$$

The variance of average migration can be expressed as

$$
\begin{aligned}
&< \overline{h}^2(\mathbf{r},t) > \\
&=< M\int_0^t \overline{\xi}(\mathbf{r_1},\tau_1)d\tau_1 \times M\int_0^t \overline{\xi}(\mathbf{r_2},\tau_2)d\tau_2 > \\
&= M^2\int_0^t\int_0^t < \overline{\xi}(\mathbf{r_1},\tau_1)\overline{\xi}(\mathbf{r_2},\tau_2) > d\tau_1 d\tau_2 \\
&= M^2\int_0^t\int_0^t < \frac{1}{S}\int_0^{L_x}\int_0^{L_z}\xi(\mathbf{r_1},\tau_1)dx_1dz_1 \times \frac{1}{S}\int_0^{L_x}\int_0^{L_z}\xi(\mathbf{r_2},\tau_2)dx_2dz_2 > d\tau_1 d\tau_2 \\
&= \frac{M^2}{S^2}\int_0^t d\tau_1\int_0^t d\tau_2\int_0^{L_x}\int_0^{L_z}\int_0^{L_x}\int_0^{L_z} < \xi(\mathbf{r_1},\tau_1)\xi(\mathbf{r_2},\tau_2) > dx_1dz_1dx_2dz_2 \\
&= \frac{M^2}{S^2}\int_0^t d\tau_1\int_0^t d\tau_2\int_0^{L_x}\int_0^{L_z}\int_0^{L_x}\int_0^{L_z} < \xi(\mathbf{r_1},\tau_1)\xi(\mathbf{r_2},\tau_2) > dx_1dz_1dx_2dz_2.
\end{aligned}
\tag{5.12}
$$

Substituting the Equation 5.4, then

$$
\begin{aligned}
&< \overline{h}^2(\mathbf{r},t) > \\
&= \frac{M^2}{S^2}\int_0^t d\tau_1\int_0^t d\tau_2\int_0^{L_x}\int_0^{L_z}\int_0^{L_x}\int_0^{L_z}\frac{2k_BT}{M}\delta(\mathbf{r_1}-\mathbf{r_2})(\tau_1-\tau_2)dx_1dz_1dx_2dz_2 \\
&= \frac{2Mk_BT}{S^2}\int_0^t d\tau_1\int_0^t d\tau_2\int_0^{L_x}\int_0^{L_z}\int_0^{L_x}\int_0^{L_Z}\delta(\mathbf{r_1}-\mathbf{r_2})(\tau_1-\tau_2)dx_1dz_1dx_2dz_2 \\
&= \frac{2Mk_BT}{S^2}\int_0^t d\tau_1\int_0^{L_x}\int_0^{L_z}dx_1dz_1 \\
&= \frac{2Mk_BT}{S}t.
\end{aligned}
\tag{5.13}
$$

Thus the GB diffusion equation is

$$
< \overline{h}^2(t) >= \frac{2Mk_BT}{S}t, \tag{5.14}
$$

where $< \overline{h}^2(\mathbf{r},t) >$ is denoted by $< \overline{h}^2(t) >$, which can be easily extracted from atomistic simulations. Then GB mobility $M$ can be determined from the slope of the fitting curve according to Equation 5.14, as shown in Figure 5.3.

### 5.2.2 Adapted Interface Random Walk Model

Interface random walk approach can only be used at very high temperature, usually at $0.8Tm$, which greatly restricts its application. Deng and Schuh

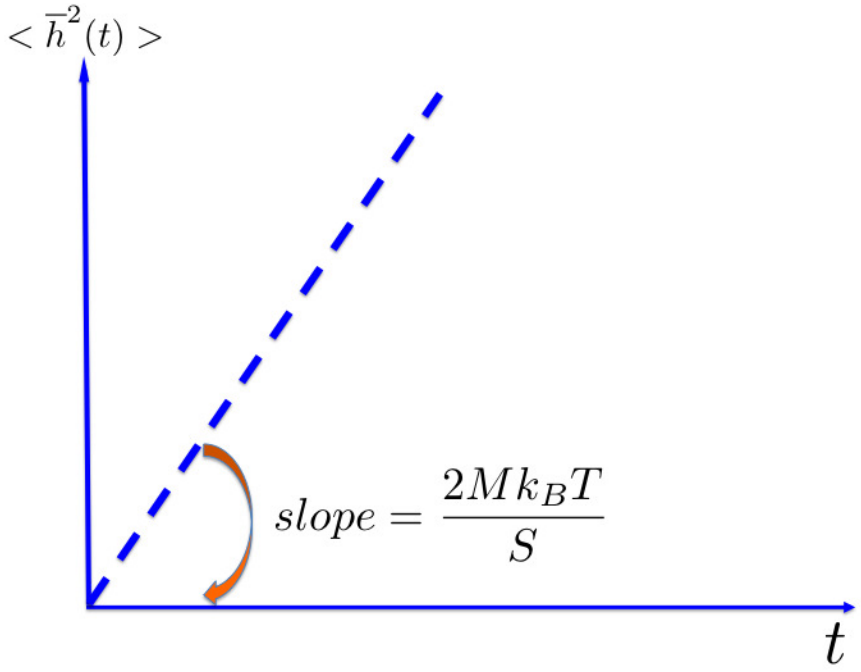


Figure 5.3: Schematic of the temporal evolution of the variance $< \overline{h}^2(t) >$.

[75] made an adaptation and presented the ingenious post processing approach, which effectively increased the accuracy and extended application to very low temperature, up to $0.2T_m$. Assuming there are $N$ simulation samples, each sample has $n$ time intervals, then we will have a matrix $\overline{H}$ which records GB average migration positions

$$\begin{pmatrix} \overline{h}_1(1) & \overline{h}_2(1) & \dots & \overline{h}_N(1) \\ \overline{h}_1(2) & \overline{h}_2(2) & \dots & \overline{h}_N(2) \\ \dots & \dots & \dots & \dots \\ \overline{h}_1(n) & \overline{h}_2(n) & \dots & \overline{h}_N(n) \end{pmatrix}$$

, where $\overline{h}_j(k)$ represents the average migration at $k$th time interval for simulation sample $j$, $k = 1, 2, 3, \dots, n$ and $j = 1, 2, 3, \dots, N$.

The most remarkable feature of Equation 5.14 is that mobility $M$ appears in the slope term $\frac{2Mk_BT}{S}$. Thus, the key of increasing the curve fitting precision depends on the number of simulation samples not on the length of each sample.

Following the postprocessing technique of Deng and Schuh [75], we introduce the GB displacement $\overline{d}(i)$ from an arbitrary position at $t = k\Delta t$ for each sample, as show in Figure 5.4, so that

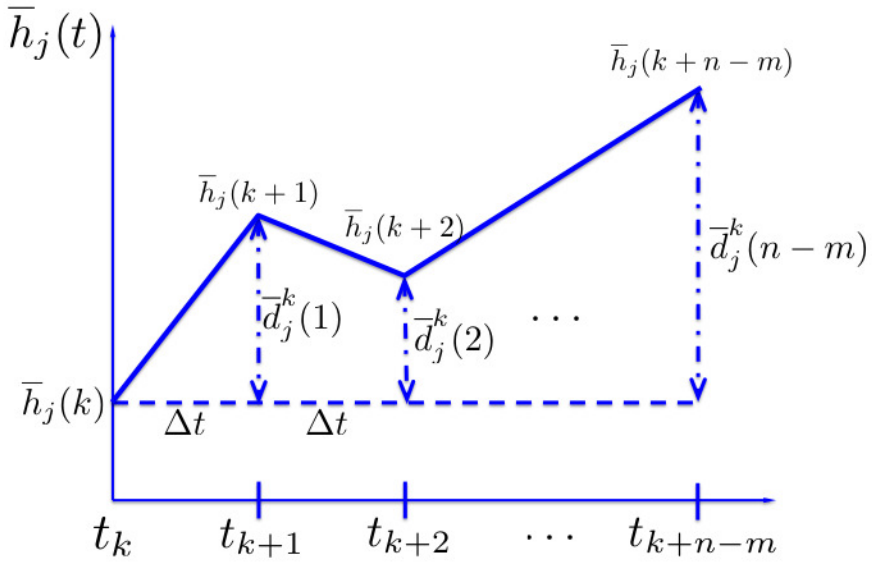


Figure 5.4: Schematic showing the definition of GB displacement $\overline{d}(i)$ relative to average GB migration position $\overline{h}(i)$.

$$\begin{aligned} &\overline{d}_j^k(i) = \overline{h}_j(k+i) - \overline{h}_j(k) \\ &j = 1,2,\ldots,N; k = 1,2,\ldots,m; i = 1,2,\ldots,n-m; m \leq n, \end{aligned} \tag{5.15}$$

thus similarly

$$D = \frac{d < \overline{d}^2 >}{dt} \sim \frac{2Mk_BT}{S}. \tag{5.16}$$

By means of this definition, we inflate the sample quantity from $N$ to $m \times N$, which effectively increases the curve fitting accuracy and reduces the measurement of noise accordingly.

## 5.3 Interface Random Walk with Second Phase Particles

### 5.3.1 Interaction between GB and Second Phase Particles

Since current random walk model is only restricted to free GB, we extend it to account for the presence of impurities, such as second phase particles. In order to study the drag impact, we consider the interaction between particles and GB motivated by the classic Zener pinning model [161, 162]. In Figure 5.5b, the solid line represents the initial spatial average of GB, dashed line corresponds to its final position. The energy decrease of GB with respect to the initial position stems from the decrease of area, as shown in Figure 5.5b.

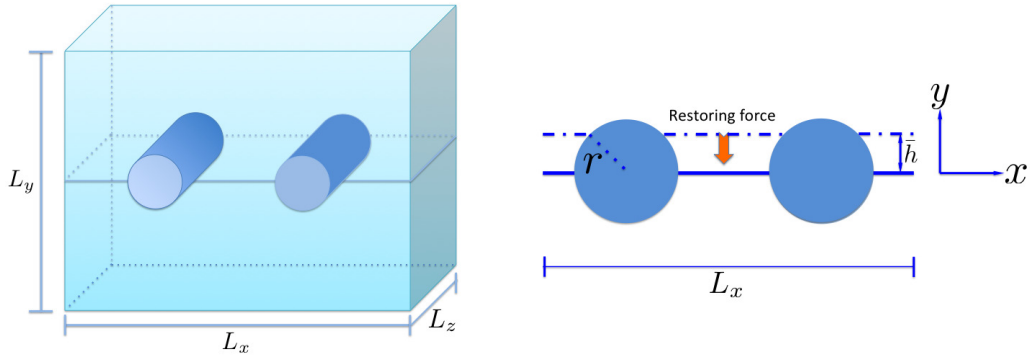


Figure 5.5: Schematic diagram of grain boundary with second phase cylinder particles

$$
\begin{aligned}
\Delta E(\bar{h}) &= E(\bar{h}) - E(0) \\
&= \gamma_s(S - 2NL_z\sqrt{r^2 - \bar{h}^2}) - \gamma_s(S - 2NL_zR) \\
&= 2N\gamma_s L_z[r - \sqrt{r^2 - \bar{h}^2}] \\
&= 2N\gamma_s L_z r[1 - \sqrt{1 - (\frac{\bar{h}}{r})^2}] \\
&\approx 2N\gamma_s L_z r \times \frac{1}{2}(\frac{\bar{h}}{r})^2 \\
&= \frac{N\gamma_s L_z}{r}\bar{h}^2,
\end{aligned}
\tag{5.17}
$$

where, $N$ is the number of second phase particles, $\gamma_s$ is the surface tension energy of GB. Notice that the interaction energy between GB and second phase particle has a quadratic dependance on average GB migration displacement $\bar{h}$. Thus, similar to the spring-mass system, there exists a restoring force

$$
f_r = -\frac{\partial \Delta E}{\partial \bar{h}} = -\frac{2N\gamma_s L_z}{r}\bar{h}. \tag{5.18}
$$

For convenience, we define a new variable $k_s = \frac{2N\gamma_s}{rL_x}$ as the drag coefficient between GB and second phase particles. Then the drag pressure is given by

$$
\frac{f_r}{S} = -k_s\bar{h}. \tag{5.19}
$$

### 5.3.2 Modified Diffusion Equation

Considering the drag effect term of second phase particles, the GB diffusion equation Equation 5.10 can be modified as

$$
\frac{d\overline{h}(t)}{dt} = M[\overline{\xi}(t) - k_s\bar{h}(t)], \tag{5.20}
$$

where $\overline{\xi}(\mathbf{r}, t)$ is denoted by $\overline{\xi}(t)$. Solving the Equation 5.20 in time domain with initial condition $\overline{h}(0) = 0$,

$$
\begin{aligned}
\overline{h}(t) &= \overline{h}(0)e^{-Mk_s t} + M\int_0^t \overline{\xi}(\tau)e^{-Mk_s(t-\tau)}d\tau \\
&= M\int_0^t \overline{\xi}(\tau)e^{-Mk_s(t-\tau)}d\tau.
\end{aligned}
\tag{5.21}
$$

It is easy to obtain that

$$
\begin{aligned}
<\overline{\xi}(t)\overline{\xi}(t+\tau)> &=< \frac{1}{S}\int_0^{L_x}\int_0^{L_z}\xi(\mathbf{r_1},t)dx_1dz_1 \times \frac{1}{S}\int_0^{L_x}\int_0^{L_z}\xi(\mathbf{r_2},t+\tau)dx_2dz_2 > \\
&= \frac{1}{S^2}\int_0^{L_x}\int_0^{L_z}\int_0^{L_x}\int_0^{L_z} <\xi(\mathbf{r_1},t)\xi(\mathbf{r_2},t+\tau)> dx_1dz_1dx_2dz_2 \\
&= \frac{1}{S^2}\int_0^{L_x}\int_0^{L_z}\int_0^{L_x}\int_0^{L_z} <\xi(\mathbf{r_1},t)\xi(\mathbf{r_2},t+\tau)> dx_1dz_1dx_2dz_2 \\
&= \frac{1}{S^2}\int_0^{L_x}\int_0^{L_z}\int_0^{L_x}\int_0^{L_z} \frac{2k_BT}{M}\delta(\mathbf{r_1}-\mathbf{r_2})\delta(\tau)dx_1dz_1dx_2dz_2 \\
&= \frac{2k_BT}{MS^2}\int_0^{L_x}\int_0^{L_z}\delta(\tau)dx_1dz_1 \\
&= \frac{2k_BT}{MS}\delta(\tau).
\end{aligned}
\tag{5.22}
$$

Thus the variance of average migration is

$$
\begin{aligned}
<\overline{h}^2(t)> &=< M\int_0^t \overline{\xi}(\tau_1)e^{-Mk_s(t-\tau_1)}d\tau_1 \times M\int_0^t \overline{\xi}(\tau_2)e^{-Mk_s(t-\tau_2)}d\tau_2 > \\
&= M^2\int_0^t\int_0^t <\overline{\xi}(\tau_1)\overline{\xi}(\tau_2)> e^{-Mk_s(2t-\tau_1-\tau_2)}d\tau_1d\tau_2 \\
&= M^2\int_0^t\int_0^t \frac{2k_BT}{MA}\delta(\tau_1-\tau_2)e^{-Mk_s(2t-\tau_1-\tau_2)}d\tau_1d\tau_2 \\
&= \frac{2Mk_BT}{S}\int_0^t\int_0^t \delta(\tau_1-\tau_2)e^{-Mk_s(2t-\tau_1-\tau_2)}d\tau_1d\tau_2 \\
&= \frac{2Mk_BT}{S}\int_0^t e^{-2Mk_s(t-\tau)}d\tau \\
&= \frac{2Mk_BT}{S}\frac{e^{-2Mk_s(\tau-t)}}{2Mk_s}\ |_0^t \\
&= \frac{k_BT}{Sk_s}[1-e^{2Mk_st}].
\end{aligned}
\tag{5.23}
$$

Thus the modified diffusion equation of GB is

$$
\begin{aligned}
<\overline{h}^2(t)> &= \frac{k_BT}{Sk_s}(1-e^{-2Mk_st}) \\
&= \begin{cases} \frac{2Mk_BT}{S}t & \text{if } t \ll \frac{1}{Mk_s} \\ \frac{k_BT}{Sk_s} & \text{if } t \gg \frac{1}{Mk_s}. \end{cases}
\end{aligned}
\tag{5.24}
$$

Similarly, both the modified GB mobility $M$ and the drag coefficient $k_s$ can be extracted from the temporal evolution curve of $<\overline{h}^2(t)>$, as shown in Figure 5.6.

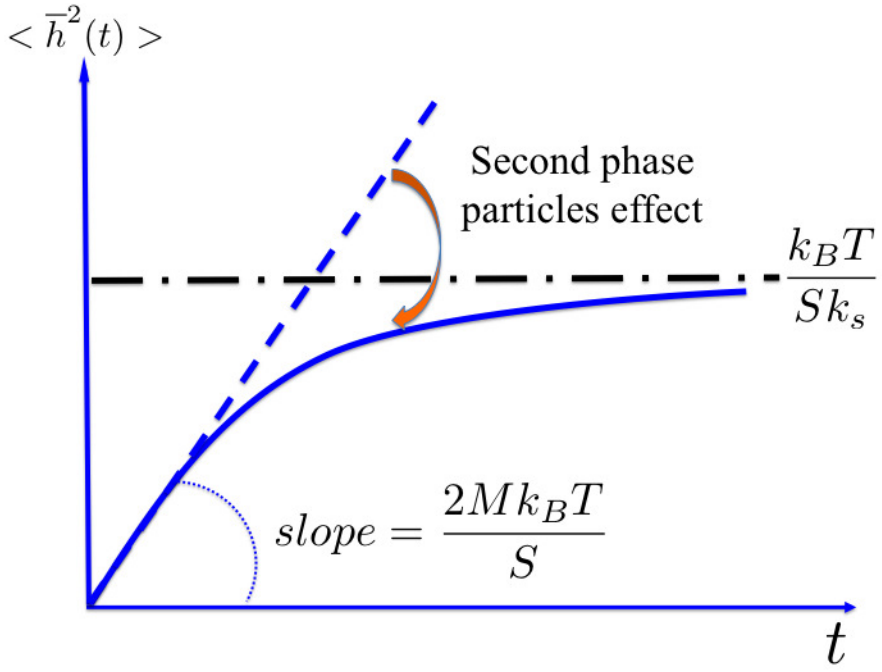


Figure 5.6: Schematic diagram of drag effect of second phase particles on the GB mobility in time domain.

### 5.3.3 Migration Power Spectrum Method

Motivated by the post processing approach of Deng and Schuh [75, 76], we propose a new calculation method in the frequency domain to get the mobility $M$ and drag coefficient $k_s$. Deng and Schuh [75, 76] method's efficiency lies in the huge increase of sample number without performing more simulations. In essence, it is achieved through considering the ensemble average of GB migration correlation function with the same time intervals. In fact, there is a more nature way to introduce the GB migration correlation function and migration power spectrum, and then deal with the GB diffusion in Fourier space.

To this end, we introduce two pairs of Fourier transforms

$$\begin{aligned} \bar{h}(t) &= \int_{-\infty}^{+\infty} \tilde{h}(f) e^{2\pi i f t} df \\ \tilde{h}(f) &= \int_{-\infty}^{+\infty} \bar{h}(t) e^{-2\pi i f t} dt \; and \end{aligned} \tag{5.25}$$

$$\begin{aligned}\overline{\xi}(t) &= \int_{-\infty}^{+\infty} \tilde{\overline{\xi}}(f) e^{2\pi i f t} df \\ \tilde{\overline{\xi}}(f) &= \int_{-\infty}^{+\infty} \overline{\xi}(t) e^{-2\pi i f t} dt.\end{aligned} \tag{5.26}$$

Then in the Fourier space, the modified GB diffusion equation Equation 5.20 becomes

$$(2\pi i f + M k_s)\tilde{h}(f) = M\tilde{\overline{\xi}}(f). \tag{5.27}$$

Now we introduce the Migration Power Spectrum function

$$\begin{aligned}S_{hh}(f) &= \lim_{P\to\infty} \frac{1}{P}|\tilde{h}_P(f)|^2 \\ S_{\overline{\xi}\overline{\xi}}(f) &= \lim_{P\to\infty} \frac{1}{P}|\tilde{\overline{\xi}}_P(f)|^2.\end{aligned} \tag{5.28}$$

Then the Equation 5.26 can be converted to

$$S_{hh}(f) = \frac{M^2}{4\pi^2 f^2 + M^2 k_s^2} S_{\overline{\xi}\overline{\xi}}(f). \tag{5.29}$$

According to the classic Wiener-Khintchine theorem: the power spectrum function and correlation function is a Fourier pair, that is to say

$$\begin{aligned}S_{hh}(f) &= \int_{-\infty}^{+\infty} R_{hh}(\tau) e^{-2\pi i f \tau} d\tau \\ S_{\overline{\xi}\overline{\xi}}(f) &= \int_{-\infty}^{+\infty} R_{\overline{\xi}\overline{\xi}}(\tau) e^{-2\pi i f \tau} d\tau,\end{aligned} \tag{5.30}$$

where the correlation functions are defined as

$$\begin{aligned}R_{hh}(\tau) &= \lim_{Q\to\infty} \frac{1}{Q} \int_{-Q/2}^{Q/2} < \overline{h}(t)\overline{h}(t+\tau) > dt \\ R_{\overline{\xi}\overline{\xi}}(\tau) &= \lim_{Q\to\infty} \frac{1}{Q} \int_{-Q/2}^{Q/2} < \overline{\xi}(t)\overline{\xi}(t+\tau) > dt.\end{aligned} \tag{5.31}$$

Then the correlation function of noise force is

$$\begin{aligned}R_{\overline{\xi}\overline{\xi}}(\tau) &= \lim_{Q\to\infty} \frac{1}{Q} \int_{-Q/2}^{Q/2} < \overline{\xi}(t)\overline{\xi}(t+\tau) > dt \\ &= \lim_{Q\to\infty} \frac{1}{Q} \int_{-Q/2}^{Q/2} \frac{2k_B T}{MS}\delta(\tau) dt \\ &= \frac{2k_B T}{MS}\delta(\tau).\end{aligned} \tag{5.32}$$

Substituting Equation 5.32 into Equation 5.30, then

$$\begin{aligned} S_{\xi\xi}(f) &= \int_{-\infty}^{+\infty} R_{\xi\xi}(\tau) e^{-2\pi i f \tau} d\tau \\ &= \int_{-\infty}^{+\infty} \frac{2k_B T}{MS} \delta(\tau) e^{-2\pi i f \tau} d\tau \\ &= \frac{2k_B T}{MS}. \end{aligned} \tag{5.33}$$

Substituting Equation 5.33 into Equation 5.29, we can get the Migration Power Spectrum with drag coefficient $k_s$

$$S_{hh}(f) = \frac{2Mk_B T}{4\pi^2 S f^2 + M^2 k_s^2 S}. \tag{5.34}$$

Without any drag effect ($k_s = 0$), then

$$S_{hh}(f) = \frac{Mk_B T}{2\pi^2 S f^2}. \tag{5.35}$$

Now it is easier to obtain the mobility $M$ and drag coefficient $k_s$ from curve fitting, as shown in Figure 5.7.

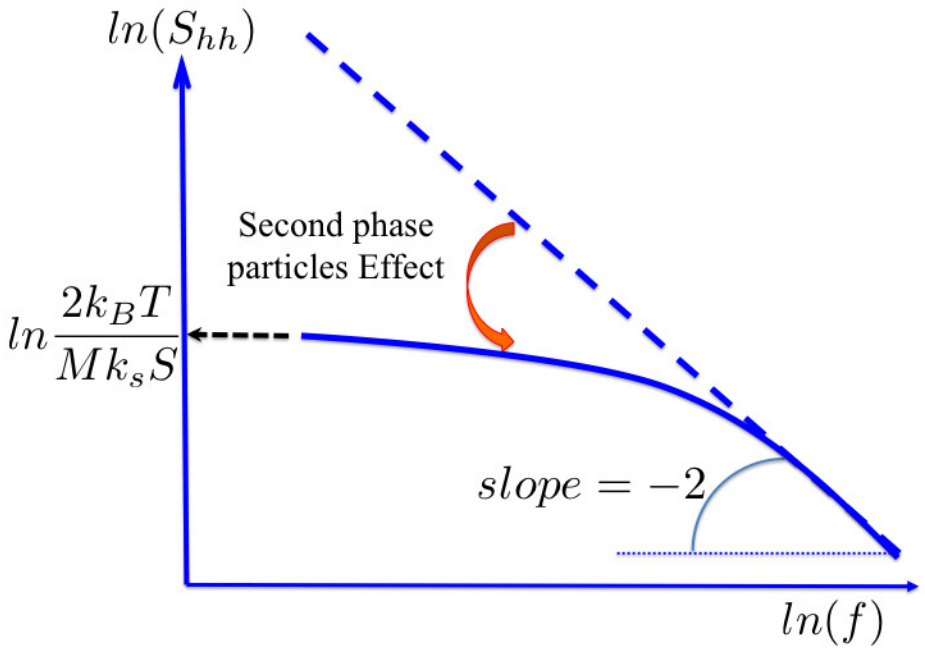


Figure 5.7: Schematic diagram of second phase particles effect on GB motion in frequency domain.

To be specific, for high frequency region:

$$\begin{aligned} & 4\pi^2 S f^2 \gg M^2 k_s^2 S \\ & \Rightarrow f \gg \frac{M k_s}{2\pi} \\ & \Rightarrow S_{hh}(f) = \frac{M k_B T}{2\pi^2 S} \bullet \frac{1}{f^2}. \end{aligned} \tag{5.36}$$

During the simulation, $C_f = \frac{M k_B T}{2\pi^2 S}$ can be obtained from curve fitting for larger $f$, then

$$M = C_f \bullet \frac{2\pi^2 S}{k_B T}. \tag{5.37}$$

For low frequency region:

$$\begin{aligned} & 4\pi^2 S f^2 \ll M^2 \equiv f \ll \frac{M k_s}{2\pi} \\ & \Rightarrow S_{hh}(0) = \frac{2 M k_B T}{M^2 k_s^2 S} = \frac{2 k_B T}{M k_s^2 S} \\ & \Rightarrow k_s^2 = \frac{2 k_B T}{MS \times S_{hh}(0)} \\ & \Rightarrow k_s = \sqrt{\frac{2 k_B T}{MS \times S_{hh}(0)}}. \end{aligned} \tag{5.38}$$

### 5.3.4 Calculation Details for Migration Power Spectrum

According to the Equation 5.34, $S_{hh}$ plays an important role throughout the whole calculation. As we have discussed in section 5.3.3, there are two steps to obtain it.

(1) Step 1: $R_{hh}(\tau) = \lim_{Q \to \infty} \frac{1}{Q} \int_{-Q/2}^{Q/2} < \overline{h}(t) \overline{h}(t+\tau) > dt$

We start from the same matrix $H$ but in the different angle of view

$$\begin{pmatrix} \overline{h}_1(1) & \overline{h}_2(1) & \dots & \overline{h}_N(1) \\ \overline{h}_1(2) & \overline{h}_2(2) & \dots & \overline{h}_N(2) \\ \dots & \dots & \dots & \dots \\ \overline{h}_1(n) & \overline{h}_2(n) & \dots & \overline{h}_N(n) \end{pmatrix}$$

$$
\begin{aligned}
R_{hh}(0) &= R_{hh}(0 \times \Delta t) = \frac{1}{n}\sum_{j=1}^{n}[\frac{1}{N}\sum_{i=1}^{N}\overline{h}_i(j)\overline{h}_i(j)] \\
R_{hh}(1) &= R_{hh}(1 \times \Delta t) = \frac{1}{n-1}\sum_{j=1}^{n-1}[\frac{1}{N}\sum_{i=1}^{N}\overline{h}_i(j)\overline{h}_i(j+1)] \\
&\cdots \\
R_{hh}(k) &= R_{hh}(k \times \Delta t) = \frac{1}{n-k}\sum_{j=1}^{n-k}[\frac{1}{N}\sum_{i=1}^{N}\overline{h}_i(j)\overline{h}_i(j+k)] \\
&\cdots \\
R_{hh}(n-1) &= \frac{1}{N}\sum_{i=1}^{N}\overline{h}_i(1)\overline{h}_i(n).
\end{aligned}
\tag{5.39}
$$

It is obvious that the larger time interval $\tau$ the less reliable of $R_{hh}(\tau)$, which limits the precision of following $S_{hh}$ calculations. Thus, in the real calculation, we neglect the values of correlation function as $\tau > n \times \Delta t$.

(2) Step 2: $S_{hh}(f) = \int_{-\infty}^{+\infty} R_{hh}(\tau)e^{-2\pi i f\tau}d\tau$

According to the Wiener-Khintchine theorem, we can obtain

$$
\begin{aligned}
S_{hh}(f) &= \int_{-\infty}^{+\infty} R_{hh}(\tau)e^{-2\pi i f\tau}d\tau \\
&= \int_{+\infty}^{0} R_{hh}(-t)e^{2\pi i f t}d(-t) + \int_{0}^{+\infty} R_{hh}(\tau)e^{-2\pi i f\tau}d\tau \\
&= \int_{0}^{+\infty} R_{hh}(t)e^{2\pi i f t}d(t) + \int_{0}^{+\infty} R_{hh}(\tau)e^{-2\pi i f\tau}d\tau \\
&= \int_{0}^{+\infty} R_{hh}(\tau)e^{2\pi i f\tau}d(\tau) + \int_{0}^{+\infty} R_{hh}(\tau)e^{-2\pi i f\tau}d\tau \\
&= \int_{0}^{+\infty} R_{hh}(\tau)(e^{2\pi i f\tau} + e^{-2\pi i f\tau})d(\tau) \\
&= 2\int_{0}^{+\infty} R_{hh}(\tau)\cos(2\pi f\tau)d(\tau).
\end{aligned}
\tag{5.40}
$$

We introduce the vector $R$ which stores the correlation function of GB average migration

$$
\begin{aligned}
R_H &= [R_H(1), R_H(2), \ldots, R_H(n)]^{'} \\
R_H(j) &\equiv R_{hh}(t = j-1 \ \ ps) \ \ j = 1, 2, \ldots, n.
\end{aligned}
\tag{5.41}
$$

According to parameters in the following simulation section, the range of frequency in Fourier space is

$$\begin{aligned} f_{min} &= \frac{1}{n\ ps} = \frac{1}{n} \times 10^{12} Hz \\ f_{max} &= \frac{1}{1\ ps} = 10^{12} Hz. \end{aligned} \tag{5.42}$$

We define the vector $S$ which records the migration power spectrum function $S_{hh}$, where

$$\begin{aligned} S_H &= [S_H(1), S_H(2), \ldots, S_H(n)]' \\ S_H(j) &\equiv S_{hh}(f = \frac{j}{n} \times 10^{12} Hz) \ \ j = 1, 2, \ldots, n. \end{aligned} \tag{5.43}$$

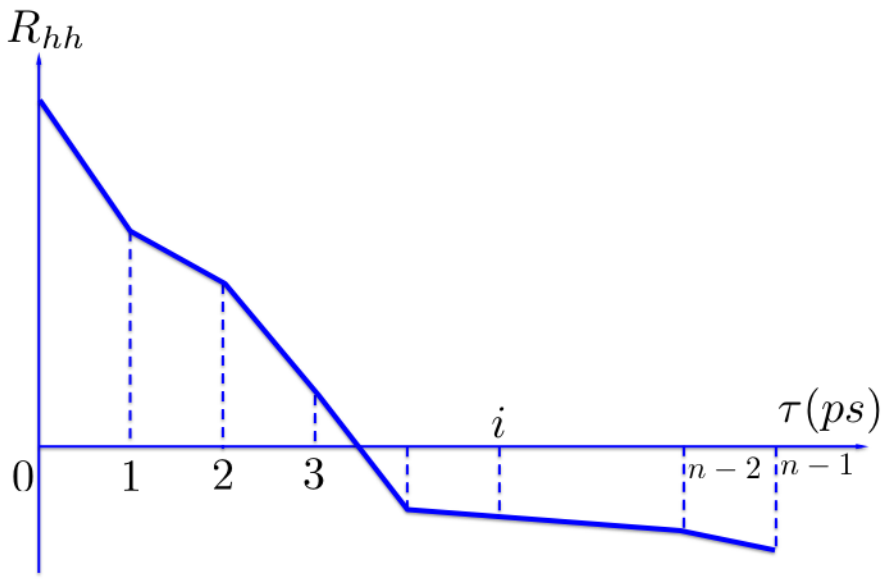


Figure 5.8: Schematic diagram of GB average migration correlation function $R_{hh}(\tau)$.

According to the Equation 5.40, we can obtain that

$$\begin{aligned} S_H(j) &= S_{hh}(\frac{j}{n} \times 10^{12} Hz) \\ &= 2 \times \Delta\tau \times [R_{hh}(0\ ps)\ cos(2\pi\frac{j}{n} \times 0) + R_{hh}(1\ ps)\ cos(2\pi\frac{j}{n} \times 1) + \dots \\ &+ R_{hh}(n-1\ ps)\ cos(2\pi\frac{j}{n} \times (n-1))] \\ &= 2\Delta\tau \bullet \sum_{j=1}^{n} R_H(i)\ cos[2\pi\frac{j}{n} \bullet (i-1)] \quad (\Delta\tau = 1\ ps). \end{aligned} \tag{5.44}$$

## 5.4 Simulation

### 5.4.1 Simulation Method

We used MD simulations to study the thermal fluctuations and mobility of tilt symmetric $\Sigma 5(310)$ grain boundaries with embedded second phase particles. Figure 5.9a gives a schematic of a bicrystal with two cylinder shaped second phase particles embedded in the GB. The size of the simulation cell is $\{133\mathring{A}, 222\mathring{A}, 10\mathring{A}\}$. The radius of the embedded particle is $r = 4.4525\mathring{A}$. The atomistic configuration of the GB and the particles is shown in Figure 5.9b. GB position is located by means of centro-symmetry parameters described by light region (green and yellow color). Dash-solid line represents the current GB position, solid line represents the present average GB position with displacement $\bar{h}$ respect to the central axis of two second phase particles (red cylinder with radius $r$). All the atoms are Ni, and the cylinder shaped particles are considered as rigid bodies to circumvent the complexity due to diffusion of the embedded particles. Figure 5.9 only shows the sample with two paticles. In our simulation, the number of second phase particles are varied from $N = 1$ to $N = 3$ for each GB structures.

Simulations were performed using LAMMPS [110] and EAM interatomic potential for Nickel [163] with periodic boundary conditions in all directions. The

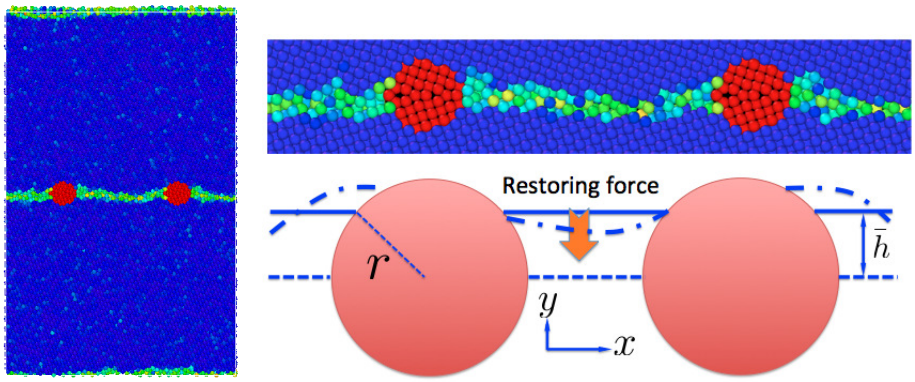


Figure 5.9: (a) Schematic configuration of simulation cell. (b) Typical snapshot of MD simulation atoms with red color constitute two rigid second phase particles and interaction with GB.

time step is set to be 5 fs. To simplify the problem and emphasize on second phase particles impact, we fix all the second phase particles through the whole simulation procedures. In order to remove the residual stress around the second phase particles, the simulation cell is relaxed by means of 'heating-and-quenching' approach. To be specific, each system is first equilibrated at 1200K for 25 ps under the NPT ensemble, then gradually annealed to the desired temperature for 25 ps, and subsequently relaxed at desired temperature for another 25 ps. After this relaxation process, the sample is equilibrated for 2 ns under the NVT ensemble using the Nose-Hoover thermostat. The atomistic configuration of the simulation cell is observed every 1 ps. Using the approach described in our previous work [112], we extract extract the evolution of the GB profile and the corresponding average position of the GB.

### 5.4.2 Simulation Results and Discussion

#### Validation of the Migration Power Spectrum Method

Our migration power spectrum (MPS) method is verified by comparing the GB mobility and migration activation energy with the adapted interface random walk (AIRW) for pure Ni $\Sigma 5$ GB without second phase particles. The simulation

is run from 300K to 1200K. All the parameters are the same as those mentioned above. The calculations are based on two equations, specifically, for the MPS method

$$S_{hh}(f) = \frac{Mk_BT}{2\pi^2 Sf^2}$$

and for the AIRW method

$$D = \frac{d < \vec{d}^2 >}{dt} \sim \frac{2Mk_BT}{S}.$$

Figure 5.10 and 5.11 shows the Ni Σ5 GB diffusion curve in the frequency domain (corresponding to the MPS method) and in the time domain (corresponding to the AIRW method) without second phase particles at temperature 300K and 1000K. At 300K, the diffusion curves do not provide a good fit using linear regression for both the methods. The GB mobility extracted from the MPS method is ($M = 2.00 \times 10^{-10} m^4 J^{-1} s^{-1}$) larger by a factor of around 7 than that from the AIRW method ($M = 3.01 \times 10^{-11} m^4 J^{-1} s^{-1}$). As the temperature increases, we get a better linear fit as expected for both cases, as shown in Figure 5.11, and the difference in mobility becomes very small. To be specific, the mobility values from the MPS and AIRW method at 1000K are $M = 1.00 \times 10^{-7} m^4 J^{-1} s^{-1}$ and $M = 8.60 \times 10^{-8} m^4 J^{-1} s^{-1}$ respectively.

Figure 5.10 and 5.11 shows the Ni Σ5 GB diffusion curve in the frequency domain (corresponding to the MPS method) and in the time domain (corresponding to the AIRW method) without second phase particles at temperature 300K and 1000K. At 300K, the diffusion curves do not provide a good fit using linear regression for both the methods. The GB mobility extracted from the MPS method is ($M = 2.00 \times 10^{-10} m^4 J^{-1} s^{-1}$) larger by a factor of around 7 than that from the AIRW method ($M = 3.01 \times 10^{-11} m^4 J^{-1} s^{-1}$). As the temperature increases, we get a better linear fit as expected for both cases, as shown in Figure 5.11, and the difference in mobility becomes very small. To be specific, the mobility values

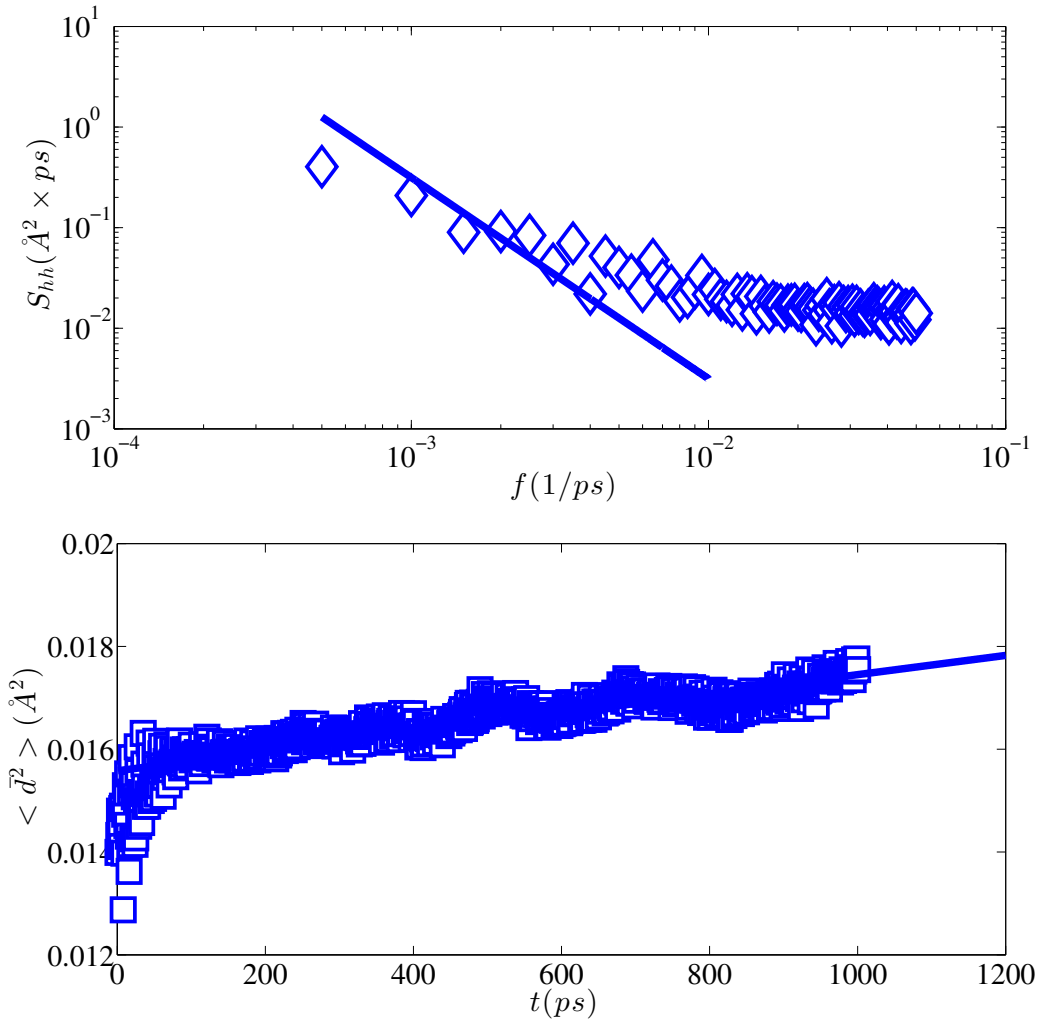


Figure 5.10: Ni Σ5 GB diffusion curve at temperature 300K (a)Migration power spectrum method. (b)Adapted interface random walk method.

from the MPS and AIRW method at 1000K are $M = 1.00 \times 10^{-7} m^4 J^{-1} s^{-1}$ and $M = 8.60 \times 10^{-8} m^4 J^{-1} s^{-1}$ respectively.

The variation of the mobility with temperature using both methods is plotted in Figure 5.12. Overall, the mobilities calculated from the MPS method are larger than those from the AIRW method. This discrepancy is obvious at lower temperatures and is negligible at higher temperatures. The red and blue lines represent the fitting curves, from which, it is clear that there exist two different temperature regimes. This is indicated by the abrupt change in the slope of the fit-

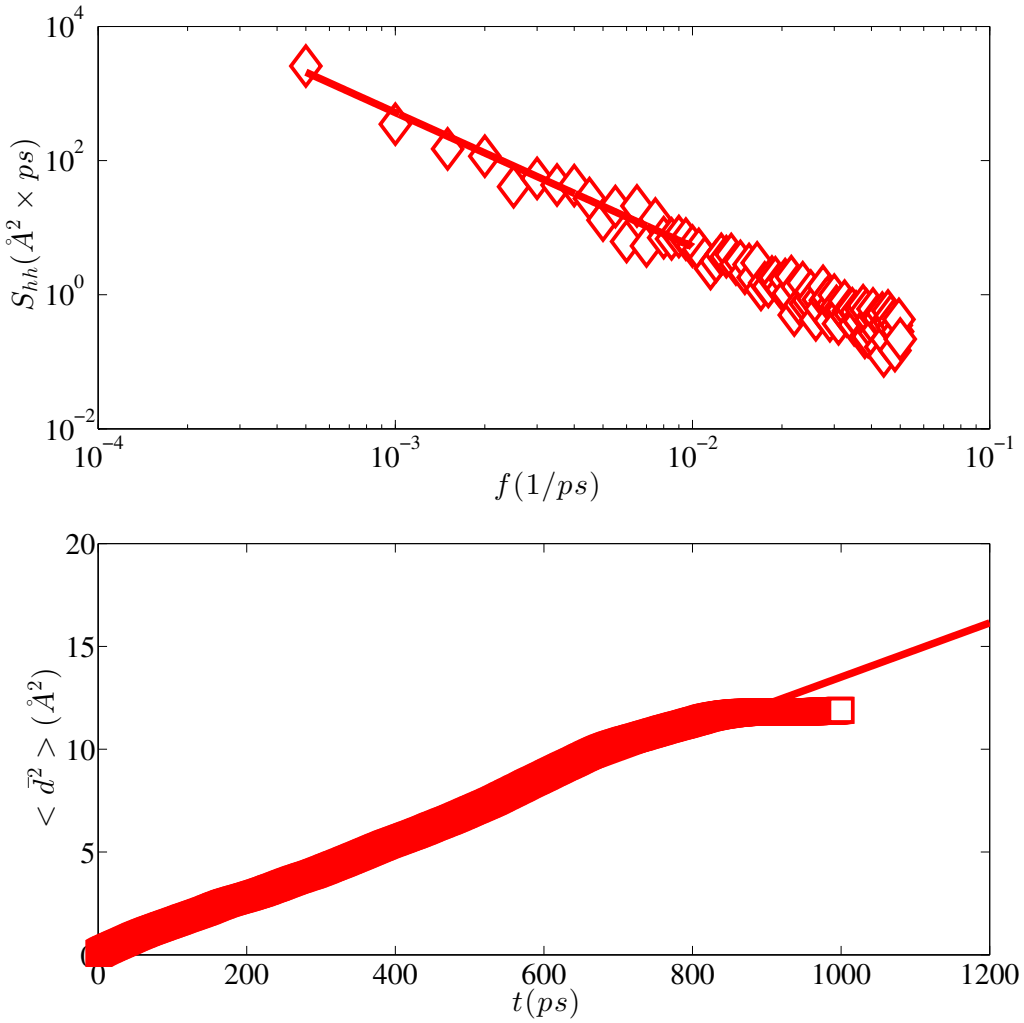


Figure 5.11: Ni Σ5 GB diffusion curve at temperature 1000K (a)Migration power spectrum method. (b)Adapted interface random walk method.

ting curves, with the transition temperature being around 700 K. Our results from both methods reveals that the dependance of mobility on temperature follows the conventional Arrhenius relation Equation 5.2,

$$M = M_0 exp(-\frac{Q_m}{k_B T}).$$

The migration activation energies for MPS method are $Q_1 = 0.1020ev$ and $Q_2 = 0.7225ev$ at lower and higher temperature regions similar to $Q_1 = 0.1777ev$ and $Q_2 = 0.7292ev$ for AIRW method.

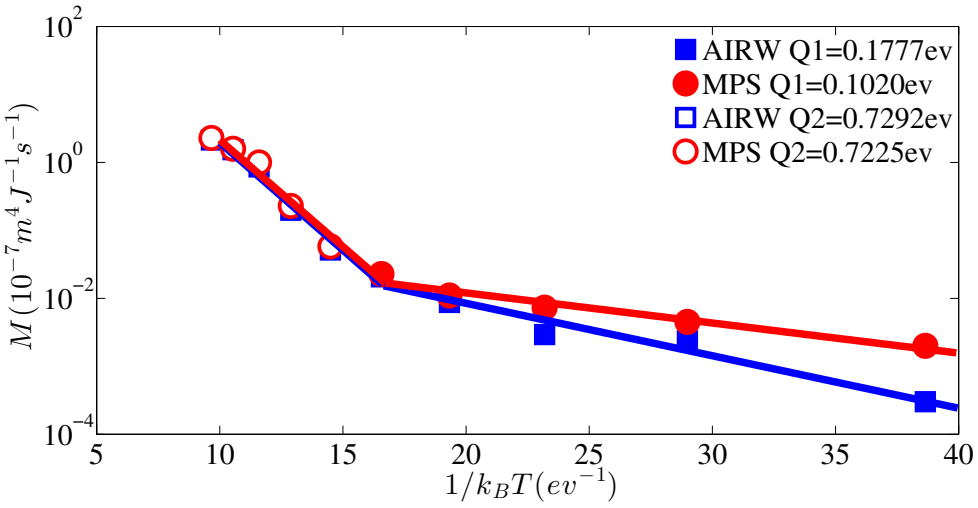


Figure 5.12: Arrhenius mobility plot for Ni Σ5. The circle and rectangular symbols represent the simulations results arises from the MPS method and AIRW method respectively.

**Second Phase Particles Effect**

With the presence of second phase particles, the GB mobility tends to decrease. The calculations are based on two equations, specifically, for the MPS method

$$S_{hh}(f) = \frac{2Mk_BT}{4\pi^2Sf^2 + M^2k_s^2S}$$

and for the AIRW method

$$\begin{aligned} < \bar{h}^2(t) > &= \frac{k_BT}{Sk_s}(1 - e^{-2Mk_st}) \\ &= \begin{cases} \frac{2Mk_BT}{S}t & \text{if } t \ll \frac{1}{Mk_s} \\ \frac{k_BT}{Sk_s} & \text{if } t \gg \frac{1}{Mk_s}. \end{cases} \end{aligned}$$

Figure 5.13 shows the mobility results at temperature 1000K for GB structure with different second phase particles, where $N = 0, 1, 2, 3$ represent the number of second phase particles. For the MPS method, we do the curve fitting for larger frequency regime; For AIRW, the mobility can be obtained from the slope of fitting curve in initial time regime. Table 5.1 lists mobility values extracted from

the MPS method and the AIRW method for different second phase particles. It is clear that the mobility decrease with more second phase particles and the results from both methods agree very well with each other.

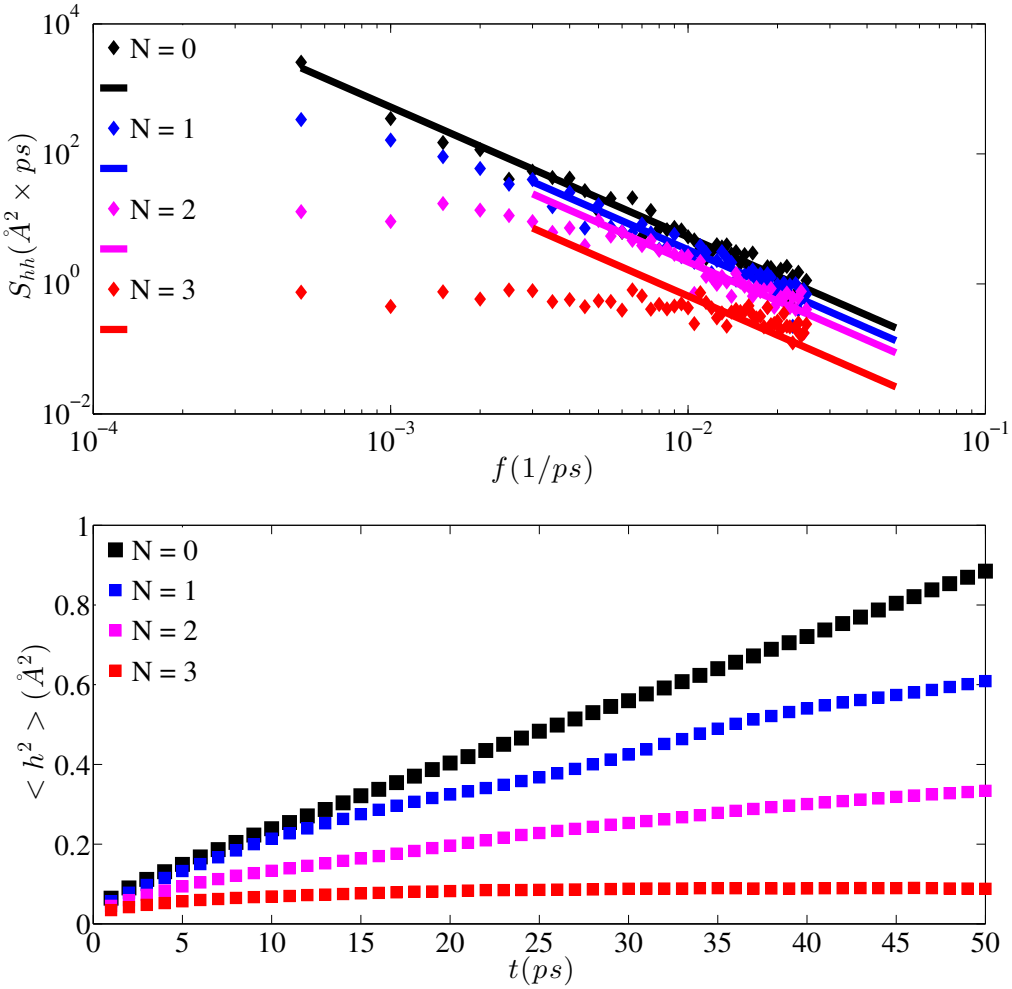


Figure 5.13: Modified GB mobility calculation details at temperature 1000K. (a) MPS method. Curve fitting for larger frequency (b) AIRW method. Curve fitting for initial time.

Table 5.1: Mobility values extracted from the MPS method and the AIRW method for different second phase particles at 1000K.

| | N = 0 | N = 1 | N = 2 | N = 3 |
|---|---|---|---|---|
| MPS ($m^4J^{-1}s^{-1}$) | $8.60 \times 10^{-8}$ | $6.80 \times 10^{-8}$ | $3.84 \times 10^{-8}$ | $1.21 \times 10^{-8}$ |
| AIRW ($m^4J^{-1}s^{-1}$) | $1.00 \times 10^{-7}$ | $6.38 \times 10^{-8}$ | $4.15 \times 10^{-8}$ | $1.24 \times 10^{-8}$ |

We further obtain the modified GB mobility dependence on the temperature with different second phase particles, as shown in Figure 5.14. For each method, the absolute value of slopes of the fitted lines decrease with more second phase particles embedded into the GB. The specific values can be represented by the GB migration energy denoted by $Q_0, Q_1, Q_2, Q_3$ for $N = 0, 1, 2, 3$ second phase particles respectively. The Arrhenius relationship between mobility and temperature always exists whether there are second phase particles or not. With more second phase particles embedded in the GB, migration becomes more difficult, which is consistent with the increasing migration activation energies $Q_0 < Q_1 < Q_2 < Q_3$. The results from MPS method and AIRW method are close to each other.

## 5.5 Conclusion

In summary, we propose the a calculation method (the MPS method) to obtain GB mobility in Fourier space based on the random walk model, and extend the current adapted interface random walk model (AIRW)and the MPS model to account for the drag effect of second phase particles. By introducing the GB migration correlation function and migration power spectrum function, we derive the GB diffusion equation in Fourier space and propose the new calculation method to capture the mobility. Our simulation reveals that the mobilities extracted from MPS method are larger than those of AIRW method at lower temperature, but with increasing temperature this discrepancy gets smaller and can be neglected. This provides a new way to study the mechanical properties related to GB mobility.

Our theory model accounting for the drag effect of second phase particles reveals that the original source of restoring force stems from the energy difference base the relative position of particles and GB. Due to this drag effect the GB dif-

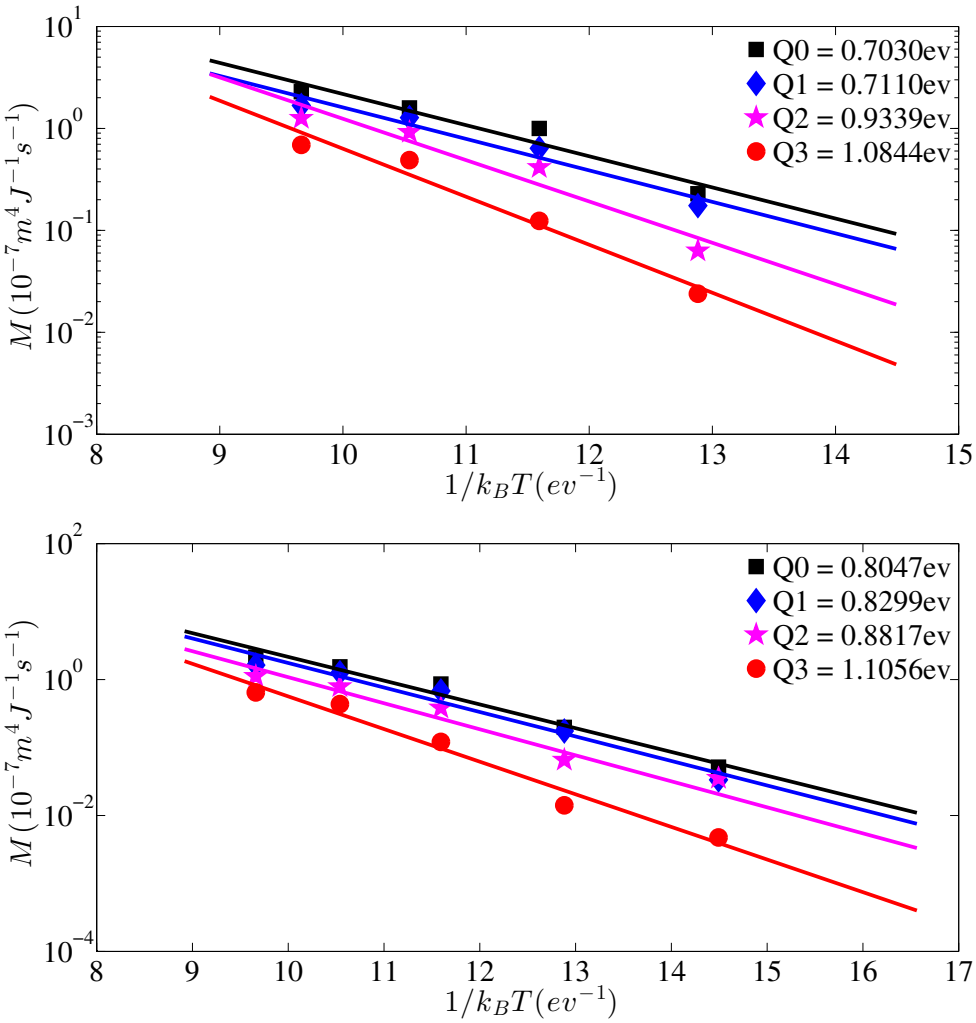


Figure 5.14: Arrhenius mobility plot at high temperature region for Ni Σ5 with several second phase particles from (a) MPS method and (b) AIRW method.

fusion can approach the limit value after the long time interval. MD simulations result verify our theory and show that modified GB mobility reduces with more second phase particles which is consistent to our common intuition. The Arrhenius relationship between mobility and temperature always exists whether there is second phase particles or not.

# Chapter 6 Summary and Future Work

Here, we summarize our study of the thermal fluctuations of grain boundaries and twin boundaries using atomistic simulations and statistical mechanics based modeling and present directions for future work. In Chapter 2, we investigate the thermal fluctuations of twin boundaries in FCC metals to elucidate the deformation mechanism governing their kinetic properties by way of molecular dynamics simulations. The simulation results show that the twin boundary motion is strongly coupled to shear deformation up to $0.95T_m$ homologous temperature. A rather unexpected observation is that coherent TBs do not exhibit any capillarity- induced fluctuations even at high temperatures, in sharp contrast to other high-angle grain boundaries.

In Chapter 3, we extend this work to further elucidate the entropic interaction between fluctuating twin boundaries constituting a nanotwinned structure at finite temperature. To this end, we begin by comparing the thermal fluctuation curves for an array of parallel twin boundaries with different spacing. The simulations reveal that the fluctuations of twin boundaries are significantly enhanced in the presence of adjoining twin boundaries as their spacing $d$ decreases, which is a remarkable signature of an attractive force. Through rigorous statistical mechanics modeling based on a continuum representation of twin boundaries, we prove the existence of an entropic attractive force which enhances their thermal fluctuations and which decreases as $1/d^2$. This rather surprising attraction between fluctuating twin boundaries is dominated by the deformation of the elastic medium between adjoining interfaces, and hence is fundamentally distinct from the entropic pressure resulting from steric hindrance in the case of biomembranes and high angle boundaries. This is an exciting result because the attractive force can enhance the stability of nanotwinned metals by preventing adjacent twin bound-

aries from moving apart. This structural stability is advantageous in the light of nanocrystalline metals which have a high density of high-angle grain boundaries and hence suffer from grain growth due to grain boundary migration and sliding.

In addition to the entropic force, in Chapter 4, we also investigate the long-range thermal force inside these NT metals. The simulations reveal that for all TB spacing $d$, this thermal stress decays as $1/d$. We present a simple analytical model to show that the $1/d$ dependence stems from the inhomogeneity in the thermal expansion coefficient due to the interfacial regions.

In Chapter 5, we use thermal fluctuations to investigate the migration of grain boundaries in the presence of defects, specifically, second phase particles. To this end, first extend the current adapted interface random walk model to account for the drag effect of second phase particles. We also propose a new method (that we refer to as the migration power spectrum method) to obtain the GB mobility in Fourier space based on the random walk model.

In Chapter 5, we propose the new calculation method (MPS method) to obtain GB mobility in Fourier space based on the random walk model, and extend current adapted interface random walk model (AIRW) the MPS model to account for the drag effect of second phase particles. Our simulation reveals that the mobilities extracted from MPS method are larger than those of AIRW method at lower temperature, but increase in temperature, this discrepancy gets smaller and can be neglected. It also shows that the GB mobility reduces with more second phase particles which is consistent to our common intuition. The Arrhenius relationship between mobility and temperature always exists whether there are second phase particles or not. Qualitatively, our results show that migration becomes harder as more second phase particles are embedded into the GB, which also reflects in the increasing migration activation energies. However, more work is needed to quantify the effect of density and size of second phase particles on

the migration activation energies, which is part of the ongoing work. There are a number of unknown but interesting topics on the drag coefficient of second phase particles. For example, even though we have established the formula to describe it, we have not performed an explicit investigation of how the temperature, particles size, surface tension of GB affect this coefficient. It is worth digging deeper into this promising subject. Another important future direction is to extend the model to capture the effect of point-defects, specifically, interstitials and dopant atoms, on the migration of GBs. These studies can provide insights into the response and structural stability of nanostructured materials undergoing radiation damage. Finally, applying the models developed in this dissertation to study the thermal fluctuations of two-dimensional materials, such as graphene, with and without defects, opens avenues for future research.

# References


[1] H. Gleiter, "Nanocrystalline Materials," *Progress in Materials Science*, vol. 33, no. 4, pp. 223–315, 1989.

[2] H. Gleiter, "Nanostructured Materails: Basic Concepts and Microstructure," *Acta Materialia*, vol. 48, no. 1, pp. 1–29, 2000.

[3] C. Suryanarayana and C. Koch, "Nanocrystalline Materials Ð Current Research and Future Directions," *Hyperfine Interactions*, vol. 130, no. 1-4, pp. 5–44, 2000.

[4] T. Hanlon, Y. Kwon, and S. Suresh, "Grain size effects on the fatigue response of nanocrystalline metals," *Scripta Materialia*, vol. 49, no. 7, pp. 675–680, 2003.

[5] M. Meyers, A. Mishra, and D. Benson, "Mechanical properties of nanocrystalline materials," *Progress in Materials Science*, vol. 51, no. 4, pp. 427–556, 2006.

[6] P. Schelling, S. Phillpot, and P. Keblinski, "Kapitza conductance and phonon scattering at grain boundaries by simulation," *Journal of Applied Physics*, vol. 95, no. 11, p. 6082, 2004.

[7] B. Feng, Z. Li, and X. Zhang, "Effect of grain-boundary scattering on the thermal conductivity of nanocrystalline metallic films," *Journal of Physics D: Applied Physics*, vol. 42, no. 5, p. 5311, 2009.

[8] A. Bagri, S. Kim, R. Ruoff, and V. Shenoy, "Thermal transport across Twin Grain Boundaries in Polycrystalline Graphene from Nonequilibrium Molecular Dynamics Simulations," *Nano Letters*, vol. 11, no. 9, pp. 3917–3921, 2011.

[9] A. Limarga and D. Clarke, "The grain size and temperature dependence of the thermal conductivity of polycrystalline, tetragonal yttria-stabilized zirconia," *Applied Physics Letters*, vol. 98, no. 21, p. 1906, 2011.

[10] A. Cao and J. Qu, "Kapitza conductance of symmetric tilt grain boundaries in graphene," *Journal of Applied Physics*, vol. 11, no. 5, p. 3529, 2012.

[11] P. Wang, B. Gong, Q. Feng, and T. Wang, "Simulations of thermal conductance across tilt grain boundaries in graphene," *Acta Mechanica Sinica*, vol. 28, no. 6, pp. 1528–1531, 2012.

[12] A. Serov, Z. Ong, and E. Pop, "Effect of grain boundaries on thermal transport in graphene," *Applied Physics Letters*, vol. 102, no. 3, p. 3104, 2013.

[13] S. Tang and Y. Kulkarni, "The interplay between strain and size effects on the thermal conductance of grain boundaries in graphene," *Applied Physics Letters*, vol. 103, no. 21, p. 3113, 2013.

[14] H. Dong, B. Wen, and R. Melnik, "Relative importance of grain boundaries and size effects in thermal conductivity of nanocrystalline materials," *Scientific Reports*, vol. 4, p. 7037, 2014.

[15] H. Liu, Y. Lin, and S. Luo, "Grain Boundary Energy and Grain Size Dependences of Thermal Conductivity of Polycrystalline Graphene," *The Journal of Physical Chemistry C*, vol. 118, no. 42, pp. 24 797–24 802, 2014.

[16] R. DM and V. Shukla, "The effect of phonon?grain boundary scattering on the lattice thermal conductivity and thermoelectric conversion efficiency of heavily doped fine?grained, hot?pressed silicon germanium alloy," *Journal of Applied Physics*, vol. 52, no. 12, pp. 7421–7426, 1981.

[17] G. Palasantzas, "Surface roughness and grain boundary scattering effects on the electrical conductivity of thin films," *Physical Review B*, vol. 58, no. 15, pp. 9685–9688, 1998.

[18] A. Tschope, E. Sommer, and R. Birringer, "Grain size-dependent electrical conductivity of polycrystalline cerium oxide I. Experiments," *Solid State Ionics*, vol. 139, no. 3, pp. 255–265, 2011.

[19] A. Tschope, E. Sommer, and R. Birringer, "Grain size-dependent electrical conductivity of polycrystalline cerium oxide II: Space charge model," *Solid State Ionics*, vol. 139, no. 3, pp. 267–280, 2011.

[20] W. Wu, S. Brongersma, V. Hove, and K. Maex, "Influence of surface and grain-boundary scattering on the resistivity of copper in reduced dimensions," *Applied Physics Letters*, vol. 84, no. 15, pp. 2838–2840, 2004.

[21] Q. Zhang, X. Zhang, and B. Cao, "Influence of grain boundary scattering on the electrical properties of platinum nanofilms," *Applied Physics Letters*, vol. 89, no. 11, p. 114102, 2006.

[22] H. Zeng, Y. Wu, J. Zhang, C. Kuang, M. Yue, and S. Zhou, "Grain size-dependentelectricalresistivityofbulk nanocrystalline Gdmetals," *Progress in Natural Science: Materials International*, vol. 23, no. 1, pp. 11–22, 2012.

[23] C. Koch, "Optimization of strength and ductility in nanocrystalline and ultrafine grained metals," *Scripta Materialia*, vol. 49, no. 7, pp. 657–662, 2003.

[24] K. Kumar, H. Swygenhoven, and S. Suresh, "Mechanical behavior of nanocrystalline metals and alloys," *Acta Materialia*, vol. 51, no. 19, pp. 5743–5774, 2003.

[25] N. Hansen, "Hall-Petch relation and boundary strengthening," *Scripta Materialia*, vol. 51, no. 8, pp. 801–806, 2004.

[26] Y. Zhu and X. Liao, "Nanostructured Metals: Retaining ductility," *Nature Materials*, vol. 3, pp. 351–352, 2004.

[27] C. Carlton and P. Ferreira, "What is behind the inverse Hall?Petch effect in nanocrystalline materials?" *Acta Materialia*, vol. 55, no. 11, pp. 3749–3756, 2007.

[28] L. Lu, Y. Shen, X. Chen, L. Qian, and K. Lu, "Ultrahigh Strength and High Electrical Conductivity in Copper," *Science*, vol. 304, no. 5669, pp. 422–426, 2004.

[29] X. Zhang, H. Wang, X. Chen, L. Lu, K. Lu, R. Hoagland, and A. Misra, "High-strength sputter-deposited Cu foils with preferred orientation of nanoscale growth twins," *Applied Physics Letters*, vol. 88, no. 17, p. 173116, 2006.

[30] M. Dao, L. Lu, R. Asaro, J. De Hosson, and E. Ma, "Toward a Quantitative Understanding of Mechanical Behavior of Nanocrystalline Metals," *Acta Materialia*, vol. 55, no. 12, pp. 4041–4065, 2007.

[31] A. Hodge, Y. Wang, and T. Barbee, Jr, "Mechanical deformation of high-purity sputter-deposited nano-twinned copper," *Scripta Materialia*, vol. 59, no. 2, pp. 163–166, 2008.

[32] L. Lu, X. Chen, X. Huang, and K. Lu, "Revealing the Maximum Strength in Nanotwinned Copper," *Science*, vol. 323, no. 5914, pp. 607–610, 2009.

[33] W. Hosford, *Mechanical Behavior of Materials*. Cambridge University Press, 2005.

[34] D. Farkas, H. Swygenhove, and P. Derlet, "Intergranular fracture in nanocrystalline," *Physical Review B*, vol. 66, no. 6, p. 060101, 2002.

[35] A. Latapie and D. Farkas, "Molecular dynamics simulations of stress-induced phase transformations and grain nucleation at crack tips in fe," *Modelling and Simulation in Materials Science and Engineering*, vol. 11, no. 5, pp. 745–753, 2003.

[36] S. Frederiksen, K. Jacobsen, and J. Schiotz, "Simulations of intergranular fracture in nanocrystalline molybdenum," *Acta Materialia*, vol. 52, no. 17, pp. 5019–5029, 2004.

[37] A. Cao and Y. Wei, "Atomistic simulations of crack nucleation and intergranular fracture in bulk nanocrystalline nickel," *Physical Review B*, vol. 76, no. 2, p. 024113, 2007.

[38] M. Buehler, H. Yao, H. Gao, and B. Ji, "Cracking and adhesion at small scales: atomistic and continuum studies of flaw tolerant nanostructures," *Modelling and Simulation in Materials Science and Engineering*, vol. 14, no. 5, pp. 799–816, 2006.

[39] A. K. Mukherjee, J. E. Bird, and J. E. Dorn, "Experimental Correlations for High-Temperature Creep," *ASM Transactions*, vol. 62, pp. 155–179, 1969.

[40] P. Sanders, M. Rittner, E. Kiedaisch, J. Weertman, H. Kung, and Y. Lu, "Creep of Nanocrystalline Cu, Pd, and Al-Zr," *Nanostructured Materials*, vol. 9, no. 1-8, pp. 433–440, 1997.

[41] F. A. Mohamed and Y. Li, "Creep and Superplasticity in Nanocrystalline Materials: Current Understanding and Future Prospects," *Materials Science and Engineering A*, vol. 298, no. 1-2, pp. 1–15, 2001.

[42] Y. Wang, A. Ishii, and S. Ogata, "Transition of Creep Mechanism in Nanocrystalline Metals," *Physical Review B*, vol. 84, p. 224102, 2011.

[43] S. Jiao and Y. Kulkarni, "Molecular dynamics study of creep mechanisms in nanotwinned metals," *Computational Materials Science*, vol. 110, pp. 254–260, 2015.

[44] [Online]. Available: https://en.wikipedia.org/wiki/Grain_boundary

[45] D. Hull and D. Bacon, *Introduction to Dislocations, Fourth Edition*. Butterworth-Heinemann, 2001.

[46] M. Kronberg and F. Wilson, "Secondary recrystallization in copper," *Metall Trans*, vol. 185, pp. 501–514, 2012.

[47] M. Dao, L. Lu, Y. Shen, and S. Suresh, "Strength, strain-rate sensitivity and ductility of copper with nanoscale twins," *Acta Materialia*, vol. 54, no. 20, pp. 5421–5432, 2006.

[48] K. Lu, L. Lu, and S. Suresh, "Strengthening Materials by Engineering Coherent Internal Boundaries at the Nanoscale," *Science*, vol. 324, no. 5925, pp. 349–352, 2009.

[49] Y. Kulkarni and R. J. Asaro, "Are Some Nanotwinned FCC Metals Optimal for Strength, Ductility and Grain Stability," *Acta Materialia*, vol. 57, no. 16, pp. 4835–4844, 2009.

[50] Y. Kulkarni, R. J. Asaro, and D. Farkas, "Are Nanotwinned Structures in FCC Metals Optimal for Strength, Ductility and Grain Stability," *Scripta Materialia*, vol. 60, no. 7, pp. 532–535, 2009.

[51] X. Li, Y. Wei, L. Lu, K. Lu, and H. Gao, "Dislocation Nucleation Governed Softening and Maximum Strength in Nano-Twinned Metals," *Nature*, vol. 464, no. 7290, pp. 877–880, 2010.

[52] X. Guo and Y. Xia, "Repulsive force vs. source number: Competing mechanisms in the yield of twinned gold nanowires of finite length," *Acta Materialia*, vol. 59, no. 6, pp. 2350–2357, 2011.

[53] D. Jang, X. Li, H. Gao, and J. R. Greer, "Deformation Mechanisms in Nanotwinned Metal Nanopillars," *Nature Nanotechnology*, vol. 7, no. 9, pp. 594–601, 2012.

[54] J. Wang, F. Sansoz, J. Huang, Y. Liu, S. Sun, Z. Zhang, and S. X. Mao, "Near-Ideal Theoretical Strength in Gold Nanowires Containing Angstrom Scale Twins," *Nature Communications*, vol. 4, p. 1742, 2013.

[55] Y. Wang, F. Sansoz, T. LaGrange, R. Ott, J. Marian, T. Barbee Jr, and A. Hamza, "Defective Twin Boundaries in Nanotwinned Metals," *Nature Materials*, vol. 12, pp. 697–702, 2013.

[56] H. Mirkhani and P. Joshi, "Mechanism-based crystal plasticity modeling of twin boundary migration in nanotwinned face-centered-cubic metals," *Journal of the Mechanics and Physics of Solids*, vol. 68, no. 8, pp. 107–133, 2014.

[57] T. Wright, N. Daphalapurkar, and K. Ramesh, "Stability of ideal fcc twin boundaries," *Journal of the Mechanics and Physics of Solids*, vol. 73, no. 12, pp. 228–241, 2014.

[58] T. Shen, S. Feng, M. Tang, J. Valdez, Y. Wang, and K. Sickafus, "Enhanced radiation tolerance in nanocrystalline MgGa2O4," *Applied Physics Letters*, vol. 98, no. 26, p. 3115, 2007.

[59] X. Bai, A. Voter, R. Hoagland, M. Nastasi, and B. Uberuaga, "Efficient Annealing of Radiation Damage Near Grain Boundaries via Interstitial Emission," *Science*, vol. 327, no. 5973, pp. 1631–1634, 2010.

[60] I. Beyerlein, A. Caro, M. Demkowicz, N. Mara, A. Misra, and B. Uberuaga, "Radiation damage tolerant nanomaterials," *Materials Today*, vol. 16, no. 11, pp. 443–449, 2010.

[61] Y. Chang, Q. Guo, J. Zhang, L. Chen, Y. Long, and F. Wan, "Irradiation effects on nanocrystalline materials," *Frontiers of Materials Science*, vol. 7, no. 2, pp. 143–155, 2013.

[62] R. Davidchack and B. Laird, "Direct calculation of the hard-sphere crystal/melt interfacial free energy," *Physical Review Letters*, vol. 85, no. 22, p. 4751, 2000.

[63] A. Karma and A. Lobkovsky, "Low-temperature dynamics of kinks on Ising interfaces," *Physical Review E*, vol. 71, no. 3, p. 036114, 2005.

[64] H. Zhang, M. Mendelev, and D. Srolovitz, "Computer simulation of the elastically driven migration of a flat grain boundary," *Acta Materialia*, vol. 52, no. 9, pp. 2269–2576, 2004.

[65] M. Upmanyu, D. Srolovitz, L. Shvindlerman, and G. Gottstein, "Misorientation dependence of intrinsic grain boundary mobility: simulation and experiment," *Acta Metallurgica*, vol. 47, no. 14, pp. 3901–3914, 1999.

[66] H. Zhang, M. Mendelev, and D. Srolovitz, "Curvature driven grain boundary migration in aluminum: molecular dynamics simulations," *Acta Materialia*, vol. 53, no. 1, pp. 79–86, 2005.

[67] K. Janssens, D. Olmsted, and E. Holm, "Computing the mobility of grain boundaries," *Nature Material*, vol. 5, pp. 124–127, 2006.

[68] S. Foiles and J. Hoyt, "Computation of grain boundary stiffness and mobility from boundary fluctuations," *Acta Materialia*, vol. 54, no. 12, pp. 3351–3357, 2006.

[69] J. Hoyt, M. Asta, and A. Karma, "Method for computing the anisotropy of the solid-lipid interfacial free energy," *Physical Review Letters*, vol. 86, no. 24, p. 5530, 2001.

[70] J. Hoyt and M. Asta, "Atomistic computation of liquid diffusivity, solid-liquid interfacial free energy, and kinetic coefficient in Au and Ag," *Physical Review B*, vol. 65, no. 21, p. 214106, 2002.

[71] J. Hoyt, M. Asta, and A. Karma, "Atomistic and continuum modeling of dendritic solidification," *Modelling and Simulation in Materials Science and Engineering*, vol. 41, no. 6, pp. 121–163, 2003.

[72] J. Hoyt, Z. Trautt, and M. Upmanyu, "Fluctuation in molecular dynamics simulation," *Mathematics and Computers in Simulation*, vol. 80, no. 7, pp. 1382–1392, 2010.

[73] A. Karma, Z. Trautt, and Y. Mishin, "Relationship between equilibrium fluctuations and shear-coupled motion of grain boundaries," *Physical Review Letters*, vol. 109, no. 09, p. 095501, 2012.

[74] Z. Trautt, M. Upmanyu, and A. Karma, "Interface mobility from interface random walk," *Science*, vol. 314, no. 5799, pp. 632–635, 2006.

[75] C. Deng and C. Schuh, "Atomistic simulation of slow grain boundary motion," *Physical Review Letters*, vol. 106, no. 4, p. 045503, 2011.

[76] C. Deng and C. Schuh, "Diffusive to ballistic transition in grain boundary motion studied by atomistic simulations," *Physical Review B*, vol. 84, no. 21, p. 214102, 2011.

[77] M. Parrinello and A. Rahman, "Strain fluctuation and elastic constants," *The Journal of Chemical Physics*, vol. 76, no. 5, pp. 2662–2666, 1982.

[78] J. Ray, "Molecular dynamics equations of motion for systems varying in shape and size," *The Journal of Chemical Physics*, vol. 79, no. 10, pp. 5128–5130, 1983.

[79] J. Ray and M. Moody, "Calculation of elastic constants using isothermal molecular dynamics," *Physical Review B*, vol. 33, no. 2, pp. 895–899, 1986.

[80] L. Pratt, "Fluctuation method for calculation of elastic constants of solids," *The Journal of Chemical Physics*, vol. 87, no. 2, pp. 1245–1247, 1983.

[81] T. Cagin and J. Ray, "Third-order elastic constants from molecular dynamics: Theory and an example calculation," *Physical Review B*, vol. 38, no. 12, pp. 7940–7946, 1988.

[82] A. Gusev, M. Zehnder, and U. Suter, "Fluctuation formula for elastic constants," *Physical Review B*, vol. 54, no. 1, pp. 1–4, 1996.

[83] M. Meyers, J. Rickman, and T. Delph, "The calculation of elastic constants from displacement fluctuations," *Journal of Applied Physics*, vol. 98, no. 6, p. 066106, 2005.

[84] R. Maranganti and P. Sharma, "A novel atomistic approach to determine strain-gradient elasticity constants: Tabulation and comparison for various metals, semiconductors, silica, polymers and the (Ir) relevance for nanotechnologies," *Journal of the Mechanics and Physics of Solids*, vol. 55, no. 9, pp. 1823–1852, 2007.

[85] L. Landau and E. Lifshitz, *Statistical Physics*. Pergamon, New York, 1980.

[86] S. Safran, *Statistical Thermodynamics of Surfaces, Interfaces, and Membranes*. Westview Press, 2003.

[87] D. Nelson, *Statistical Mechanics of Membranes and Surfaces*. World Science Plublishing, 2004.

[88] D. Chen and Y. Kulkarni, "Entropic interaction between fluctuating twin boundaries," *Journal of the Mechanics and Physics of Solids*, vol. 84, no. 11, pp. 59–71, 2015.

[89] J. Los, M. Katsnelson, O. Yazyev, K. Zakharchenko, and A. Fasolino, "Scaling properties of flexible membranes from atomistic simulations: application to graphene," *Physical Review B*, vol. 80, no. 12, p. 121405, 2009.

[90] W. Gao and R. Huang, "Thermomechanics of monolayer graphene: rippling, thermal expansion and elasticity," *Journal of the Mechanics and Physics of Solids*, vol. 66, no. 2, pp. 42–58, 2014.

[91] D. Rapaport, *The Art of Molecular Dynamics Simulation, 2nd Edition*. Cambridge University Press, 2004.

[92] V. Bulatov and W. Cai, *Computer simulations of dislocations*. Oxford University Press, 2006.

[93] J. Jones, "On the Determination of Molecular Fields," *Proceedings of the Royal Society A*, vol. 146, no. 738, p. 463?477, 1924.

[94] M. S. Daw and M. I. Baskes, "Embedded-Atom Method: Derivation and Application to Impurities, Surfaces, and Other Defects in Metals," *Physical Review B*, vol. 29, no. 12, p. 6443, 1984.

[95] L. Verlet, "Computer "Experiments" on Classical Fluids. I. Thermodynamical Properties of Lennard-Jones Molecules," *Physical Review B*, vol. 159, no. 1, p. 98?103, 1967.

[96] M. Hestenes and E. Stiefel, "Methods of Conjugate Gradients for Solving Linear Systems," *Journal of Research of the National Bureau of Standards*, vol. 49, no. 6, pp. 409–436, 1952.

[97] A. Cao, Y. Wei, and X. Mao, "Molecular Dynamics Simulation of Plastic Deformation of Nanotwinned Copper," *Applied Physics Letters*, vol. 90, no. 15, p. 151909, 2007.

[98] K. Afanasyev and F. Sansoz, "Strengthening in Gold nanopillars with nanoscale twins," *Nano Letters*, vol. 7, no. 7, pp. 2056–2062, 2007.

[99] R. J. Asaro and Y. Kulkarni, "Are Rate Sensitivity and Strength Effected by Cross-Slip in Nano-Twinned FCC Metals," *Scripta Materialia*, vol. 58, no. 5, pp. 389–392, 2008.

[100] T. Zhu, J. Li, A. Samanta, H. G. Kim, and S. Suresh, "Interfacial Plasticity Governs Strain Rate Sensitivity and Ductility in Nanostructured Metals," *Proceedings of the National Academy of Sciences*, vol. 104, no. 9, pp. 3031–3036, 2007.

[101] D. Wolf, V. Yamakov, S. Phillpot, A. Mukherjee, and H. Gleiter, "Deformation of Nanocrystalline Materials by Molecular-Dynamics Simulation: Relationship to Experiments?" *Acta Materialia*, vol. 53, no. 1, pp. 1–40, 2005.

[102] K. Zhang, J. Weertman, and J. Eastman, "Rapid Stress-driven Grain Coarsening in Nanocrystalline Cu at Ambient and Cryogenic Temperatures," *Applied Physics Letters*, vol. 87, no. 6, p. 061921, 2005.

[103] F. Sansoz and V. Dupont, "Grain growth behavior at absolute zero during nanocrystalline metal indentation," *Applied Physics Letters*, vol. 89, no. 11, p. 111901, 2006.

[104] I. Ovidko, A. Sheinerman, and E. Aifantis, "Stress-driven migration of grain boundaries and fracture processes in nanocrystalline ceramics and metals," *Acta Materialia*, vol. 56, no. 12, pp. 2718–2727, 2008.

[105] X. Li, W. Y, and Y. Gao, "Competing grain-boundary- and dislocation-mediated mechanisms in plastic strain recovery in nanocrystalline aluminum," *Proceedings of the National Academy of Sciences*, vol. 106, no. 38, pp. 16 108–16 113, 2009.

[106] P. Keblinski and V. Yamakov, "Effect of High-Temperature Structure and Diffusion on Grain-Boundary Diffusion Creep in fcc Metals," *Interface Science*, vol. 11, no. 1, pp. 111–120, 2003.

[107] J. Bezares, S. Jiao, Y. Liu, D. Bufford, L. Lu, X. Zhang, Y. Kulkarni, and R. J. Asaro, "Indentation of Nanotwinned FCC Metals: Implications for Nanotwin Stability," *Acta Materialia*, vol. 60, no. 11, pp. 4623–4635, 2012.

[108] C. Shute, B. Myers, S. Xie, S. Li, T. Barbee Jr., A. Hodge, and J. Weertman, "Detwinning, Damage and Crack Initiation during Cyclic Loading of Cu Samples Containing Aligned Nanotwins," *Acta Materialia*, vol. 59, no. 11, pp. 4569–4577, 2011.

[109] X. Zhang and A. Misra, "Superior Thermal Stability of Coherent Twin Boundaries in Nanotwinned Metals," *Scripta Materialia*, vol. 66, no. 11, pp. 860–865, 2012.

[110] S. Plimpton, "Fast parallel algorithms for short-range molecular dynamics," *Journal of Computational Physics*, vol. 117, no. 1, pp. 1–19, 1995.

[111] Y. Mishin, M. Mehl, D. Papaconstantopoulos, A. Voter, and J. Kress, "Structural Stability and Lattice Defects in Copper: Ab Initio, Tight-Binding, and

Embedded-Atom Calculations," *Physical Review B*, vol. 63, no. 22, p. 224106, 2001.

[112] D. Chen and Y. Kulkarni, "Elucidating the kinetics of twin boundaries from thermal fluctuations," *MRS Communication*, vol. 3, no. 4, pp. 241–244, 2013.

[113] Z. Trautt and M. Upmanyu, "Direct two-dimensional calculations of grain boundary stiffness," *Scripta Materialia*, vol. 52, no. 11, pp. 1175–1179, 2001.

[114] C. Rottman, "Thermal fluctuation in low-angle grain boundary," *Acta Metallurgica*, vol. 34, no. 12, pp. 2465–2470, 1986.

[115] J. Cahn, Y. Mishin, and A. Z. Suzuki, "Coupling grain boundary motion to shear deformation," *Acta Materialia*, vol. 54, no. 19, pp. 4953–4975, 2006.

[116] T. Sinha and Y. Kulkarni, "Anomalous Deformation Twinning in FCC Metals at High Temperatures," *Journal of Applied Physics*, vol. 109, no. 11, p. 114315, 2011.

[117] M. Demkowicz, O. Anderoglu, X. Zhang, and A. Misra, "The Influence of Σ3 Twin Boundaries on the Formation of Radiation-Induced Defect Clusters in Nanotwinned Cu," *Journal of Materials Research*, vol. 26, no. 14, pp. 1666–1675, 2011.

[118] K. Yu, D. Bufford, C. Sun, Y. Liu, H. Wang, M. Kirk, M. Li, and X. Zhang, "Removal of stacking-fault tetrahedra by twin boundaries in nanotwinned metals," *Nature Communications*, vol. 4, no. 1377, 2013.

[119] J. Hoyt, Z. Trautt, and M. Upmanyu, "Steric interaction of fluid membranes in multiplayer systems," *Naturforschung A*, vol. 33, no. 3, pp. 305–315, 1978.

[120] W. Janke and H. Kleinert, "Fluctuation pressure of a stack of membrane," *Physical Review Letters*, vol. 58, no. 2, p. 144, 1987.

[121] M. Bachmann, H. Kleinert, and A. Peister, "Fluctuation pressure of membrane between walls," *Physical Review E*, vol. 63, no. 5, p. 051709, 2001.

[122] L. Freund, "Fluctuation pressure on a bio-membrane confined within a parabolic potential well," *Acta Mechanica Sinica*, vol. 28, no. 4, pp. 1180–1185, 2012.

[123] L. Freund, "Entropic pressure on between biomembranes in a periodic stack due to thermal fluctuations," *Proceedings of the National Academy of Sciences*, vol. 110, no. 6, pp. 2047–2051, 2013.

[124] Y. Hanlumyuang, L. Liu, and P. Sharma, "Revisiting the entropic force between fluctuating biological membranes," *Journal of the Mechanics and Physics of Solids*, vol. 63, no. 2, pp. 179–186, 2014.

[125] J. Radler, T. Feder, H. Strey, and E. Sackmann, "Fluctuation analysis of tension-controlled undulation forces between giant vesicles and solid substrates," *Physical Review E*, vol. 51, no. 5, p. 4526, 1995.

[126] J. Radler, T. Feder, H. Strey, and E. Sackmann, "Cytoskeleton confinement and tension of red blood cell membranes," *Physical Review Letters*, vol. 90, no. 22, p. 228101, 2003.

[127] R. Merath and U. Siefert, "Fluctuation spectra of free and supported membrane pairs," *The European Physical Journal E*, vol. 23, no. 1, pp. 103–116, 2007.

[128] O. Farago, "Membrane fluctuations near a plane rigid surface," *Physical Review E*, vol. 78, no. 5, p. 051919, 2008.

[129] K. Zakharchenko, J. Los, M. Katsnelson, and A. Fasolino, "Atomistic simulation of structural and thermodynamic properties of bilayer graphene," *Physical Review B*, vol. 81, no. 23, p. 235439, 2010.

[130] J. Rickman and R. Lesar, "Finite-temperature dislocation interactions," *Physical Review B*, vol. 64, no. 9, p. 094106, 2001.

[131] F. Hammami and Y. Kulkarni, "Size Effects in Twinned Nanopillars," *Journal of Applied Physics*, vol. 116, no. 3, p. 033512, 2014.

[132] D. Chen and Y. Kulkarni, "Atomistic study of the thermal stress due to twin boundaries," *Journal of Applied Mechanics*, vol. 82, no. 2, p. 021005, 2015.

[133] S. Phillpot, "Thermoelastic behavior of grain boundary superlattices," *Journal of Applied Physics*, vol. 72, no. 12, pp. 5606–5615, 1992.

[134] H. Klam, H. Hahn, and H. Gleiter, "The thermal expansion of grain boundaries," *Acta Metallurgica*, vol. 35, no. 8, pp. 2101–2104, 1987.

[135] M. Wagner, "Structure and thermodynamics properties of nanocrystalline metals," *Physical Review B*, vol. 45, no. 2, pp. 635–639, 1991.

[136] J. Jasczak and D. Wolf, "Thermoelastic behavior of structurally disordered interface materials: homogeneous versus inhomogeneous effects," *Physical Review B*, vol. 46, no. 4, pp. 2473–2480, 1992.

[137] K. Lu and M. Sui, "Thermal expansion behaviors in nanocrystalline materials with a wide grain size range," *Acta Metallurgica et Materialia*, vol. 43, no. 9, pp. 3325–3332, 1995.

[138] G. Palumbo, E. Lehockey, and P. Lin, "Applications for grain boundary engineered materials," *JOM*, vol. 50, no. 2, pp. 40–43, 1998.

[139] A. Schwartz and W. King, "The potential engineering of grain boundaries through thermomechanical processing," *JOM*, vol. 50, no. 2, pp. 55–56, 1998.

[140] M. Kumar, A. Schwartz, and W. King, "Microstructural evolution during grain boundary engineering of low to medium stacking fault energy fcc materials," *Acta Materialia*, vol. 50, no. 10, pp. 2599–2612, 2002.

[141] A. Schuh, M. Kumar, and W. King, "Analysis of grain boundary networks and their evolution during grain boundary engineering," *Acta Materialia*, vol. 51, no. 3, pp. 687–700, 2003.

[142] V. Randle, "Twinning-related grain boundary engineering," *Acta Materialia*, vol. 52, no. 14, pp. 4067–4081, 2004.

[143] D. Molodov, U. Czubayko, G. Gottstein, and L. Shvindlerman, "On the effect of purity and orientation on grain boundary motion," *Acta Metallurgica*, vol. 46, no. 2, pp. 553–564, 1998.

[144] Y. Huang and F. Humphreys, "Measurements of grain boundary mobility during recrystallization of a single-phase aluminium alloy," *Acta Metallurgica*, vol. 47, no. 7, pp. 2259–2268, 1999.

[145] Y. Huang and F. Humphreys, "Subgrain growth and low angle boundary mobility in aluminium crystals of orientation," *Acta Materialia*, vol. 48, no. 8, pp. 2017–2030, 2000.

[146] G. Gottstein, D. Molodov, L. Shvindlerman, D. Srolovitz, and M. Winning, "Grain boundary migration: misorientation dependence," *Current opinion in solid state and materials science*, vol. 5, no. 1, pp. 9–14, 2001.

[147] M. Winning, G. Gottstein, and L. Shvindlerman, "On the mechanisms of grain boundary migration," *Acta Materialia*, vol. 50, no. 2, pp. 353–363, 2002.

[148] M. Winning, G. Gottstein, and L. Shvindlerman, "Grain boundary shear migration coupling—1. Insitu TEM straining experiments in Al polycrystals," *Acta Materialia*, vol. 57, no. 7, pp. 2198–2209, 2009.

[149] M. Mendelev, C. Deng, C. Schuh, and D. Srolovitz, "Comparison of molecular dynamics simulation methods for the study of grain boundary migration," *Modelling and Simulation in Materials Science and Engineering*, vol. 21, no. 4, pp. 0 145 017–045 029, 2013.

[150] G. Gottstein and L. Shvindlerman, *Grain boundary migration in metals: thermodynamics, kinetics, applications*. CRC Press, 1999.

[151] M. Mendelev and D. Srolovitz, "Impurity effects on grain boundary migration," *Modelling and Simulation in Materials Science and Engineering*, vol. 10, no. 6, pp. 79–109, 2002.

[152] J. Cahn, "The impurity-drag effect in grain boundary motion," *Acta Metallurgica*, vol. 10, no. 9, pp. 789–798, 1962.

[153] K. Lucke and H. Shvindlerman, "Recovery and recrystallization of metals," *New York: Interscience*, 1963.

[154] J. Cahn and A. Cohen, "Motion by curvature and impurity drag: resolution of a mobility paradox," *Acta Materialia*, vol. 48, no. 13, pp. 3425–3440, 2000.

[155] M. Mendelev and D. Srolovitz, "A regular solution model for impurity drag on a migration grain boundary," *Acta Materialia*, vol. 49, no. 4, pp. 589–597, 2001.

[156] A. Suzuki and Y. Mishin, "Interaction of point defects with grain boundaries in fcc metals," *Interface Science*, vol. 11, no. 4, pp. 425–437, 2003.

[157] M. Mendelev and D. Srolovitz, "Effect of Fe segregation on the migration of a non-symmetric Σ5 tilt grain boundary in Al," *Journal of Materials Research*, vol. 20, no. 1, pp. 208–218, 2005.

[158] D. Srolovitz, F. Fischer, and M. Leindl, "Transient solute drag in migrating grain boundaries," *Acta Materialia*, vol. 59, no. 17, pp. 6656–6562, 2011.

[159] H. Sun and C. Deng, "Adapted solute drag model for impurity controlled grain boundary motion," *Journal of Materials Research*, vol. 29, no. 12, pp. 1369–1375, 2014.

[160] H. Sun and C. Deng, "Direct quantification of solute effects on grain boundary motion by atomistic simulations," *Computational Materials Science*, vol. 93, no. 10, pp. 137–143, 2014.

[161] C. Smith, "Grains, phases, and interphases: an interpretation of microstructure," *Trans. Metall. Soc*, vol. 175, pp. 15–51, 2014.

[162] P. Manohar, M. Ferry, and T. Chandra, "Five decades of the zener equation," *ISIJ International*, vol. 38, no. 9, pp. 913–924, 1998.

[163] G. Ackland, G. Tichy, V. Vitek, and M. Finnis, "Simple N-body potentials for the noble-metals and nickel," *Philosophical Magazine A*, vol. 56, no. 6, pp. 735–756, 1987.